NASA CR-159675
R79-912997-39

DEVELOPMENT OF SiAlON MATERIALS

G.K. Layden

UNITED TECHNOLOGIES RESEARCH CENTER

prepared for

NATIONAL AERONAUTICS AND SPACE ADMINISTRATION

NASA LEWIS RESEARCH CENTER

Contract NAS 3-19712

FINAL REPORT

September 1979

1. Report No.	2. Government Accession No.	3. Recipient's Catalog No.
NASA CR-159675		

4. Title and Subtitle	5. Report Date
Development of SiAlON Materials	September 1979
	6. Performing Organization Code

7. Author(s)	8. Performing Organization Report No.
G. K. Layden	R79-912997-39
	10. Work Unit No.

9. Performing Organization Name and Address	11. Contract or Grant No.
United Technologies Reserach Center East Hartford, Connecticut 06108	NAS3-19712

12. Sponsoring Agency Name and Address	13. Type of Report and Period Covered
National Aeronautics and Space Administration Lewis Research Center Cleveland, Ohio 99135	Contractor Report June 1975, September 1979
	14. Sponsoring Agency Code

15. Supplementary Notes

Final Report
Project Manager, T. P. Herbell, Materials and Structures Division
NASA Lewis Research Center, Cleveland, Ohio

16. Abstract

Cold pressing and sintering techniques were used to produce ceramic test specimens in which the major phase was either Si_3N_4 or a solid solution having the β Si_3N_4 structure. Additional components were incorporated to promote liquid phase sintering. Glass and/or crystalline phase were consequently retained in boundaries between Si_3N_4 grains which largely determined the physical properties of the bodies. Systems investigated most extensively included R-Si-Al-O-N (R = rare earth element) Zr-Si-Al-O-N, Y-Si-Be-O-N, and R_1-R_2-Si-O-N.

Room temperature and 1370°C modulus of ruptured, 1370°C creep, and oxidation behavior are discussed in terms of phase relationships in a parent quinery, and relavent ternary oxide systems.

17. Key Words (Suggested by Author(s))	18. Distribution Statement
SiAlON, Silicon Nitride, Nitrogen Ceramics, Gas Turbine Materials, Sintering, Ceramic Processing	Unclassified - Unlimited N79-33258 #

19. Security Classif. (of this report)	20. Security Classif. (of this page)	21. No. of Pages	22. Price*
Unclassified	Unclassified	137	

* For sale by the National Technical Information Service, Springfield, Virginia 22161

TABLE OF CONTENTS

LIST OF TABLES

LIST OF TABLES (Cont'd)

LIST OF FIGURES

LIST OF FITURES (Cont'd)

LIST OF FIGURES (Cont'd)

R79-912997-39

Development of SiAlON Materials

SECTION I

SUMMARY

The objective of this program was the development of Si_3N_4 based ceramic bodies which can be fabricated to complex shapes by conventional forming and pressureless sintering techniques, and which exhibit properties which make them suitable for high stress applications in gas turbines at temperatures up to 1370°C (2500°F). Target goals were: flexural strength at 25°C of 520 MPa (75 ksi) and at 1370°C of 415 MPa (60 ksi); creep rate at 1370°C and 69 MPa (10 ksi) on the order of 10^{-5} hr^{-1}; static air oxidation parabolic rate constant at 1400°C on the order of 0.01 $mg^2cm^{-4}hr^{-1}$.

Work completed during the first 21 months of this program was presented in detail in the interim report NASA CR-135290. The earlier work identified the systems Zr-Si-Al-O-N and Y-Si-Al-O-N, as being promising candidates in terms of oxidation resistance, and mechanical properties, respectively. However, no compositions were produced from either system which presented the desired balance of properties. In the current work, these two systems - particularly the latter - were examined in greater depth. Solid phase equilibria were explored, and compatibility tetrahedra delineated. Property data for bodies from various tetrahedra were determined. In the case of the Zr-Si-Al-O-N system, it was concluded that sinterable β' based ceramic formulations exist only on the "oxide" side of the β' homogeniety line. The greatest extent of sinterable formulations lie in the β'_{10-60}-X-ZrN tetrahedron. Solidus temperatures appeared to be low in this tetrahedron, and samples had little strength or creep resistance at 1370°C. A composition on the β'_{0-10}-ZrO_2 plane (94.6 m/o $Si_{2.7}Al_{.3}N_{3.7}$ m/o 5.4 ZrO) also exhibited unacceptably high creep at 1370°C. If sinterable formulations with acceptably low creep exist in the Zr-Si-Al-O-N system, they must lie very close to pure Si_3N_4.

The Y-Si-Al-O-N system is more complex than the analogous Zr system. Five 3-phase, and eleven 4-phase compatibility tetrahedra exist wherein one phase is either Si_3N_4 or $Si_{3-x}Al_xO_xN_{4-x}$ solid solution. Property data for compositions from all of the 3-phase, and two of the 4-phase compatibility tetrahedra were screened for oxidation and mechanical properties. Oxidation properties at a given temperature are discussed by projecting body compositions (in cation equivalent percent) onto the relevant isothermal sections of the Y_2O_3-Al_2O_3 - SiO_2 phase diagram. The only sinterable bodies with low oxidation rates at 1400°C (on the order of 0.01 $mg^2cm^{-4}hr^{-1}$) were compositions whose oxides fell in the primary

phase field of mullite, and which produced scales that were at least 30 volume percent mullite at 1400°C. These compositions fall in regions of the quinery system where the solidus temperature is low (perhaps below 1500°C) so that 1370°C mechanical properties are poor. No sinterable composition was found that exhibited oxidation and mechanical properties that would be acceptable for high stress applications in oxidizing atmospheres at 1370°C. However, bodies were produced which exhibit properties attractive for stressed application at temperatures of 1300°C and below. One formulation (96.6 m/o $Si_{2.614}Al_{.386}O_{.386}N_{3.614}$ + 2.3 m/o $Y_3Al_5O_{12}$ + 1.0 m/o $Si_3Al_6N_{10}$) produced samples which exhibited the following properties:

Property	Value
1300°C oxidation rate	0.003 $mg^2cm^{-4}hr^{-1}$
25°C MOR (mean)	518 MPa
1370°C MOR (mean)	340 MPa
1370°C, 69 MPa creep	6×10^{-5} hr^{-1}

New systems explored during the final phases of the program were the Y-Si-Be-O-N system, and various R-Si-O-N and R_1-R_2-Si-O-N sytems where R represents a rare earth element. Only a limited number of compositions were studied in the Y-Si-Be-O-N system, but these were sufficient to delineate some of the compatibility tetrahedra in the quinery system. In general, oxidation rates for samples from this system were an order of magnitude lower than those for analogous compositions from the Y-Si-Al-O-N system. However, none of the compositions investigated exhibited acceptable creep properties.

Of the R-Si-O-N systems that were studied, dense bodies could not be produced from the yttrium system, probably because the viscous liquid which formed at sintering temperatures (1750°C) could not wet out the bodies. Theoretically, dense bodies could be sintered from the cerium, neodymium, and gadolinium-samarium analog systems, but samples from these systems exhibited excessive rates of oxidation.

Bodies were produced from the Si_3N_4-SiO_2-$Y_{2-x}Ce_xO_3$ system which exhibited acceptable oxidation (0.015 $mg^2cm^{-4}hr^{-1}$) and 1370°C strength properties (400 MPa). XRD (x-ray diffraction) studies of the bodies disclosed them to be non-equilibrium assemblies with a minor phase constitution of $Y_2Si_2O_7$ and glass. The 1370°C creep tests of the material in argon atmosphere initiated the recrystallization of the minor phase assemblage to H phase and $Y_2Si_2O_7$ with a progressive decrease in 1370°C, 69 MPa creep rate to a value of 5×10^{-5} hr^{-1} at the time of rupture, 36 hrs into the test. The

grain boundary transformation, occurring under stress, is presumed to be responsible for the low stress rupture life of the sample.

It appears that the systems of the type Si_3N_4-SiO_2-$Y_{2-x}R_xO_3$ have a good potential for producing sinterable bodies for 1370°C application, but development of heat treating cycles to yield equilibrated bodies with low internal stresses is required.

SECTION II

INTRODUCTION

The gas turbine is considered as a candidate for an alternative engine for automotive and marine use as well as for power generation. Efficient use of fuel can be achieved by high turbine operating temperatures and light rotating parts. These considerations, plus the necessity of using nonstrategic and potentially inexpensive materials, have led to serious consideration of the use of ceramic components. Stringent property requirements have limited the ceramic candidates for rotating parts to Si_3N_4 and SiC based materials. While hot pressed Si_3N_4 would appear to offer the most attractive properties at the present time, the great expense of machining parts from this material is prohibitive, and alternative materials are sough which can be formed to near net shape by conventional sintering process.

The object of this program is the development of a formulation or formulations for ceramic bodies which can be fabricated to complex shapes by conventional sintering techniques and which exhibit properties which make them suitable for highly stressed applications in a gas turbine. Target property goals for the program are: flexural strength at 25°C of 520 MPa (75 ksi), and at 1370°C of 415 MPa (60 ksi); creep rate at 1370°C and 69 MPa (10 ksi) on the order of 10^{-5} hr^{-1}, static air oxidation parabolic rate constant at 1400°C on the order of 0.01 $mg^2cm^{-4}hr^{-1}$.

Materials which were investigated contained over about 90 volume percent Si_3N_4 or solid solution having the βSi_3N_4 structure. Such solid solutions are formed by substitution of Al and/or Be for Si, and O for N in the Si_3N_4 structure (Refs. 1 through 10). Neither pure Si_3N_4 bodies nor β solid solutions can be sintered to theoretical density (Refs. 3 and 6). Si_3N_4 based bodies can be sintered by choosing compositions which contain some liquid at the firing temperature. This can be accomplished by using compositions in the β'-X phase field in the SiAlON systems (Refs. 11 and 12), or using "sintering aids" - usually additional oxide components which promote liquid formation (Refs. 13 through 20). In either case, the fired bodies contain phases other than βSi_3N_4 or β' solid solution which to a great extent determine the properties of the bodies, particularly at elevated temperature. The task of identifying acceptable formulations then becomes one of extensive property testing.

Progress toward this goal during the first twenty one months of this program was described in an interim report (Ref. 21), the results of which are briefly summarized below.

Bodies investigated during the first twenty-one months of the program were limited to $Si_{3-x}Al_xO_xN_{4-x}$ formulations to which were added different weight percentages of various "sintering aids", including $AlPO_4$, $GaPO_4$, ZrO_2, ZrC, Cr_2O_3, TiO_2, HfO_2, Y_2O_3, La_2O_3, Er_2O_3, Nd_2O_3 and $GdSmO_3$. Uniformly dense bodies were obtained only with ZrO_2, Y_2O_3 (and mixtures of these), and other rare earth oxide additions. The best mechanical properties obtained up to this point were achieved with β' compositions with low values of x (about 0.5 and below) with additions of Y_2O_3. Bodies of composition $Si_{2.7}Al_{.3}O_{.3}N_{3.7}$ + 2.5 w/o Y_2O_3 exhibited room temperature flexural strengths up to about 550 MPa (80,000 psi). In the absence of other more deleterious types of flaws, room temperature strength of these bodies was controlled by the presence of metallic inclusions. Strength at 1370°C was grain boundary limited and reached about 450 MPa (65 ksi). The creep rate for a β' $Si_{2.45}Al_{.55}O_{.55}N_{3.45}$ - 5 w/o Y_2O_3 sample at 1370°C and 69 MPa stress was $6x10^{-5}hr^{-1}$. β'-Y_2O_3 samples, however, proved to have high oxidation rates at 1400°C (0.3 $mg^2cm^{-4}hr^{-1}$), although oxidation was quite slow at 1300°C (0.003 $mg^2cm^{-4}hr^{-1}$).

Bodies formulated as β' + ZrO_2 (and β' + ZrO_2-Y_2O_3 mixtures) were found to exhibit exceptionally low oxidation rates (virtually zero weight gain of 1400°C) and good room temperature strength. However, the creep rate at 1370°C and 69 MPa stress was on the order of $4x10^{-3}hr^{-1}$, making these formulations unusable under high stress at that temperature.

A correlation was shown between the oxidation rate of the ceramic bodies and the minimum liquidus temperatures in the systems containing the oxidation products For compositions where the minimum ternary eutectic temperature in the system containing the oxidation products was above the test temperature (i.e., in the SiO_2-Al_2O_3, and SiO_2-ZrO_2-Al_2O_3 systems) thin protective oxide scales developed, and the static oxidation rates were low. Bodies whose oxidation products fell in systems with minimum liquidus below test temperature (i.e., SiO_2-Al_2O_3-R_2O_3 where R = rare earth), exhibited relatively rapid rates of oxidation.

During the earlier phases of this program, described in Ref. 21, it was realized that the formulations investigated (β' + foreign oxide) represented a limited sampling of the possible phase assemblages that could exist in the various systems considered. However, lack of phase equilibrium data for the relevant quinery systems (e.g., Y-Si-Al-O-N, Zr-Si-Al-O-N) was deemed an impediment to a reasonably structured approach to selecting formulations which would yield the desired properties. During the current phase of this program we have carried out compatibility studies in the two above named systems to serve as the framework for understanding and projecting property data. Test samples having compositions lying in various compatibility tetrahedra in the Y-Si-Al-O-N system were evaluated. Also, solid-liquid equilibrium in portions of the Si_3N_4-Y_2O_3-SiO_2 system were studied in an attempt to formulate sinterable bodies from this system. Although liquid was present at temperatures at least as low as 1700°C in parts of the system,

this was not effective in producing dense bodies by pressureless sintering. Attempts to find effective agents to promote densification relative to that in the Si_3N_4-Y_2O_3-SiO_2 system, without degrading oxidation and/or creep properties too severely, led to the investigation of bodies in the systems Y-Si-Be-O-N, Ce-Si-Be-O-N and R-Y-Si-O-N.

In the report which follows, the chronology of the work reported is ignored in favor of organizing results in terms of systems. Much of the tabular fabrication and test data will be relegated to appendices wherein the chronological sample numbering systems is retained. Recent data on test bodies formulated in the Y-Si-Al-O-N have led to minor revisions of our interpretation of compatible relations in this system, originally reported in ninth quarterly report (Ref. 22). These include: 1) an expansion of the portion of the system investigated to include the higher AlN polytypes reported by Gauckler, et al. (Ref. 1), Jack (Ref. 7), and Land, et al. (Ref. 4), 2) assigning the appropriate homogeneity ranges to the phases X, 15R and O' ($Si_2N_2O_{ss}$) rather than treating these as point compounds as was done for simplicity in Ref. 22, and 3) adding one tie line and deleting another. These changes necessitated revision of the assumed phase compositions listed in several tables in earlier reports. This accounts for discrepancies that occur in a few instances between data as it appears here, and as it was originally presented in the quarterly reports. Also, some data from four β'-Y_2O_3 samples originally presented in the interim report (Ref. 21) are recast in terms of the compatibility relationships as they are now understood. Similar revisions have been made in drawing the Zr-Si-Al-O-N diagram and in recasting old β'-ZrO_2 data in light of these relationships.

SECTION III

EXPERIMENTAL PROCEDURES

A. Sample Preparation

1. Raw Materials

Several different Si_3N_4 powders were used during the course of the program. These were: AME high purity 90 percent α phase -300 mesh powder, KBI high purity 85 percent α phase -325 mesh powder, Starck high alpha - 1μ powder, and GTE SN-402 amorphous Si_3N_4. Al_2O_3 was Linde A micropolish, and AlN was Atlantic Equipment Engineers (AEE) AL106 99.9 percent -325 mesh. Spectrochemical analyses of impurities in these starting powders, and fast neutron activation analyses for oxygen in the Si_3N_4 powders are presented in Table 1. SiO_2 powders used were -270 mesh silica glass, Apache 0.03 μ 99.99 + purity, or AEE SI239 99.9 -325 mesh. Other compounds used in formulations are listed in Table 2. Chemical analyses were not performed on these compounds. Unless otherwise stated in subsequent text or tables, samples were prepared using the KBI Si_3N_4 and AEE SiO_2.

2. Powder Preparation Techniques

a) Powders for Compatibility Studies

Phase compatibility studies in the Y-Si-Al-O-N and Zr-Si-Al-O-N systems used the AME Si_3N_4 powder, Linde A, and -270 mesh silica glass. Initial studies in the $BeO-Y_2O_3-SiO_2$ system used Be_2SiO_4 as a constituent. This was prepared by calcining a mixture of AEE -325 mesh SiO_2 and beryllium carbonate. Later formulations used BeO obtained from the carbonate as a constituent. Mixtures were lightly ground under acetone in an alumina mortar to a smooth past-like consistency, then allowed to dry fully.

b) Powders for Test Bar Fabrication

In general, powders for test bar fabrication were prepared in 30 to 100 gram batches. Constituents were weighed out into wide mouth 16 oz. polyethylene jars containing a known weight of either high alumina, or reaction sintered Si_3N_4 grinding media, and methanol was then added to cover the charges. In some instances, a measured volume of carbowax-methanol solution was added to the ball mill charges. The jars were rolled at 75 rpm for a predetermined time (typically 18 hrs), then the charges were transferred to wash bottles and dried by spraying onto a heated aluminum plate. The wash bottles were kept agitated during the spraying process, and dried material was frequently scraped from the plate into a

TABLE 1

ANALYSES OF RAW MATERIALS

Reagent		Al	Si	Ca	Co	Cr	Fe	Mg	Mo	Ni	Zn	O*
Si_3N_4	AME	.15	major	< .02	< .05	< .01	.10	< .01	< .01	.02	.02	1.9
	KBI	.05	major	< .02	< .05	< .01	.30	< .01	< .01	< .01	< .02	0.8
	GTE SN402	<.01	major	< .02	< .05	< .01	.01	< .01	< .01	< .01	< .02	2.2
	Starck	.18	major	.01	< .05	< .01	.01	< .01	< .01	< .01	< .02	1.1
AlN		> 10	.20	<.02	.10	< .01	.07	.40	.02	.05	.02	
Al_2O_3		> 10	< .01	<.01	< .01	< .01	< .01	< .01	< .01	< .01	< .01	

* Determined by fast neutron activation analyses

TABLE 2

OXIDE ADDITIVES

$AlPO_4$	Rocky Mountain Research 99.99% Purity
ZrO_2	Gallard Schlesinger 99.9% Purity
BeO	Alfa Inorganics Beryllium Carbonate (Calcined)
Y_2O_3, $GdSmO_3$	Molycorp oxalates (calcined)
Er_2O_3, La_2O_3, Nd_2O_3	Apache Chemicals Inc. 99.9% Purity
Sm_2O_3	American Potash Oxalate (calcined)

surrounding tray. The spray dried material was then passed through either a 20 or 100 mesh screen. The grinding media were washed, thoroughly dried, and weighed after the drying operation, and logs were kept of the media weight. Predictions of the media pick up by the batches were generally factored into the formulations. Exceptions to this practice will be noted where appropriate.

3. Cold Pressing of Green Samples

In general, samples for compatibility studies were pressed into 1.5 cm diameter pellets in a hardened steel piston die to a final pressure of 120 MPa. Test bars were pressed to dimensions approximately 0.4 cm x 1 cm x 15 cm in a steel die. These were then cut into three or four shorter bars. These were placed in individual latex bags which were then evacuated and tied off, and isostatically pressed to 275 MPa.

4. Calcining

Samples pressed from batches containing carbowax binder were heated in air from room temperatures to 600°C on a three day linear heating schedule in order to burn out the binder prior to firing in nitrogen.

5. Firing

Sample pellets for compatibility studies in the Y-Si-Al-O-N and Zr-Si-Al-O-N systems were loaded into covered boron nitride crucibles and placed in the graphite susceptor of the vacuum induction unit described in Ref. 21. The furnace chamber was evacuated to about 100 micron pressure, backfilled with nitrogen, reevacuated, and finally filled with nitrogen to one atmosphere of pressure. During the final filling, the heating was started and the furnace brought to the intended temperature in approximately 15 minutes. The temperature was monitored with a commercial W-Re sealed thermocouple. Thermocouples aged with use, and were occasionally calibrated against the melting point of wollastonite ($CaSiO_3$, m.p. 1544°C). Unless otherwise stated, samples were maintained at the nominal firing temperature for 1 hour before cooling to room temperature.

Samples for compatibility studies in the $BeO-Y_2O_3-SiO_2$ system were fired on platinum foil in air in a resistance heated furnace using a variety of heating schedules. Heat treatments will be described later.

In general, test bars were fired in an Astro model 1000-3060-FP-12 furnace equipped with L&N Electromax III controller, and Data Track model 5300 card programmer. The temperature profile was flat over the region of the furnace which contained the samples, and temperature was reproducible to within 5°C at about 1700°C. Samples were placed in covered boron nitride crucibles, inside graphite crucible holders which held the covers in place during evacuation. The furnace

chamber was evacuated and back filled to atmospheric pressure of nitrogen a total of three times, then a slow flow of nitrogen maintained in the furnace during firing. Firing schedules varied and will be presented later.

6. Grinding and Polishing Test Bars

In general, fired bars were waxed to a metal plate and surface ground to a uniform thickness. Samples for mechanical test were finished on the tensile surface through various grits of SiC papers, and some were subsequently polished with Linde A micropolish. The edges of the tensile face were beveled at an angle of 45° for about 0.025 cm. The surface finish will be specified in subsequent tables as 240 grit, Line A, etc. Samples for oxidation testing were finished on all surfaces to the specified finish. Exceptions were samples containing beryllium, which were tested for oxidation in the as-fired condition, and were finished by hand to the specified finish for mechanical testing in order to avoid machine grinding.

B. Sample Evaluation

1. Characterization of Fired Samples

Bulk density, specific gravity, and apparent porosity of sintered specimens were determined using procedures of ASTM test C373-5. Microstructures were examined on polished and etched sections of selected test specimens. Phase identification was made on the basis of XRD (X-ray defraction) and metallographic evidence.

a. Mechanical Testing

Room temperature testing was performed in four point flexure using inner and outer spans of 0.95 cm and 1.90 cm, respectively. Cross head speed was 0.05 cm/min. Tests at 1370°C were performed in three point flexure using a span of 1.9 cm and a cross head speed of .05 cm/min. Test atmosphere was argon, and the sample supports and loading nose were tungsten. Fracture surfaces of selected test specimens were examined in the scanning electron microscope (SEM). Creep testing was done in three point flexure at 1370°C at a stress level of 69 MPa (10 ksi).

In some instances, test samples were heated in air at 1370°C for extended periods of time prior to testing.

b. Oxidation Testing

In general, samples were placed on platinum foil so fashioned that the samples were contacted along two lines only. Samples were introduced into a preheated oven

and removed periodically, cooled to room temperature, and the weight recorded. (In some instances, samples were placed across .05 cm dia platinum wire rails that were welded to an irridium-rhodium alloy sheet. This practice was discontinued when it was discovered that rhodium was being transferred to the samples.)

Following the oxidation tests, x-ray diffraction patterns were obtained from oxidized surfaces, and the samples were photographed. In most instances, the samples were then mounted in resin, polished to give a cross sectional view of the oxide scale, and examined metallographically. In selected instances, polished sections were examined by EDAX^{R} (energy dispersive analysis of X-rays) to ascertain the distribution of elements in the oxide scale.

SECTION IV

RESULTS AND DISCUSSION

A. The System Zr-Si-Al-O-N

1. Background

The five component system was investigated by treating it as a six component reciprocal system, based on the end members Si_3N_4-AlN-"Zr_3N_4" and SiO_2-Al_2O_3-ZrO_2, making up an equilateral prism as shown in Fig. 1. The zirconium nitride "Zr_3N_4" was chosen as an end member to make possible the plotting of this member on quadrilateral planes in any tetrahedron with Zr at an apex. The compound Zr_3N_4 has been prepared by Juza, et al. (Ref. 23) and was stated to decompose above 700°C into 3ZrN+N.

Prior work on some of the binary subsystems includes that of Aramaki and Roy (Ref. 24) and Welch (Ref. 25) on the system Al_2O_3-SiO_2, Geller and Lang (Ref. 26) and Butterman and Foster (Ref. 27) on the system ZrO_2-SiO_2, Lejus (Ref. 28) on the system AlN-Al_2O_3, Gilles (Ref. 29) and Claussen et al. (Ref. 30) on the system ZrN-ZrO_2. The ternary subsystem Al_2O_3-SiO_2-ZrO_2 has been investigated by Kordyuk and Gul'ko (Ref. 31) and Herold and Smothers (Ref. 32) and, more recently, by Sorrell and Sorrell (Ref. 33). The compatibility relationships drawn in Ref. 32 defining the compatibility triangle Al_2O_3-$3Al_2O_3.2SiO_2$-$ZrO_2.SiO_2$ are at odds with those drawn in Ref. 31 which shows ZrO_2-$ZrO_2.SiO_2$-$3Al_2O_3.SiO_2$ co-existing. Reference 33 confirms the latter assemblage.

Rae et al. (Ref. 20) examined the system Si_3N_4-SiO_2-"Zr_3N_4"-ZrO_2 and established a behavior diagram at 1700°C shown in Fig. 2. They also reported one new phase in the Zr-Si-Al-O-N system. It was reported to be close to the composition $5AlN.3ZrO_2$ with a cubic unit cell approximately four times that of ZrN. They do do show $ZrSiO_4$ as a phase existing at this temperature.

The subsystem Si_3N_4-SiO_2-Al_2O_3-AlN has been investigated by Gauckler et al. (Ref. 5), Land et al. (Ref. 4), Jack (Ref. 7) and Layden (Ref. 6). Figure 3 is a reproduction of the behavior diagram for the system presented by Jack (Ref. 7). There is a basic agreement between the above referenced authors regarding the general aspects of equilibrium between the phases although the compositions assigned to specific new phases (e.g., X, 15R, etc) vary somewhat, as do the homogeniety ranges of solid solution phases.

2. Experimental Results

The phase 5 $AlN.3ZrO_2$ reported by Rae (Ref. 20) was not confirmed. The only reaction products between components Al_2O_3, AlN, "Zr_3N_4" and ZrO_2 that were

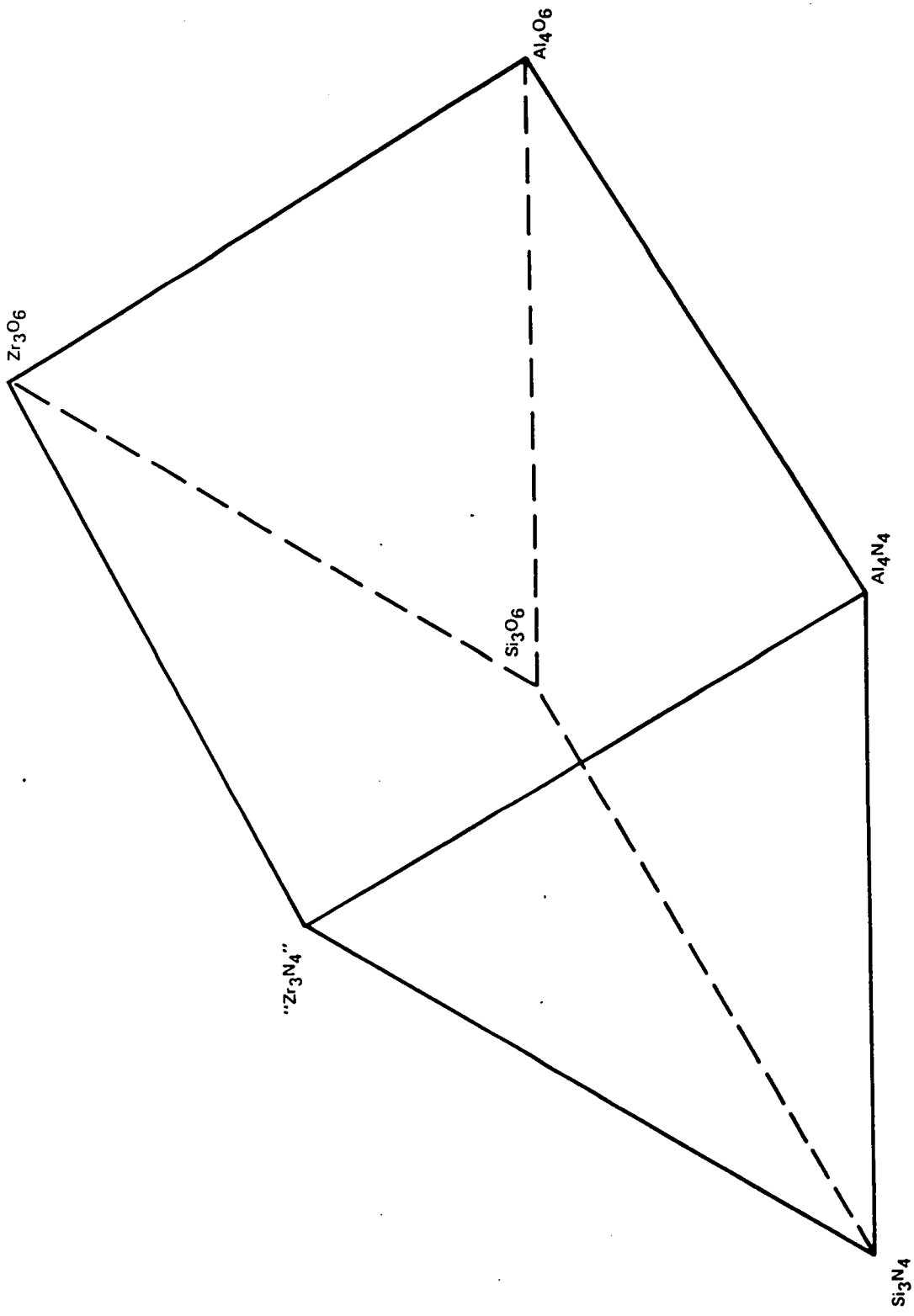

Figure 1. Representation of the Quinary System

78-01-86-3

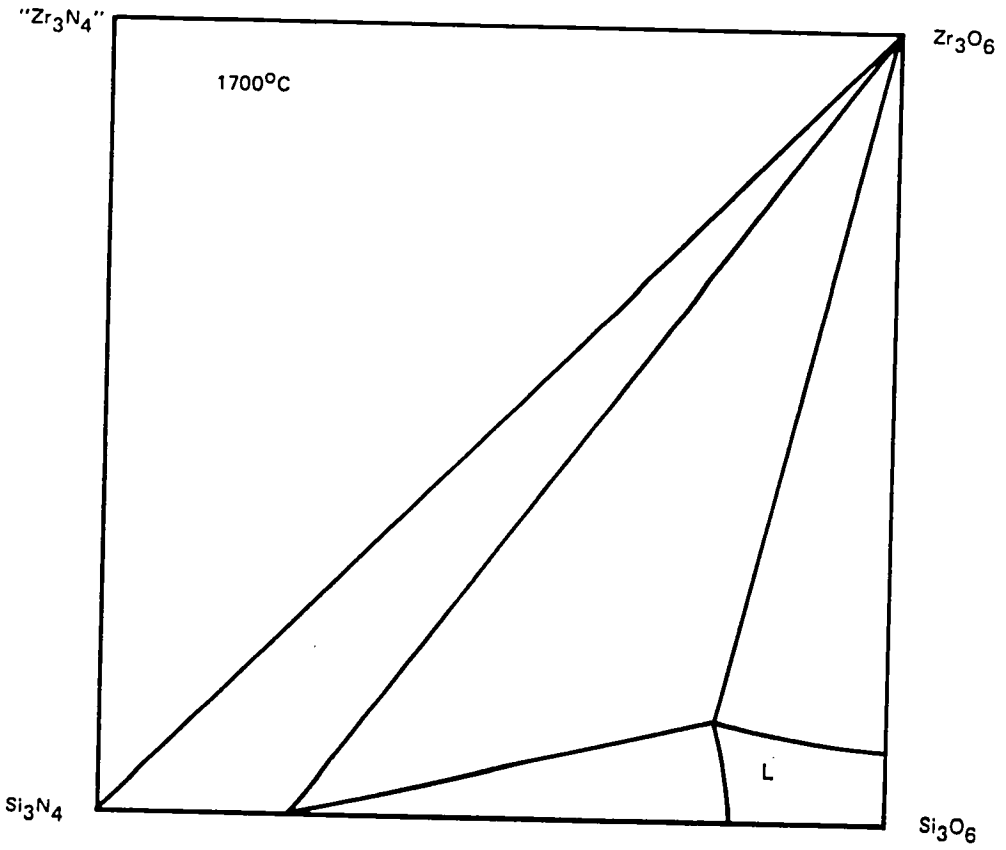

Figure 2. System Si_3N_4–Si_3O_6–Zr_3O_6–Zr_3N_4 After Rae et al

78-01-86-5

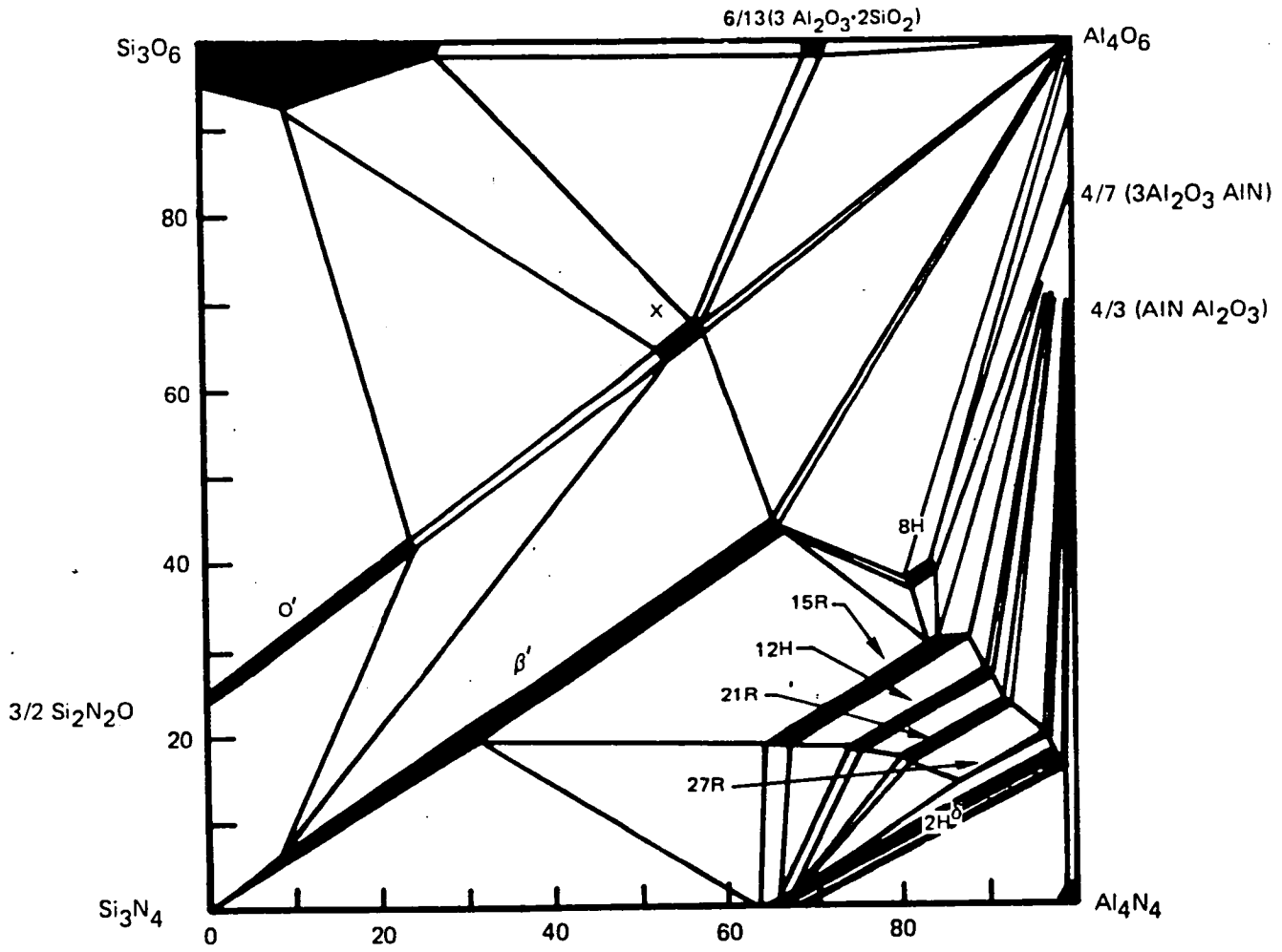

Figure 3. System Si_3N_4–AlN–Al_2O_3–SiO_2 After Jack

77–02–172–7

observed were the spinel phase solid solution centered around Al_3O_3N and a cubic phase between ZrN and ZrO_2. Compatibility was observed between "Zr_3N_4" (ZrN) and Al_2O_3) and between ZrN and the spinel phase. Since the spinel phase is known to be unstable below about 1600°C (Refs. 28, 6) it may be inferred that the observed compatibility with ZrN was metastable at lower temperatures, and that ZrN-AlN-Al_2O_3 form a compatibility triangle below about 1600°C. Compatibility was established between ZrN and the ternary phases β', 15R and X, and between X and ZrO_2. Topographical considerations then necessitated the compatibility of ZrN and the $2H^{\delta}$ end member $Si_3Al_6N_{10}$ also. On the basis of the Si_2O-Al_2O_3-ZrO_2 diagram as drawn by Sorrell and Sorrell (Ref. 33), one can infer compatibility between $ZrO_2.SiO_2$ and X phase, and between $ZrO_2.SiO_2$ and Si_2N_2O as well. These joins, however, were not investigated experimentally. The above data, along with the relations shown on Fig. 3 establish the compatibility tetrahedra shown on Fig. 4. Relationships involving the AlN polytypes are not shown except those involving the 15R (treated here as a point, rather than a line compound) and the $Si_3Al_6N_{10}$ $2H^{\delta}$ end member. A list of the 3 and 4 phase compatibility tetrahedra shown in Fig. 4 which involve β' solid solutions as one component is given in Table 3. (Several additional probable 4 phase tetrahedra involving the β_{60} end member, not shown on Fig. 4, but presumed to exist on the basis of Fig. 3 are added in parenthesis.)

It can be seen from Fig. 4 that ZrO_2 is in equilibrium with β' only over the range β_o to β_{10} (i.e., from 0 to 10 e/o Al). At higher aluminum concentrations in the β' solution, small additions of ZrO_2 move the composition into the β'-15R-ZrN tetrahedron. Of the two β'-ZrO_2 compositions (ignoring the small Y_2O_3 substitution for ZrO_2) previously tested in creep at 1370°C (Ref. 21 pp. 90-93), sample 757 formulated as $Si_{2.45}Al_{.55}O_{.55}N_{3.45}$ + 5 w/o ZrO_2, falls in the β'-X-ZrN tetrahedron (phase composition 92.3 $Si_{2.54}Al_{.46}O_{.46}N_{3.54}$ + 1.9 $Si_3Al_6O_{12}N_2$ + 5.8 ZrN) whereas the formulation of sample 822, $Si_{2.7}Al_{.3}O_{.3}N_{3.7}$ - 5 w/o ZrO_2, correctly describes the equilibrium phase assemblage. Both compositions exhibited high creep rates at 1370°C (4×10^{-3} and $1.7 \times 10^{-3} hr^{-1}$ respectively) with the β'-ZrO_2 composition (822) exhibiting a rate less than half of that of the β'-15R-ZrN composition. Both compositions sintered to near theoretical density at temperatures around 1750°C. During the current reporting period compositions in the β'_{0-25}-$Si_3Al_6N_{10}$-ZrN and β'_{25-60}-15R-ZrN tetrahedron were prepared but the bodies did not sinter at 1750°C. In fact, they expanded on firing and exhibited large weight losses.

It can be concluded that sinterable β' based ceramic formulations occur only on the "oxide" side of the β' homogeneity line. The greatest extent of sinterable β' formulations lie in the β'_{10-60}-X-ZrN tetrahedron. Solidus temperatures appear to be low in this tetrahedron, and samples have little strength and creep resistance at 1370°C. At least some compositions lying on the

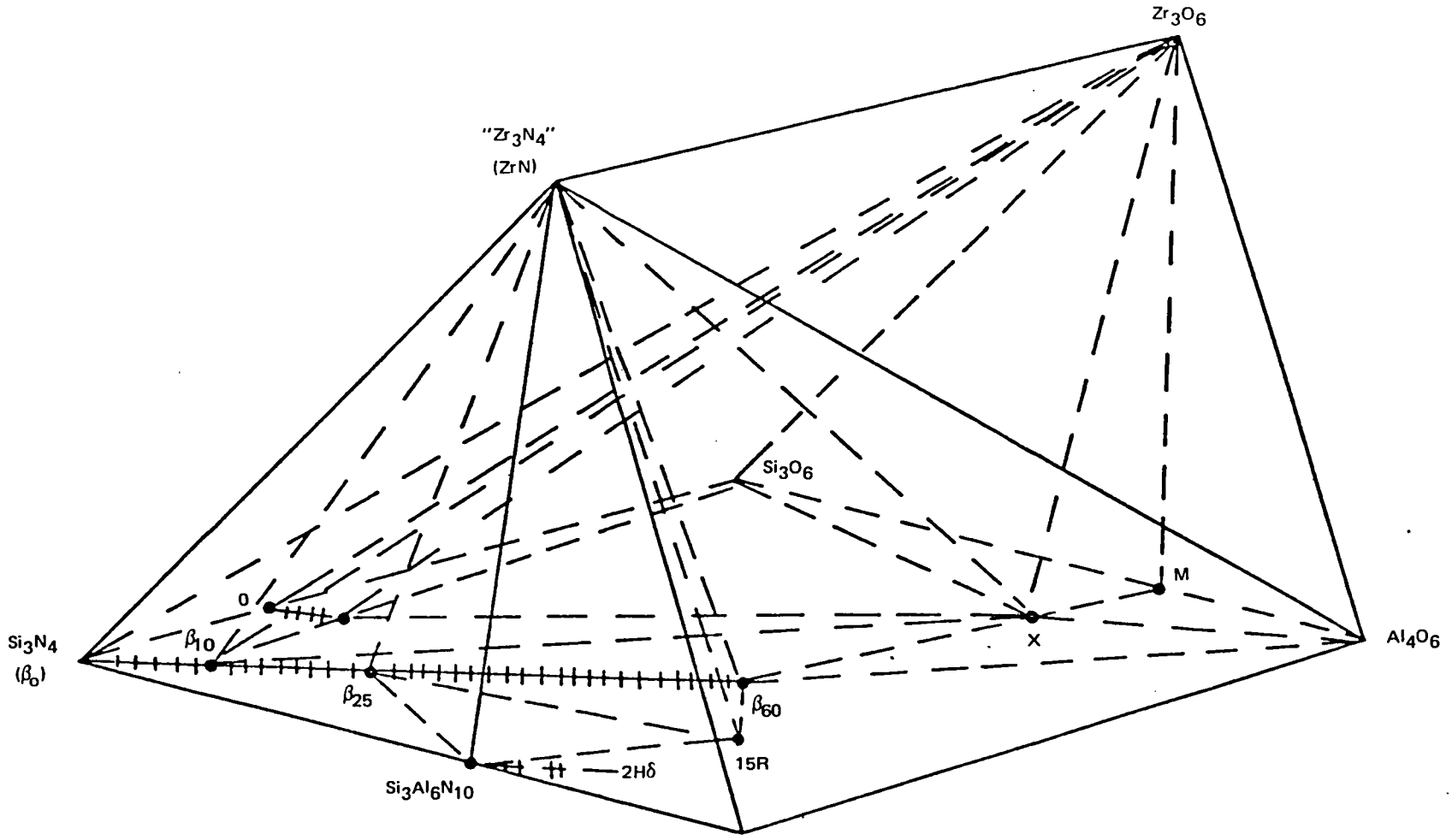

Figure 4. Probable Compatibility Relations (Partial) in the System Si_3N_4–Zr_3N_4–Al_4N_4–Al_4O_6–Zr_3O_6–Si_3O_6 at One Atmosphere Pressure of Nitrogen

TABLE 3

COMPATIBILITY TETRAHEDRA INVOLVING $Si_{3-x}Al_xO_xN_{4-x}$ SOLID SOLUTIONS IN THE Zr-Si-Al-O-N SYSTEM

3 Phase Equilibria	4 Phase Equilibria
1. $\beta'_{(0-10)}$-ZrN-ZrO_2	
2. $\beta'_{(0-10)}$-$O'_{(0-10)}$-ZrO_2	
	3. β'_{10}-O'_{10}-ZrO_2-X
	4. β'_{10}-ZrO_2-X-ZrN
5. $\beta'_{(10-60)}$-X-ZrN	
6. $\beta'_{(0-25)}$-ZrN-$Si_3Al_6N_{10}$	
	7. β'_{25}-ZrN-$Si_3Al_6N_{10}$-15R
8. $\beta'_{(25-60)}$-ZrN-15R	
	(9. β'_{60}-15R-ZrN-8H)
	(10. β'_{60}-ZrN-8H-Al_2O_3)
	(11. β'_{60}-ZrN-Al_2O_3-X)

$\beta'_{(0\text{-}10)}$-ZrO_2 plane (and presumably in the $\beta'_{(0\text{-}10)}$-$O'_{(0\text{-}10)}$-ZrO_2 and $\beta_{0\text{-}10}$-ZrO_2-Si_2N_2O tetrahedra) also sinter to theoretical density, but the composition tested ($Si_{2.7}Al_{.3}O_{.3}AlN_{3.7}$-5 w/o ZrO_2) also exhibited unacceptably high creep rate. If sinterable formulations with acceptably low creep rates are to be found in this system, they must have a β' composition very close to that of pure Si_3N_4.

B. System Y-Si-Al-O-N

1. Background

As with the Zr-Si-Al-O-N system described above, this system is best treated as a six component reciprocal system which can be visualized by replacing the components "Zr_3N_4" and Zr_3O_6 of Fig. with Y_4N_4 and Y_4O_6 respectively. Before describing experimental work in the system, the limiting binary, ternary and quarternary systems will be reviewed.

a) Binary Systems Y_2O_3-Al_2O_3 and Y_2O_3-SiO_2

The Y_2O_3-Al_2O_3 system has been investigated by a number of workers (Refs. 34, 35 and 26). Reference 34 shows the congrunetly melting compounds $3Y_2O_3$-$5Al_2O_3$ (YAG) and $2Y_2O_3.Al_2O_3$ (YAM) with the latter disproportionating below about 1000°C. References 35 and 36 do not indicate disproportionation of YAM, and show the additional $Al_2O_3.Y_2O_3$ phase, (YAP), having a narrow temperature range of stability between about 1830°C and the melting point around 1875°C. Reference 35 shows incongruent melting of YAP, while Ref. 36 indicates congruent melting. The system Y_2O_3-SiO_2 (Ref. 37) also contains three compounds, only two of which are stable at low temperature. These latter two compounds each exhibit several polymorphic forms; six modifications have been reported for the compound $Y_2Si_2O_7$, and four for Y_2SiO_5. The stability ranges of the various forms have not been firmly established. The crystal structure of the intermediate compound, $Y_4Si_3O_{12}$, which is reported to be stable from about 1650°C to its melting point at 1950°C, is the same as that of $Y_3Al_5O_{12}$ (YAG), suggesting the possibility of a solid solution between them at high temperatures.

b) The Ternary System Y_2O_3-Al_2O_3-SiO_2

This system has been studied by Bondar and Galakov (Ref. 38) who delineated the liquidus surface but not the solid phase compatibility. Their diagram has been redrawn in terms of equivalent percent and is presented as Fig. 5. From the position and the direction of falling temperatures of boundary curves between primary crystal fields, one can infer the solid phase compatibility relations at temperatures where the compounds $YAlO_3$ and $Y_4Si_3O_{12}$ are stable. Again, from

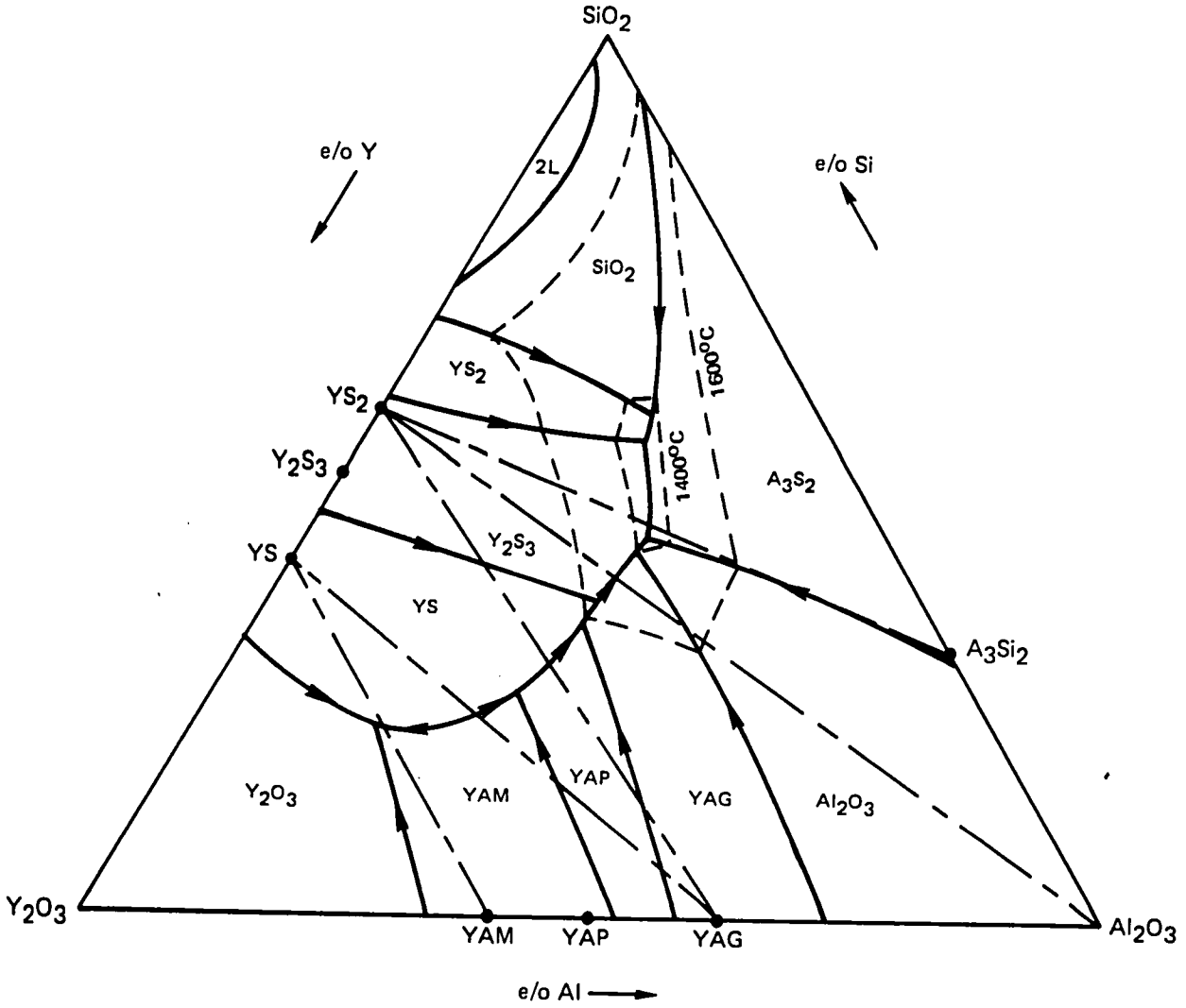

Figure 5 System–Y_2O_3–Al_2O_3–SiO_2 After Bondar and Galakov

79-04-137-6

the indicated temperatures on boundary curves, it can be inferred that the lower temperatures of stability of the $YAlO_3$ and $Y_4Si_3O_{12}$ phases are lowered somewhat in the ternary system suggesting some solid solubility in these phases. The extensive liquid region at 1600°C is noteworthy, as is the lowest ternary eutectic temperature of 1350°C. It can be anticipated that this liquid region would make a substantial incursion into the quinary system under consideration.

c) The ternary system YN-AlN-Si_3N_4

No information on this system was located.

d) The quaternary system Si_3N_4-SiO_2-Al_2O_3-AlN

This system was discussed earlier and shown as Fig. 3.

e) The quaternary system Si_3N_4-SiO-Y_2O_3-YN

Three investigations of this system have been reported (Refs. 20, 39 and 40). A composite diagram reflecting a consensus view of the system is shown in Fig. 6. This system will be discussed more fully in Section IVE.

f) The quaternary system Al_2O_3-Y_2O_3-YN-AlN

This system has been investigated by Rae et al. (Ref. 20) and Holmquist (Ref. 41). Both references agree that the compatibility relations at 1700°C are as shown in Fig. 7.

g) The quinary system

Rae et al. (Ref. 20) have studied compositions on the (nonternary) planes Al_2O_3-Y_2O_3-Si_2N_2O and Si_3N_4-Al_2O_3-Y_2O_3. On the former plane, they report solid solution between the "J" or N-YAM phase $Y_4Si_2O_7N_2$ (see Fig. 6) and $Y_4Al_2O_9$ (YAM), and between "K" or N-α-wollastonite phase $YSiO_2N$ and $YAlO_3$. Other than these quinary solid solutions, no new crystalline phases were observed in the system. Phase assemblages found by Rae (Ref. 20) on the plane Si_3N_4-Al_2O_3-Y_2O_3 are shown on Fig. 8.

During the course of our studies in the system, Naik and Tien (Ref. 42) presented the results of their studies of phase compatibility in the volume of the system bounded by phases β-Al_2O_3-Y_2O_3. Our earlier work in this volume of the system was presented in Ref. 22. The compatibility tetrahedra involving the β solid solution phase assigned by Naik and Tien and by Layden and Holmquist (Ref. 22) are compared in Table 4. These are essentially identical except for

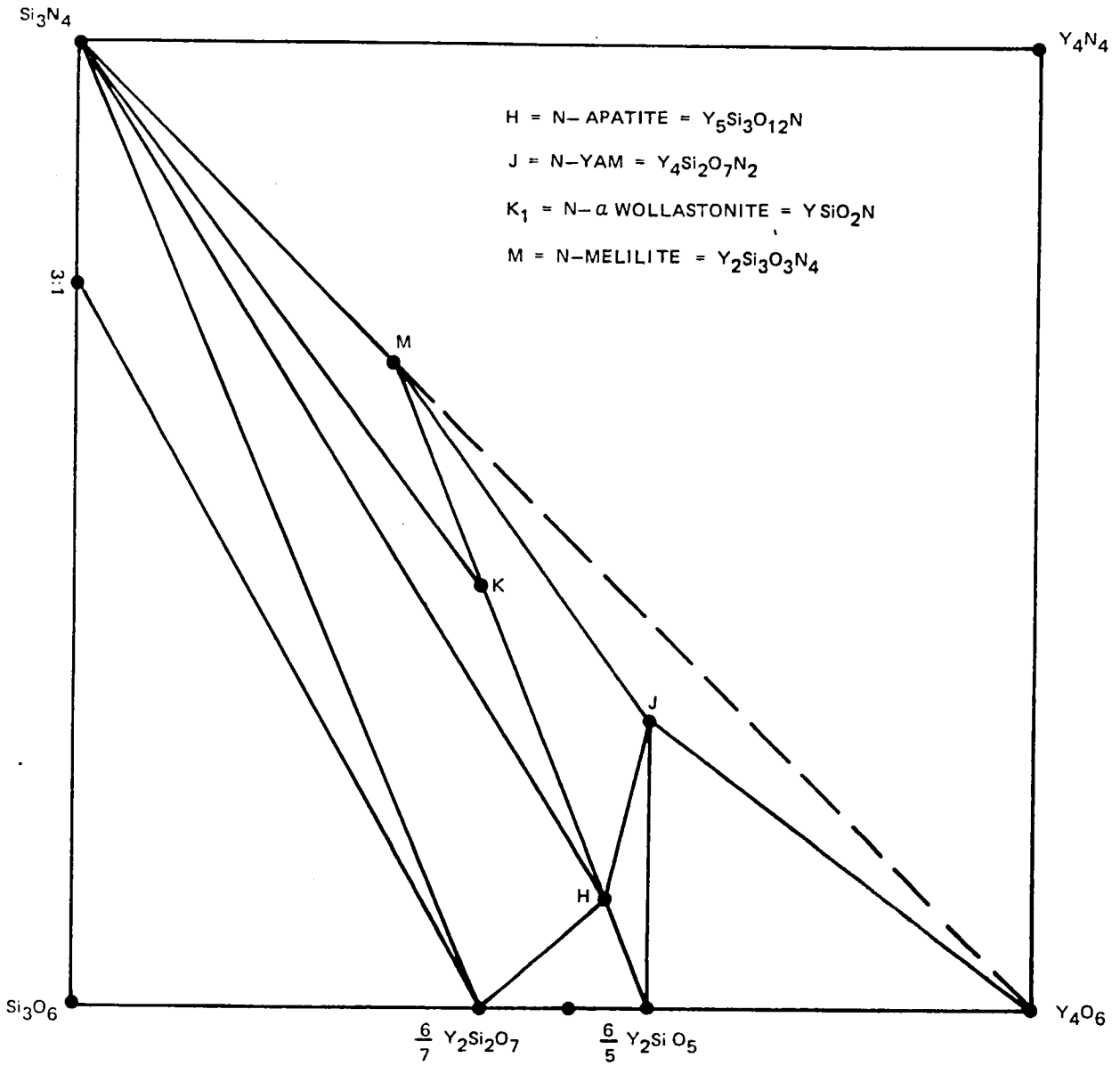

Figure 6 System $Si_3N_4 - SiO_2 - Y_2O_3 - YN$ (Composite)

78–03–67–2

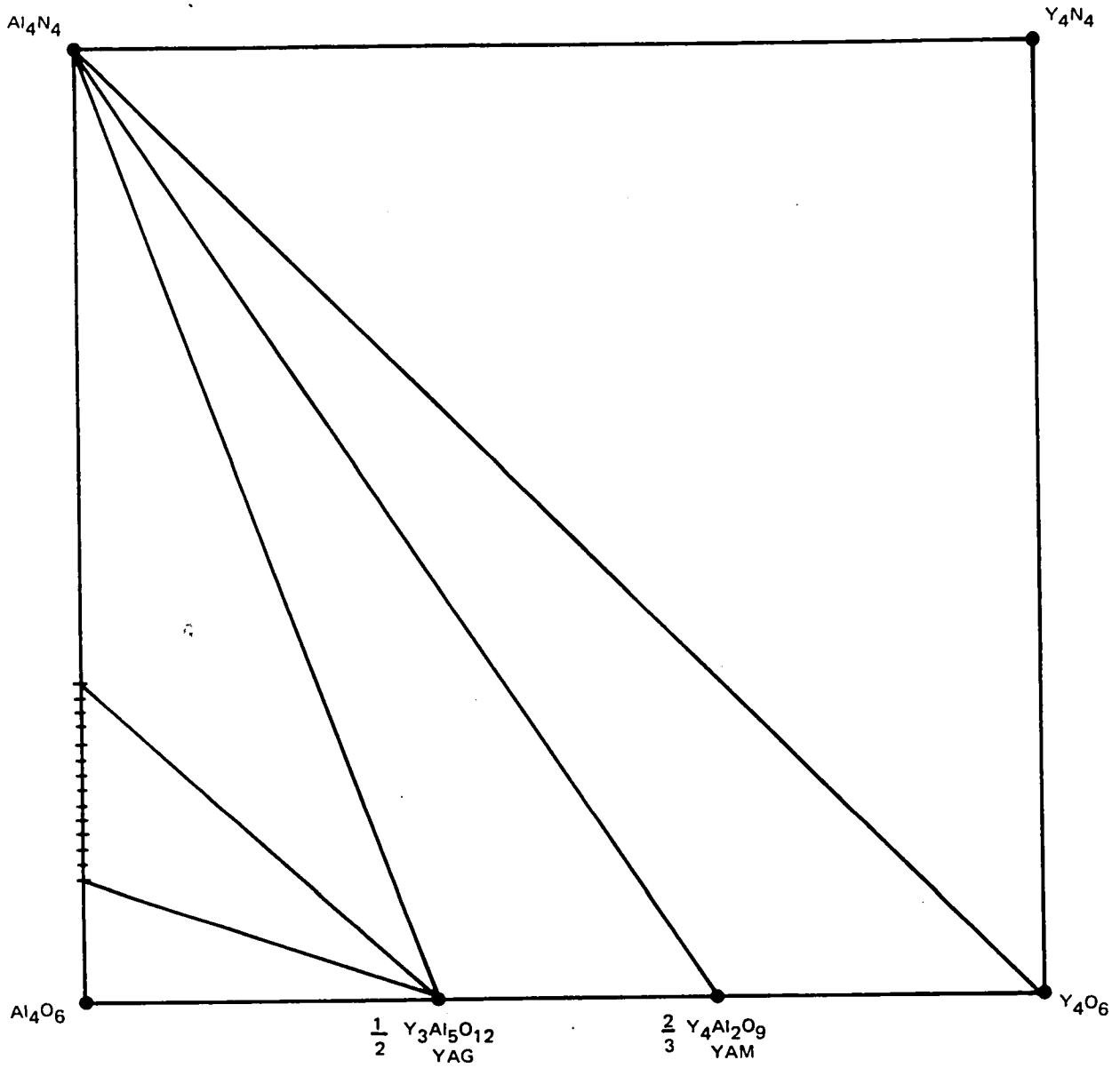

Figure 7 The System $A\ell_2O_3 - Y_2O_3 - YN - A\ell N$

78–03–67–3

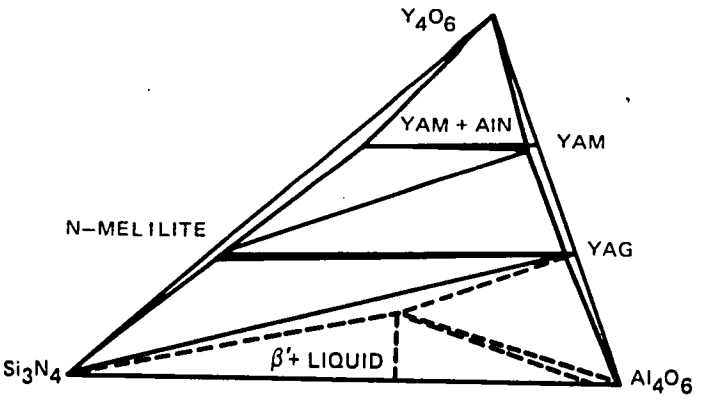

A. 1700°C

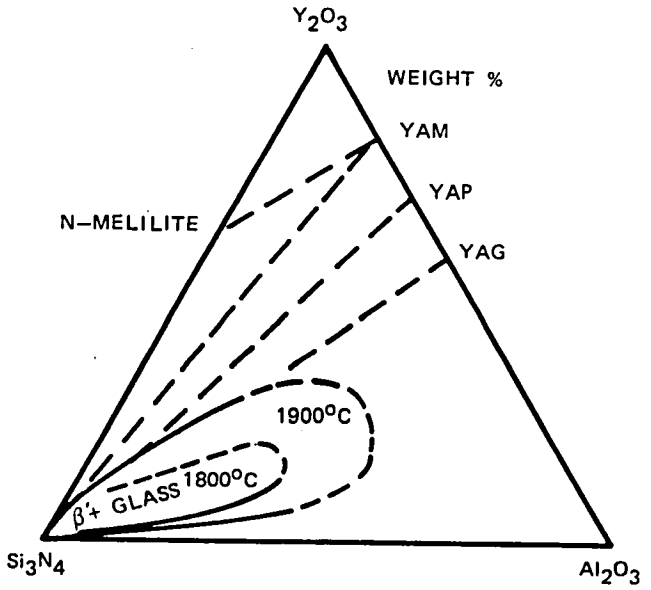

B. 1800 AND 1900°C

Figure 8 Phase Assemblages at Different Temperatures in the System Y_2O_3 – Al_2O_3 – Si_3N_4 After Rae et al (ref 20)

78-04-12-1

TABLE 4

COMPARISON OF PROPOSED β PHASE
COMPATIBILITY TETRAHEDRA IN THE Y-Si-Al-O-N SYSTEM

Naik and Tien	Layden and Holmquist
β_{0-60} - YS_2 - YAG	β_{0-60} - YAG - X
β_{10-60} - YS_2 - X	
β_{60} - YS_2 - X - YAG	β_0 - YS_2 - X - YAG
β_{60} - Al_2O_3 - X - YAG	β_{60} - Al_2O_3 - X - YAG
β_{10} - O_b - YS_2 - X	β_0 - O_o - YS_2 - X
β_{0-10} - O_{o-b} - YS_2	(ignored solubility limits)
β_0 - YAG - YS_2 - H	β_0 - YAG - YS_2 - H
β_0 - YAG - H - K	β_0 - YAG - H - K
β_0 - YAG - K - M	β_0 - YAG - K - M

Code:

β_{a-b} - all compositions from a to b e/o Al

YS_2 - $Y_2Si_2O_7$

YAG - $Y_3Al_5O_{12}$

H - $Y_{10}Si_6O_{24}N_2$

K - $YSiO_2N$

M - $Y_2Si_3O_3N_4$

O - Si_2N_2O(ss)

X - $Si_3Al_6O_{12}N_2$ (ss)

the subvolume bounded by the phases β'-$Y_2Si_2O_7$-$Y_3Al_5O_{12}$-X within which Naik and Tien established the tie line β_{60}-$Y_2Si_2O_7$ not observed by Layden and Holmquist. After examining the data of Naik and Tien we agree that this tie line should be included.

2. Experimental Investigation

a) Representation

While the Zr-Si-Al-O-N system could be depicted with reasonable clarity by the use of a perspective drawing (Fig. 4), this becomes virtually impossible in the case of the Y-Si-Al-O-N system because of the greater complexity of the bounding systems. For this reason a plexiglas model in the shape of an equilateral triangular prism was made. Transparencies of the various bounding systems were produced to the proper scale and fastened to the appropriate faces of the model. Holes were drilled through the model at the locations of the various phases, and thread was used to connect different points in the model in order to delineate various joins.

b) Results

Compositions prepared specifically for phase studies, conditions of firing, and tests results, are presented in tabular form in Appendix A. In general, substantial shrinkage during firing was an indication that partial melting had occurred. Nominally identical compositions prepared from different starting materials fired under similar conditions frequently exhibited rather different behavior and resulted in different phase assemblages in the fired bodies. A good example of this is found in data in Appendix A for samples located along the $Y_3Al_5O_{12}$ - "$Y_3Si_5O_7N_5$" join. This was particularly the case where substantial melting and bloating of samples were observed. It was also clear that in many instances a substantial amount of glass was retained in the samples at room temperature. As well as the data in Appendix A, phase data obtained from earlier, and subsequent test bars, were also considered in assessing phase compatibility. These data are found in tables in appendices B and C, and will be discussed when the physical property data for the various samples are discussed.

In regard to identification of the various AlN polytypes, we have used the notation of Jack (Ref. 7). However, with the exception of the 15R phase, identification of the X-ray diffraction patterns was made on the basis of X-ray data published by Land et al. (Ref. 4). It is clear that phases designated by Land as θ, η, ε, are the phases designated by Jack as 8H, 15R and $2H^{\delta}$ respectively. It is not clear to which of the 3 remaining polytypes listed by Jack the Land ξ phase corresponds.

In constructing the model of the system, coexisting crystalline phases revealed by the data in the appendices were assumed to be compatible, and the points representing the compositions of these phases were connected by thread. As well as our own data, that of Rae et al. (Ref. 20) and Naik and Tien (Ref. 42) were used. The resulting model is shown as Fig. 9. Only tie lines relevant to equilibria involving the β solid solution phase have been included. Not shown on the model is the 8H phase which was not unambiguously identified in our samples. However topographical considerations would appear to necessitate a tie line between this phase and $Y_3Al_5O_{12}$, thus leading to two additions 4 phase tetrahedra involving β_{60} ($SiAl_2O_2N_2$) not delineated on the model. Likewise, we have not drawn a tie line between the $Y_2Si_3O_3N_4$ phase and YN which would be required if in fact no binary compounds occur between either Y_2O_3 are YN on YN and Si_3N_4. This tie line would delineate the final tetrahedron involving Si_3N_4.

A list of the three and four phase tetrahdra delineated by the model (plus the three not delineated, but assumed to exist, and listed in parenthesis) are listed in Table 5.

C. Properties of Bodies in the Y-Si-Al-O-N System

1. Primary Data

The formulations for various batches from which test samples were prepared are listed in Appendix B. Tables in Appendix B include information relating to raw materials and processing techniques used in the batch preparations. Unless otherwise stated there, the Si_3N_4 component was KBI powder. Fabrication, density, and mechanical test data for fired test specimens, are listed in Appendix C and oxidation data are presented in tables or curves in Appendix D. The above named appendices present data for samples from many different phase systems and are arranged chronologically. Data for Y-Si-Al-O-N samples were collected from the various appendices and compositions have been recalculated from the actual batch components (including grinding media pick-up where relevant) in terms of equivalent percent Al, Y, and O, and also in mole percent of the equilibrium phases based on the compatibility relationships shown in Fig. 9 and Table 5. These batch compositional data are presented in Table 6. Also shown in Table 6 are code symbols denoting the equilibrium phase assemblage. A quick glance at Table 6 shows that most of the samples investigated fall into one of the three phase tetrahedra which involve broad ranges of β solid solution, as opposed to the four phase tetrahedra which involve unique β compositions. In general, the 4 phase tetrahedra may be considered peripheral to the main area of interest in the system.

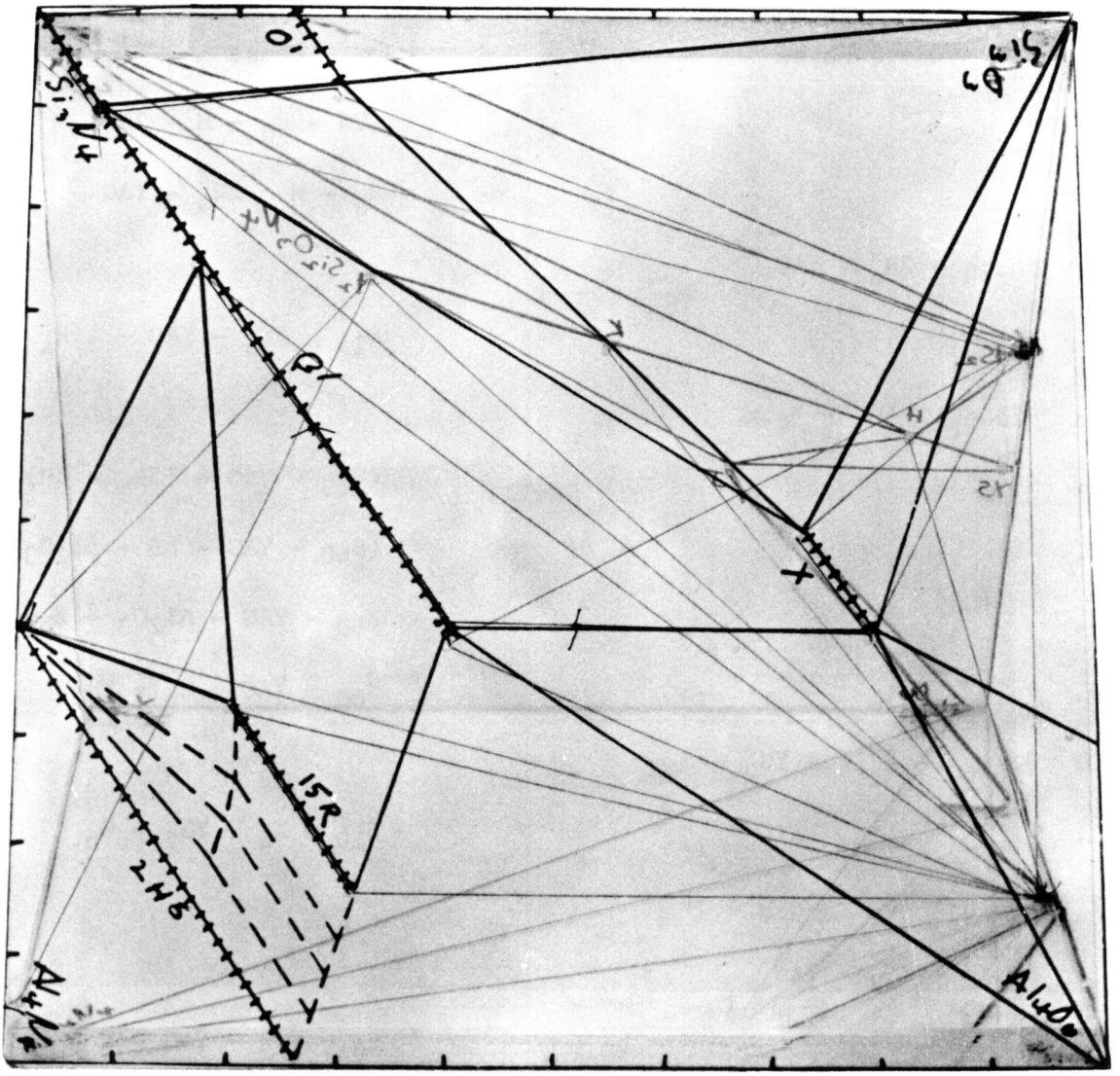

Figure 9 Model of the Y–Si–Al–O–N System

79–04–137–1

TABLE 5

PROPOSED COMPATIBILITY TETRAHEDRA INVOLVING
$Si_{3-x}Al_xO_xN_{4-x}$ (β' SOLID SOLUTIONS) IN THE SYSTEM Y-Si-Al-O-N

	3 Phase	4 Phase
1.		(YN - β_o - M - $2H_o^\delta$)
2.		β_o - M - $2H_o^\delta$ - YAG
3.	β_{0-25} - $2H_o^\delta$ - YAG	
4.		β_{25} - $2H_o^\delta$ - YAG - $15R_a$
5.	β_{25-60} - YAG-$15R_{a-b}$	
6.		(β_{60} - YAG - $15R_b$ - 8H)
7.		(β_{60} - YAG - 8H - Al_2O_3)
8.		β_{60} - YAG - Al_2O_3 - X_b
9.		β_{60} - YAG - X_b - YS_2
10.	β_{10-60} - X_{a-b} - YS_2	
11.		β_{10} - X_a - YS_2 - O_b
12.	β_{0-10} - YS_2 - O_{o-b}	
13.	β_{0-60} - YS_2 - YAG	
14.		β_0 - YS_2 - YAG - H
15.		β_0 - YAG - H - K
16.		β_0 - YAG - K - M

β_{a-b} - all composition from a to b e/o Al
YS_2 - $Y_2Si_2O_7$
YAG - $Y_3AL_5O_{12}$
H - $Y_{10}Si_6O_{24}N_2$
K - $YSiO_2N$
M - $Y_2Si_3O_3N_4$
O - Si_2N_2O (ss)

X - $Si_3Al_6O_{12}N_2$ (ss)
15R - $SiAl_4O_2N_4$(ss)
$2H_o^s$ - $Si_3Al_6N_{10}$
8H - $Si_3Al_{16}O_{12}N_{12}$ (ss)

TABLE 6

PHASE COMPOSITIONS OF TEST SAMPLES IN THE Y-Si-Al-O-N SYSTEM

Composition Designation (Appendix B)	Equivalent Percent			Symbol	Equilibrium Phase Composition (mole percent) (1)										
					β $Si_{3-x}Al_xO_xN_{4-x}$										
	Al	Y	O		m/o	x	c/o Al	YAG	YS_2	$2H^{\delta}_{o}$	15R	II	M	O'(2)	X
β'_1 + 2.5 w/o Y_2O_3	7.62	0.82	5.74	▽	98.5	0.227	5.8	1.0		0.5					
β'_1 + 5 w/o Y_2O_3	7.56	1.63	6.78	▽	96.8	0.146	3.7	2.3		0.9					
β'_2 + 2.5 w/o Y_2O_3	13.62	0.79	9.60	▽	98.5	0.486	12.7	1.0		0.5					
β'_2 + 5 w/o Y_2O_3	14.14	1.64	10.75	▽	96.6	0.386	10.0	2.3		1.0					
1078	1.04	9.61	16.23	▲	90.6	0	0	1.0	0.8			7.6			
1079	3.93	4.22	10.73	△	92.8	0	0	3.3	3.9						
1080	11.50	5.13	19.6	◇	90	0.500	13.0		10						
1081	23.90	5.31	28.3	◇	90	1.00	27.3		10						
1085	6.00	3.06	9.5	▷	95	0	0	5							
1086	32.03	3.81	25.33	▷	95	1.0	27.3	5							
1087	60.27	4.22	46.73	▷	95	2.0	60	5							
1088	4.82	3.37	8.88	△	95	0	0	4	1						
1089	3.70	3.31	8.06	△	95	0	0	3	2						
1090	3.03	2.97	7.30	△	95	0	0	2	3						
1091	27.65	1.35	18.78	▼	96.7	0	0	0.7		1.1			1.5		
1103	4.77	2.98	10.60	□	93.4	.165	4.2		6						0.6
1104	43.13	1.95	13.64	▷	97.5	1.0	27.3	2.5							
1105	27.52	1.38	19.43	▢	93.1	0.82	22.0	1.7			5.2				
1111	2.79	4.32	10.99	△	93.7	0.05	1.3	4.9	1.4						
1112	2.28	2.92	7.47	○	85.9	0.14	3.5		2.8					11.3	
1114	12.64	2.55	12.38	△	96.4	0.364	9.4	2.8	0.8						
1115	25.91	1.21	14.40	▽	93.3	0.74	20.0	1.7		5.0					
1116	3.01	1.53	9.63	○	86.5	0.1	2.5		5.7					7.8	
1118	20.76	0.97	2.16		79.5	0	0			17.9			2.6		

(1) Codes were presented in Table 5.

(2) In calculating composition it was assumed that the O' phase had the same equivalency aluminum substitution as the β' phase.

Test data abstracted from the appendices are summarized in Table 7. Oxidation data are expressed as parabolic rate constants, even though reference to the primary oxidation data shows that oxidation was not necessarily parabolic. Such numbers were generally calculated from the total weight gain per unit area for the accumulated exposure time. This was done simply to give a number to plot that expresses in a qualitative way the oxidation rate relative to our program goals. The numbers become quantitative as they became small (on the order of 0.05 $mg^2cm^{-4}hr^{-1}$).

2. Graphical Presentation of Property Data

a. Equivalent Percent Representation

It is desirable to have a method for displaying composition points for the quinery system on a single plane, so that property data can be plotted as functions of composition. This can be accomplished by plotting the cation equivalent percentage on triangular coordinate paper. This in effect projects all composition points onto a plane. The composition of each point can then be specified by labeling it with either a number corresponding to the equivalent percent oxygen, or a symbol corresponding to the equilibrium phase assemblage. The latter method has been adopted in the following plots, since this reserves the use of numbers for presenting property data.

To illustrate the plotting of compositions in this way, consider compositions in the compatibility tetrahedra β'-YAG-YS_2 (i.e., $Si_{3-x}Al_xO_xN_{4-x}$ - $Y_3Al_5O_{12}$-$Y_2Si_2O_7$). Projections of these phases are shown in Fig. 10. The point A could represent for instance:

1. a binary mixture of $\beta'_{(x=1)}$ and $Y_3Al_5O_{12}$
2. a binary mixture of $\beta'_{(x=1.5)}$ and $Y_2Si_2O_7$, or
3. ternary mixtures of $\beta_{(1 < x < 1.5)}$, $Y_3Al_5O_{12}$ and $Y_2Si_2O_7$.

An appropriate symbol placed at point A would then serve to identify the given phase assemblage (symbols were given in Table 6).

An advantage of this type of representation is that it can be used to project every composition in the quinery system directly onto the phase diagram for the ternary system Al_2O_3 - Y_2O_3 - SiO_2, i.e., the system which contains its oxidation products. This is a help in understanding the oxidation behavior of bodies as functions of composition.

TABLE 7

SUMMARY OF PROPERTY DATA FOR Y-Si-Al-O-N SAMPLES

Designation (Appendix B)	Apparent Porosity (%)	Bulk Density (g/cc)	Oxidation Data: Test Temp. (°C)	Oxidation Data: Rate Constant $mg^2cm^{-4}hr^{-1}$	Flexural Strength Data: Test Temp. (°C)	Flexural Strength Data: Range (ksi)	Flexural Strength Data: Number of Tests	Flexural Strength Data: Mean Value (ksi)	Flexural Strength Data: Mean Value MPa	1370°C, 69MPa Creep Rate (hr^{-1})
β'1+25%Y_2O_3	< 1	3.04	1400	0.3	25	63-8	5	67	464	
					1370	42-65	2	54	373	
β'1+5%Y_2O_3	< 1	3.20	1400	0.1						
β'2+2.5%Y_2O_3	< 1	3.26	1400	0.5						
β'2+5%Y_2O_3		3.26	1400	0.6	25	37-85	14	59	407	$6x10^{-5}$
			1300	0.003	1370	47-51	3	49	338	
			1000	0.0000						
1078	< 1	3.51	1400	0.15						
			1000	0.10						
1079	4	3.25	1400	0.23						
			1000	0.0005						
1080	0	3.36	1400	16						
			1000	0.0000						
1081	0	3.24	1400	17						
1085	< 1	3.14	1400	17						
1086	1	3.11	1400	0.3						
1088	< 1	3.23	1400	0.99						
			1400*	0.78						
1089	1	2.71	1400	0.47						
			1400*	0.39						
1090	1	2.96	1400	0.37						
			1400*	0.31						
1091			1400	0.005						
1103	< 1	3.25	1400	2.3						
			1300	0.03						
1104	< 1	3.12	1400	0.033						
			1300	0.003						
1105	< 1	3.21	1400	0.010	25	38-58	5	48	331	$2.4x10^{-3}$
			1370	0.005	25**	34-60	8	48	331	
			1300	0.001	25***	28-43	5	34	235	
			1000	0.0000						
1111	0	3.40	1400	0.6						
1112	0	3.07	1400	0.2						
1114	0	3.19	1400	0.8						
1115	0	3.09	1400	0.016	25	34-48	4	40	276	
			1000	0.0000	25***	25-35	3	29	200	
1116	< 1	3.25	1400	3.0						

*Following heat treatment in nitrogen at 1400°C for 64 hrs.
**Following heat treatment in air at 1300°C for 100 hrs.
***Following heat treatment in air at 1370°C for 100 hrs.

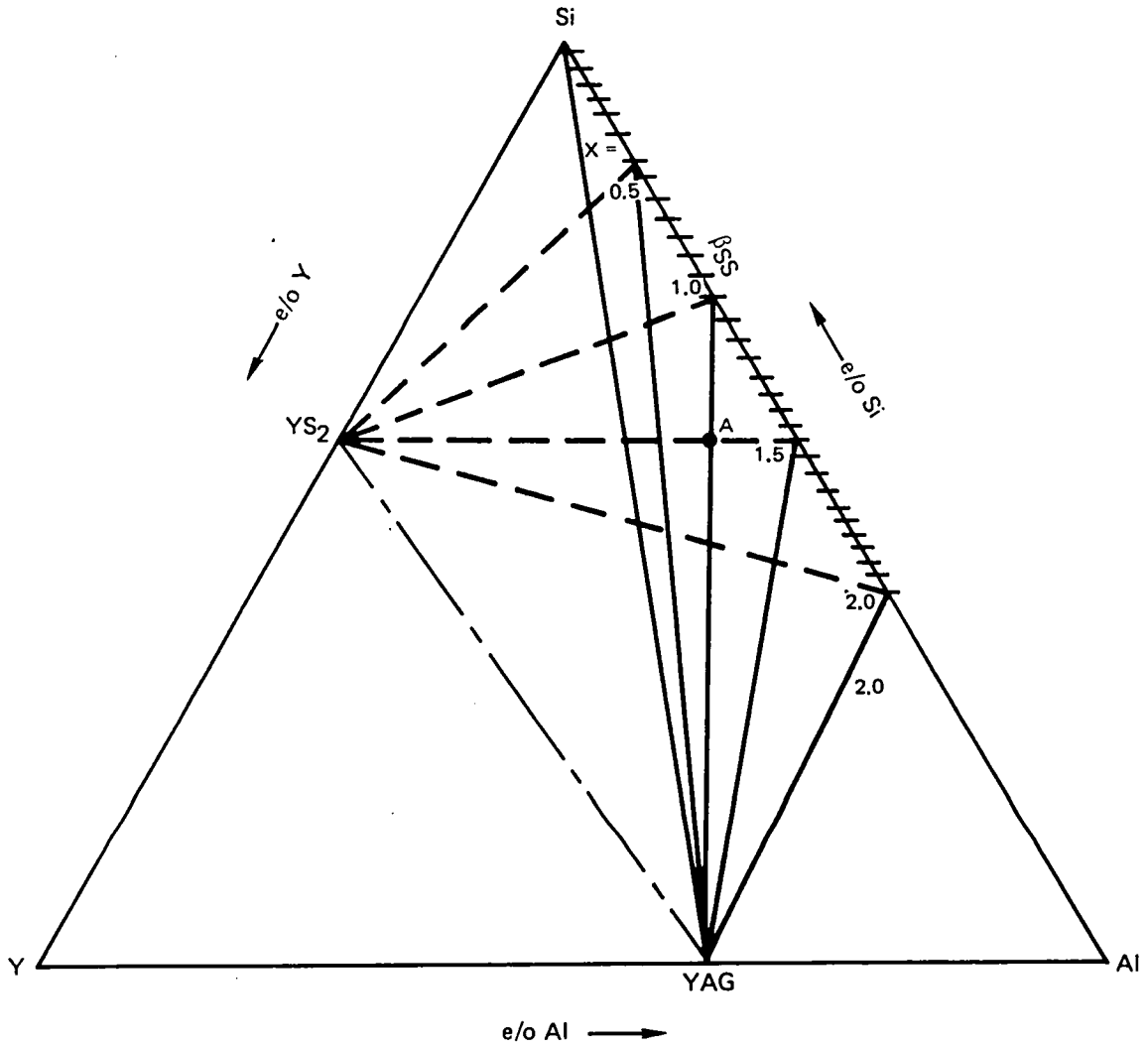

Figure 10 Planar Projection of the $\beta'_{(0-60)}$–YAG–YS_2 Tetrahedron

79-04-137-2

3. Densification

$Si_{3-x}Al_xO_xN_{4-x}$ bodies could not be sintered to greater than about 85 percent of theoretical density by firing to 1750°C, although β'-X phase bodies could be readily sintered to over 98 percent of theoretical density as a result of the presence of a liquid phase at the sintering temperature (Ref. 12). Liquid formation can also be promoted by the addmixture of Y_2O_3 and Y_2O_3-SiO_2 to Si_3N_4 and β' compositions. However, in the absence of Al_2O_3 (or other fluxing oxides such as BeO and CeO_2) the liquid which forms is not effective in promoting densification unless external pressure is applied to the system (i.e., hot pressing). In terms of the ternary projection of quinery compositions discussed in the previous section, it can be stated that compositions which project onto the Y-Si join cannot be sintered to high density, nor can compositions which project onto the Al-Si join, with the exception of compositions in the B'-X phase field. Between the two bounding regions there is a wide range of compositions which can be readily sintered to near theoretical density, as can be seen from table 7. The compositional limits within which densification can be effected at temperatures of 1750°C and below are about the 1 e/o aluminum line (in the absence of X phase) and 1 e/o yttrium line.

The effectiveness of Y_2O_3-Al_2O_3 addmixtures in sintering Si_3N_4 based bodies is certainly related to the formation of relatively low melting liquids which readily wet-out the β phase. How low in temperature liquid forms in parts of the quinery system can be judged from the fact that compositions lying on the β' -YS_2 plane (compositions 1080 and 1081, Appendix C and Table 7) sintered to high density at 1500°C. Compositions in the tetrahedron Si_3N_4-YAG-YS_2 (1088, 1089 and 1090) appeared to consist of β' and liquid (glass at room temperature) at temperatures at least as low as 1400°C.

4. Oxidation of Y-Si-Al-O-N Samples

a. 1400°C Oxidation

The phase diagram for the system Al_2O_3 - Y_2O_3 - SiO_2 was shown as Fig. 5. The 1400°C isothermal section drawn from Fig. 5 is presented in Fig. 11. The 1400°C oxidation rate data from Table 7 are plotted as described earlier, using the composition symbols given in Table 6, on the relevant portion of the Al_2O_3 - Y_2O_3 - SiO_2 1400°C isothermal section in Fig. 12. Also plotted on Fig. 12 are oxidation rate data for two phase β'-X phase bodies from Ref. 12 which project onto the Si-Al join, and data for Y-Si-Al-O-N samples reported by Arias (Ref. 43) and Dutta (Ref. 44). It can be seen that, except for compositions which project onto the Si-Al or Si-Y joins, all compositions will have oxide scales at 1400°C which contain some liquid. The equilibrium phase

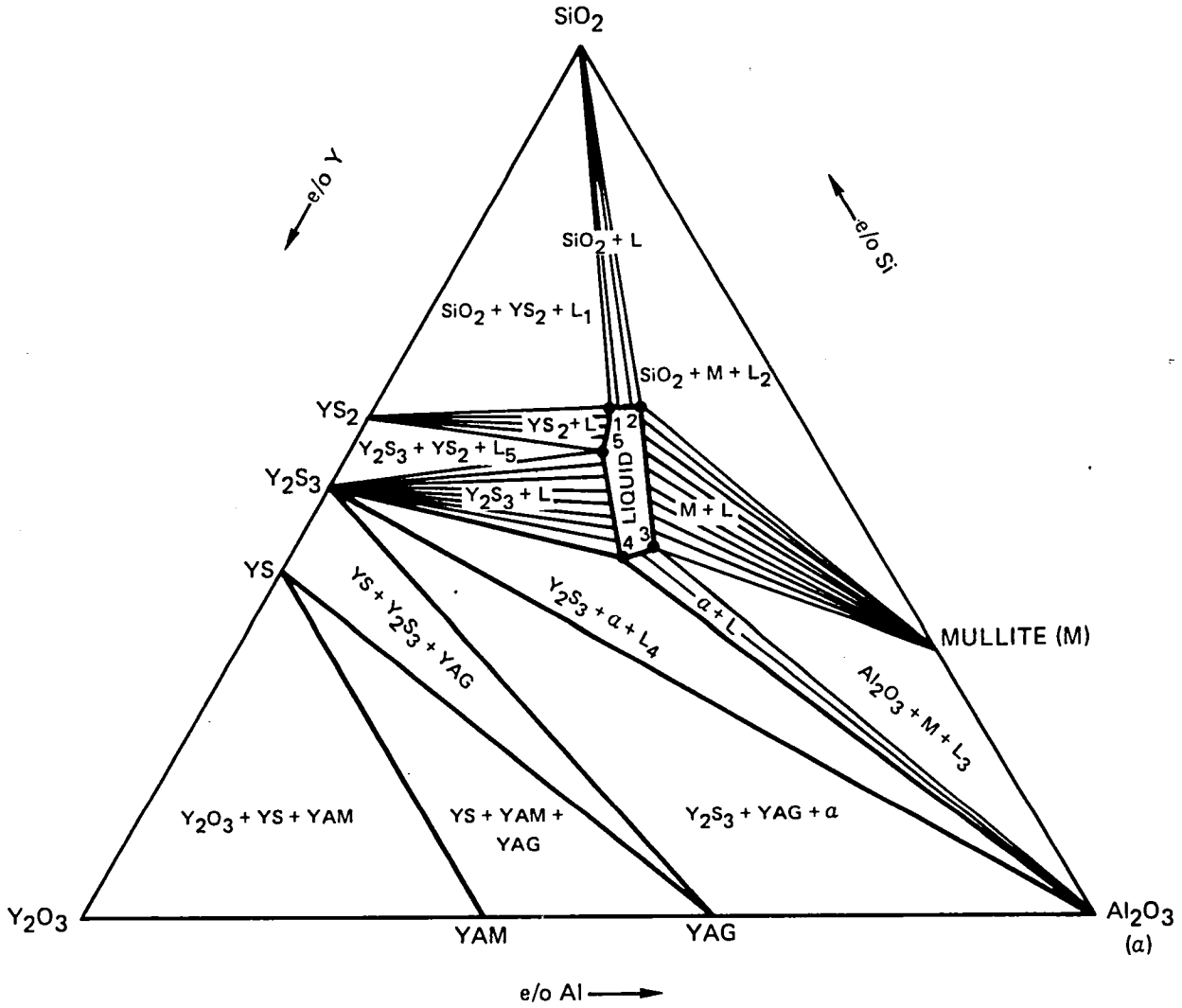

Figure 11 1400°C Isothermal Section of the Al_2O_3–Y_2O_3–SiO_2 System

79–04–137–3

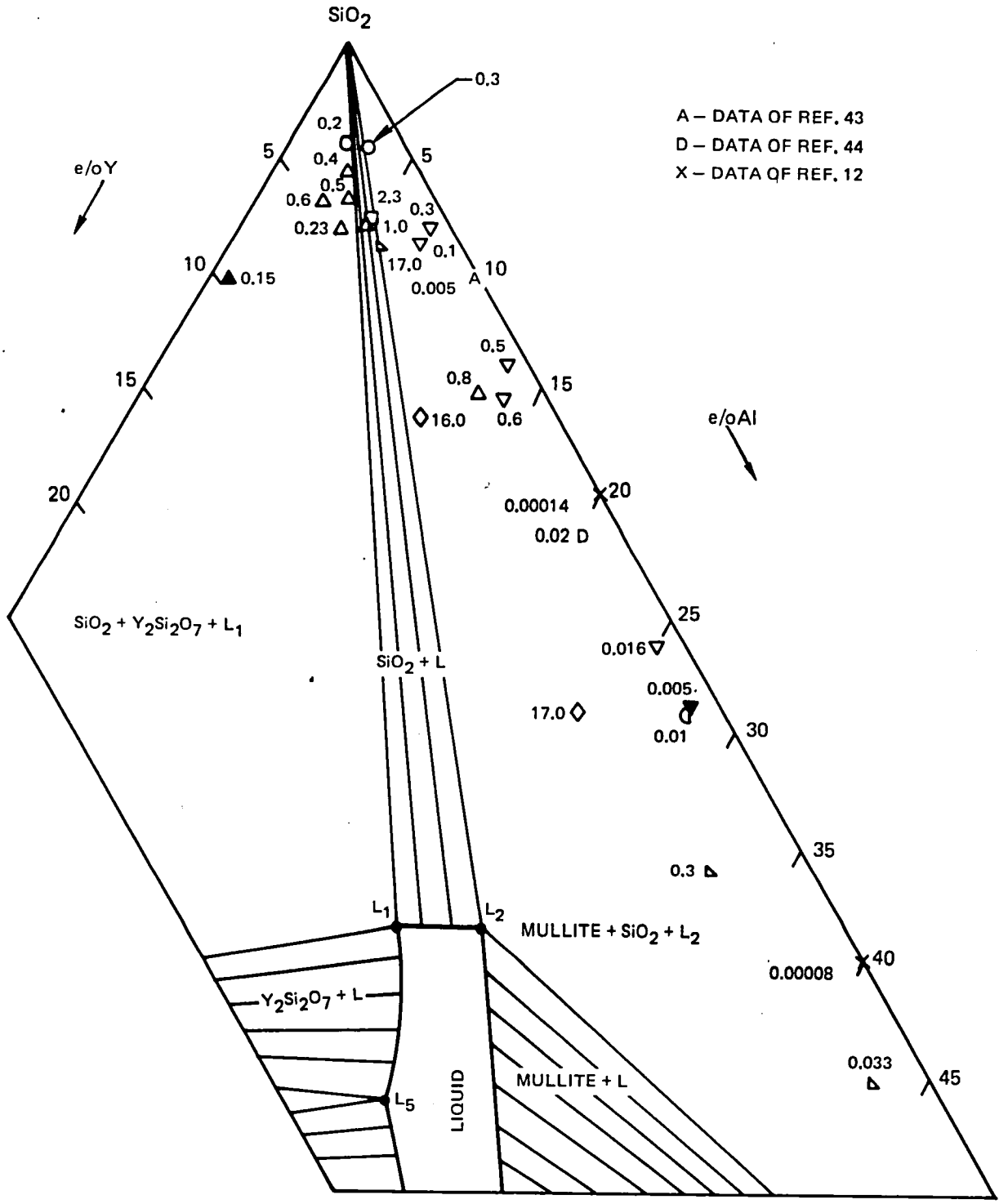

Figure 12 1400°C Oxidation Rate Constants ($mg^2\ cm^{-4}\ hr^{-1}$) for Samples in the Y–Si–Al–O–N System, Plotted on the 1400°C Isothermal Section of the Al_2O_3–Y_2O_3–SiO_2 Phase Diagram (Symbols Defined in Table 6)

79-04-137-4

compositions of scales can be readily calculated. A simple way to do this is to express all relevant compositions in terms of a constant valence (e.g., ± 4). Such formulations for SiO_2, mullite, yttrium disilicate, and the liquids L_1 and L_2, along with their molecular weights and densities* (needed to convert mole percent into volume percent) are presented in Table 8. Coefficients for chemical equations of the type:

$$Y_xAl_ySi_zO_2 = aSiO_2 + b(Y_{.571}Si_{.571}O_2) + c(Y_{.240}Al_{.305}Si_{.590}O_2)$$

are then determined to calculate mole percent of the phases. The calculated phase compositions for scales for some representation compositions, and their oxidation rate constants, are presented in Table 9. Micrographs of polished sections through the scales of these same samples are shown in Figs. 13 and 14. In general, the data plotted in Fig. 12 indicate that high concentrations of cristobalite and liquid in the scales result in high oxidation rates. By far, the overriding effect is that of liquid concentration. Thus composition 1080.2, which by calculation, and by rough visual assessment of Fig. 13-B, has a scale consisting of about 29 percent liquid, 68 percent cristobalite and 3 percent mullite (only cristobalite was detected by XRD) oxidized extremely rapidly. The scale was virtually nonprotective, despite the great thickness (250 μ) that built up in only 1.24 hours of exposure, attesting to the rapid diffusion of oxygen through the liquid.

Samples having scales with lower calculated liquid concentrations, but relatively higher cristabalite concentrations, exhibited intermediate rates (but still excessive in terms of performance requirements), with the rate decreasing with decreasing liquid and cristobalite concentrations, as seen from the data for samples 1078.1 (Fig. 13A) and 1111.1 (Fig. 14B). Another effect apparently unrelated to scale composition per se is evident from the micrograph of sample 1078.1. This shows the generation of subscale porosity apparently associated with diffusional processes (grain boundary?) and internal oxidation. It will be seen later that this composition also oxidizes badly at 1000°C as well).

In contrast to the above examples, sample 1105.1, Fig. 14A, with a low liquid, intermediate (but still major) cristobalite, and a substantial mullite concentration (about 30 percent) in the scale exhibited a low oxidation rate. The scale was protective, and built to a thickness of about 25 μ in 96 hours of exposure. This is generally seen to be the case: the only sintered samples studied which had nominally acceptable oxidation rates at 1400°C (on the order of 0.01 $mg^2cm^{-4}hr^{-1}$) were those samples which exhibited scales with high concentrations of mullite (about 30 percent or

*Densities of the liquids were estimated by extrapolation of the density data of Bacon (Ref. 45) for yttrium bearing glasses.

TABLE 8

SOME EQUIVALENT FORMULATIONS, MOLECULAR WEIGHTS, AND DENSITIES FOR SOME OXIDE PHASES

Conventional Formula	Equivalent Formula	Molecular Weight	Density (g/cc)
SiO_2	SiO_2	60.1	2.3
$Al_6 Si_2 O_{13}$	$Al_{.923} Si_{.308} O_2$	65.5	3.15
$Y_2 Si_2 O_7$	$Y_{.571} Si_{.571} O_2$	98.8	4.15
Liquid L_1	$Y_{.240} Al_{.306} Si_{.59} O_2$	76.6	$\sim$ 3.8
Liquid L_2	$Y_{.200} Al_{.347} Si_{.590} O_2$	75.7	$\sim$ 3.8

TABLE 9

CALCULATED VOLUME PERCENT PHASES IN 1400°C
OXIDE SCALES ON SOME Y-Si-Al-O-N SAMPLES

Composition Number	Equivalent Percent Al	Y	O	Equivalent Formulation	Volume Percent of Phase in Scale SiO_2	$Y_{.571}Si_{.571}O_2$	$Al_{.923}Si_{.308}O_2$	L_1	L_2	Oxidation Rate Constant ($mg^2cm^{-4}hr^{-1}$)
1078	1.04	9.61	16.23	$Y_{.128}Al_{.014}Si_{.894}O_2$	77.0	19.1	0	3.9	0	0.15
1080	11.50	5.13	19.60	$Y_{.068}Al_{.153}Si_{.834}O_2$	68.2	0	3.3	0	28.5	16.0
1105	27.52	1.38	19.43	$Y_{.018}Al_{.367}Si_{.771}O_2$	60.4	0	32.1	0	7.5	0.01
1111	2.79	4.32	10.99	$Y_{.058}Al_{.037}Si_{.930}O_2$	89.4	4.0	0	6.6	0	0.6

a) SAMPLE 1078.1 OXIDIZED 96 HOURS AT 1400°C

100μ

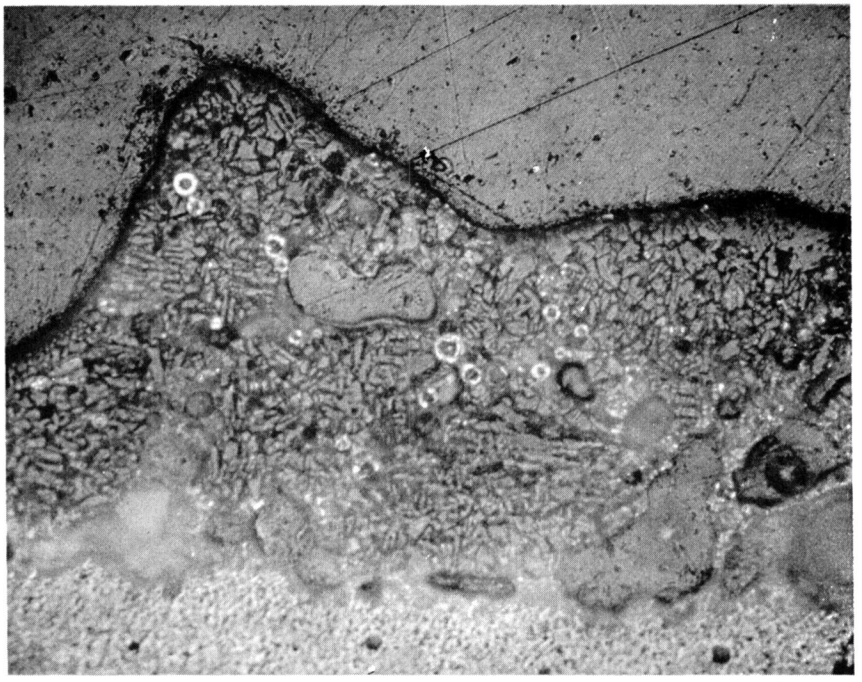

b) SAMPLE 1080.2 OXIDIZED 1.25 HOURS AT 1400°C

50μ

Figure 13 Oxide Scales on Samples 1078.1 and 1080.2

79–04–137–10

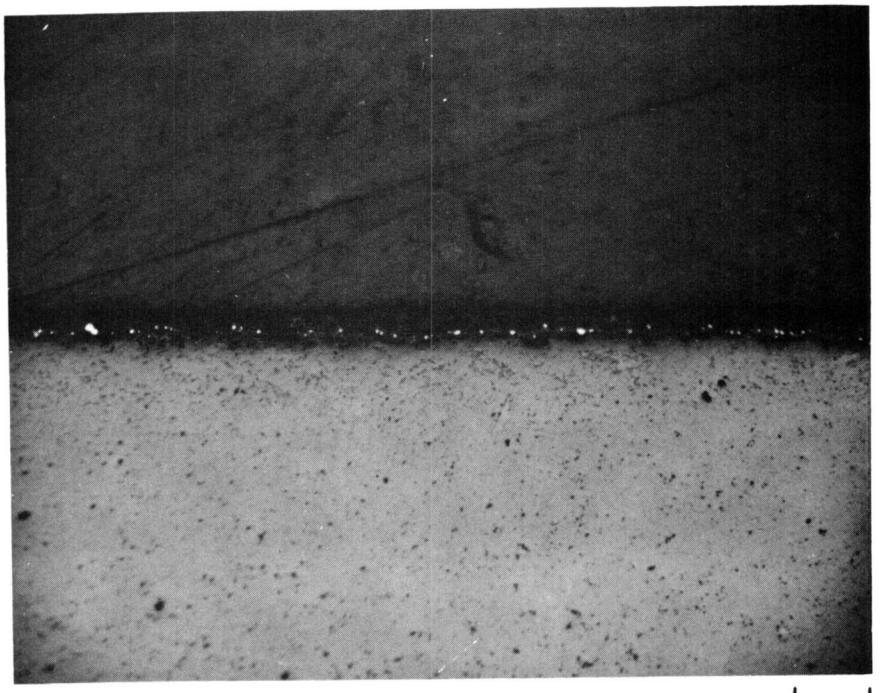

a) SAMPLE 1105.1 OXIDIZED 96 HOURS AT 1400°C

50μ

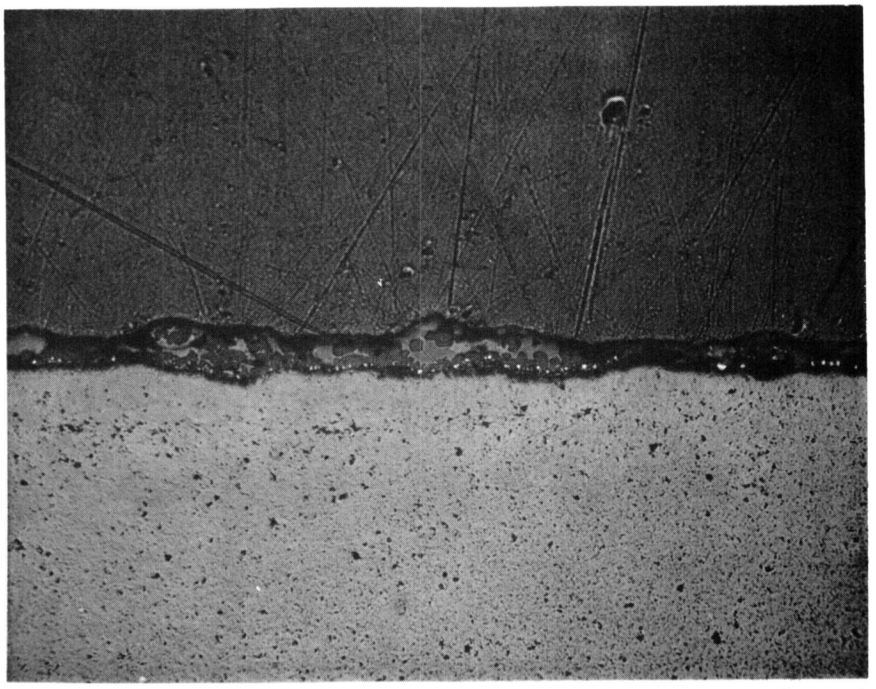

b) SAMPLE 1111.1 OXIDIZED 45 HOURS AT 1400°C

50μ

Figure 14 Oxide Scales on Samples 1105 and 1111.1

79–04–143–11

greater) which tend to form a dense matt of accicular crystallites. (For β'-X phase samples which exhibit the lowest oxidation rates, only mullite was detected in the scale by XRD.)

Hot pressed Si_3N_4 bodies containing Y_2O_3 as the sintering aid exhibit very low oxidation rates (Refs. 40, 46). The crystalline oxidation products are cristobalite and $Y_2Si_2O_7$ (Ref. 47). By way of analogy with the mullite forming bodies in the Y-Si-Al-O-N system, it could be anticipated that bodies in the same system with scales bearing on the order of 30 volume percent $Y_2Si_2O_7$ crystals would also exhibit oxidation rates on the order of 0.01 $mg^2cm^{-4}hr^{-1}$ at 1400°C. One can then inquire what cation equivalent percents would yield such a concentration of $Y_2Si_2O_7$ crystal, given the constraint that on the order of 1 e/o Al is necessary to permit pressureless sintering. Calculations shown that this would require an equivalent formulation of the oxide scale composition to be about $Y_{.182}Al_{.013}Si_{.854}O_2$. This would be the oxidation product, for instance, at a body that was about 71.5 percent $Si_{2.943}Al_{.057}O_{.057}N_{3.943}$ + 28.5 m/o $Y_2Si_2O_7$, or, for another instance, 71.6 m/o Si_3N_4 + 27.4 $Y_2Si_2O_7$ + 0.9 $Y_3Al_5O_{12}$. Such bodies would require about 33 w/o Y_2O_3 in their formulations. Bodies with such high yttrium concentrations were not investigated.

Returning to consideration of the mullite forming bodies, examination of the mechanical test data presented in Table 7 shows that samples of compositions with low 1400°C oxidation rate constants (compositions 1105 and 1115) nonetheless suffer significant degradation in room temperature flexural strength following 100 hrs exposure to air at 1370°C, although there was no degradation after similar exposure at 1300°C. Examination of the micrographs of the polished sections shown in Figs. 13 and 14 shows that the scale-body interface does not advance smoothly during 1400°C oxidation, but generates a rather pitted surface which is probably responsible for the loss in strength.

b. 1300°C Oxidation

The 1300°C parabolic oxidation rate constants for some Y-Si-Al-O-N samples are plotted vs composition in Fig. 15. At this temperature (which is below the minimum solidus temperature in the Y_2O_3-Al_2O_3-SiO_2 system) oxidation rates are acceptionally low (particularly for the samples which would have a substantial fraction of mullite in their scales) and as mentioned earlier, the samples tested showed no degradation in room temperature flexural strength after 100 hrs of air exposure.

c. 1000°C Oxidation

Most of the samples subjected to oxidation at 1000°C showed little or no weight gain or other evidence of sample degradation. The exception was

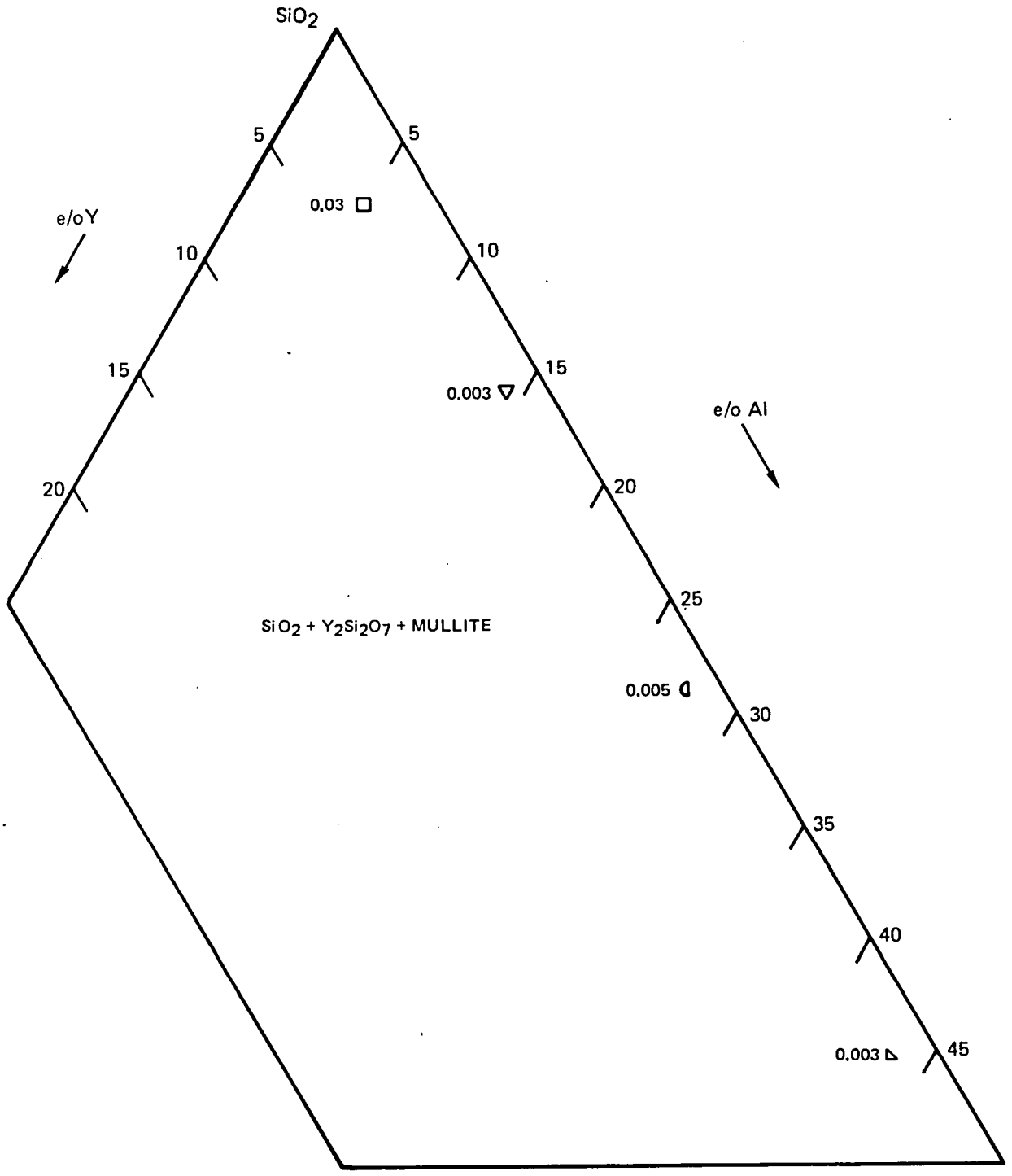

Figure 15 1300°C Oxidation Rate Constants ($mg^2\ cm^{-4}\ hr^{-1}$) for Samples in the Y–Si–Al–O–N Systems (Symbols Defined in Table 6)

79–04–137–12

composition 1078, lying in the four-phase field Si_3N_4-YAG-YS_2-H which oxidized nearly as fast at 1000°C as at 1400°C. (As shown earlier, this sample showed evidence of several sub-scale degradation during 1400°C oxidation.) Macro- and micro-graphs of the polished cross section of sample 1078.2 are presented in Fig. 16 which show the extent of the attack after 65 hrs at 1000°C. X-ray diffraction shows the surface region to consist of the X_I modification of Y_2SiO_5 and β'.

5. Mechanical Properties

The mean room temperature and 1370°C strength values, and 1370°C 69 MPA creep data for various samples recorded in Table 7 are plotted against composition, as discussed earlier, in Fig. 17. It can be seen that the general trend is for strength (measured both at 25°C and 1370°C) to decrease, and creep rate to increase, with increasing aluminum concentration. The progressively poorer elevated temperature mechanical properties correlated with the decrease in solidus temperature with increasing aluminum concentration mentioned earlier. While various types of recognizable flaws served to initiate fracture at 25°C, distinct flaws were generally not resolved on the fracture surfaces of samples tested at 1370°C, suggesting that the grain boundaries themselves were strength controlling at this temperature.

The β'-Y_2O_3 formulations (entires 1 through 4 of tables 6 and 7) were studied in some detail in Ref. 21. Flaws that were identified from SEM and microprobe analyses of the fracture surfaces of the samples included:

1) Metallic inclusions, exemplified by Fig. 18. These are silicon-transition metal particles resulting from the impurity-initiated decomposition Si_3N_4 during firing.

2) Small irregular voids, exemplified by Fig. 19. These may be the sites of inclusions that were ejected at fracture.

3) Large voids, probably resulting from the inclusion of foreign matter in the sample.

Fractures of composition 1105 also initiated irregular voids near the surface, exemplified in Fig. 20, or at edges, although at substantially lower stress levels than the β'-Y_2O_3 samples. Micrographs at HF etched and unetched polished surfaces of sample 1105.1, Fig. 21, show a coarse grain structure with a relatively high volume fraction at etched material, probably glass, in grain boundaries.

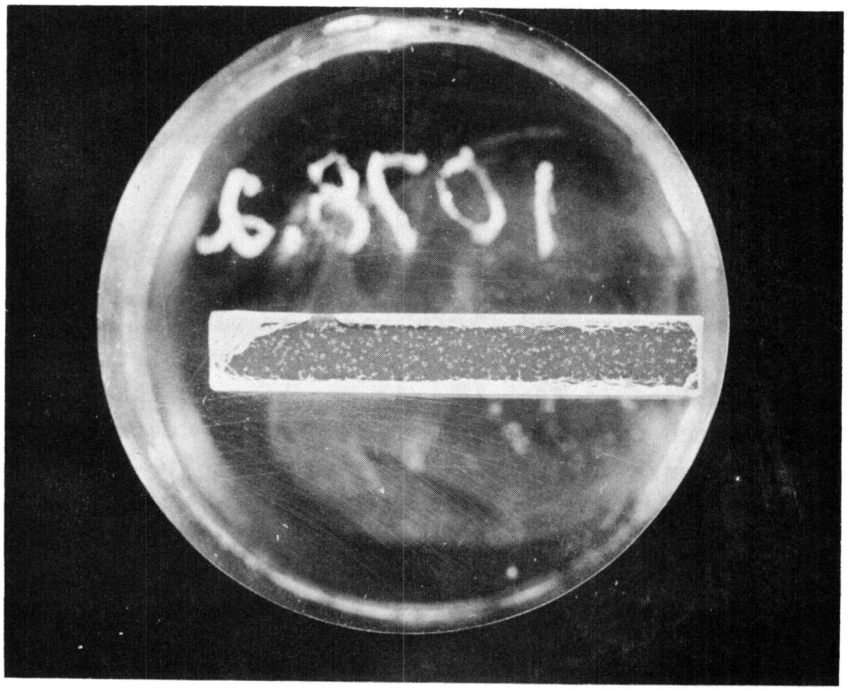

Figure 16 Polished Cross Section of Sample 1078.2 Oxidized at 1000°C for 65 Hours

79–04–137–13

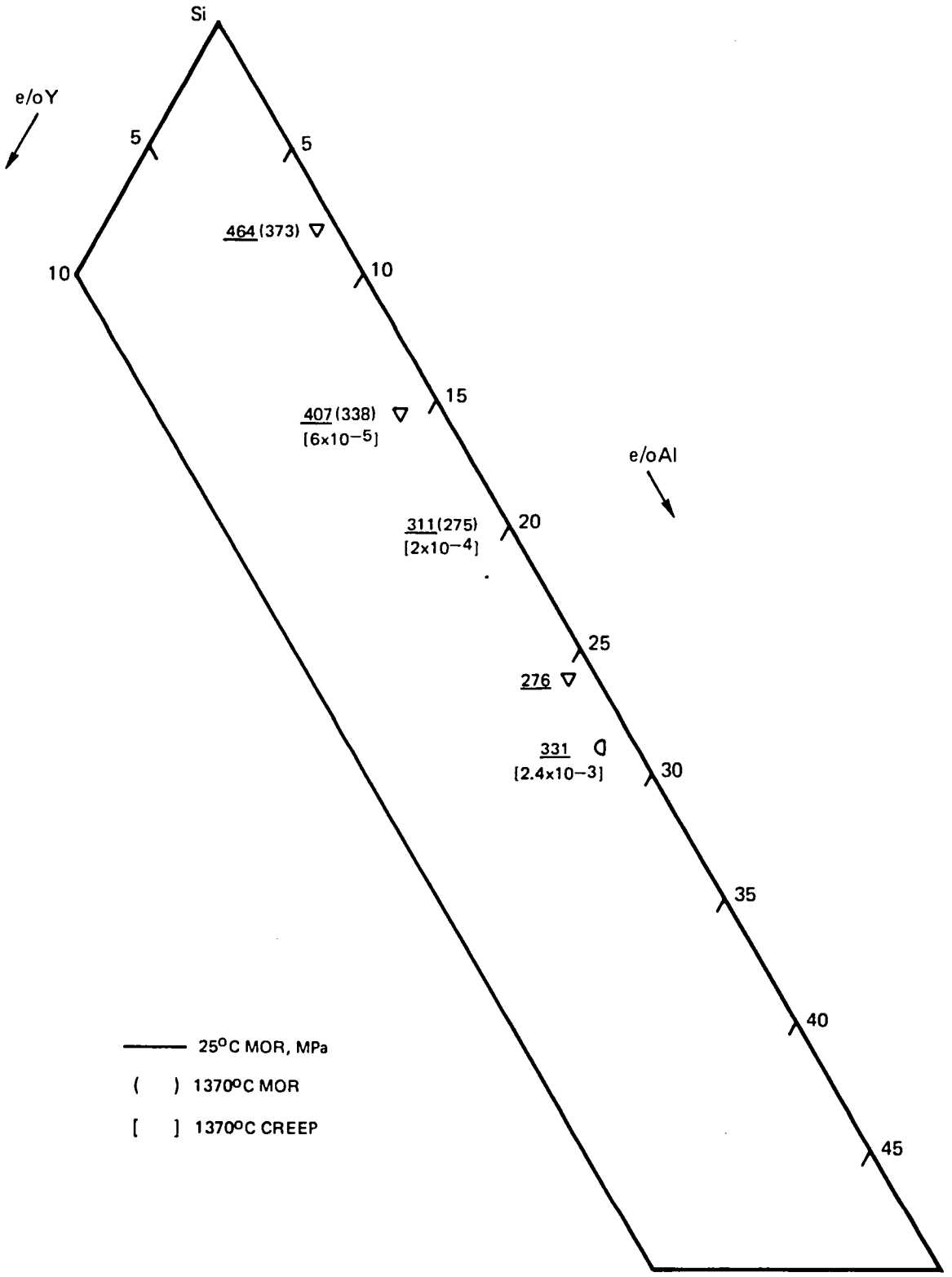

Figure 17 Mechanical Property Data vs. Composition for Some YSiALON Samples (Symbols Defined in Table 6)

79-04-137-5

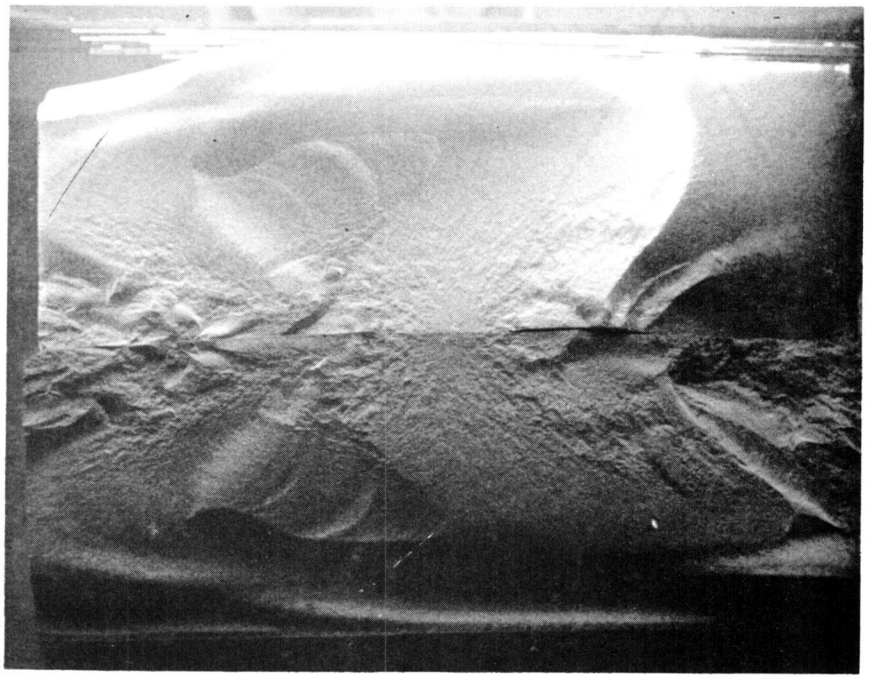

700μ

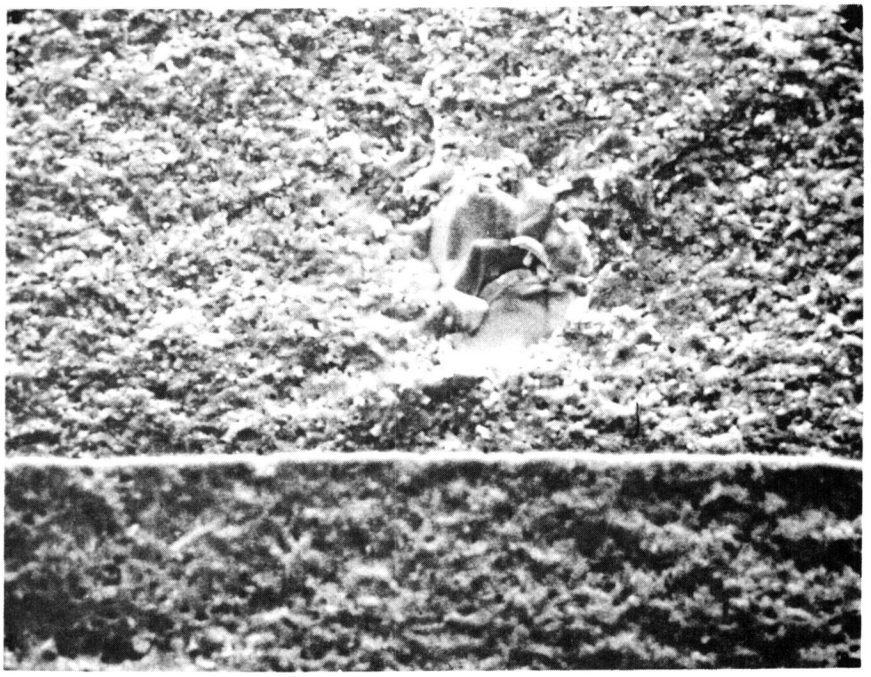

10μ

Figure 18 Fracture Initiated at Metallic Inclusion in β'1 + 2.5 w/o Y_2O_3 Sample (σ = 386 MPa)

79–04–137–16

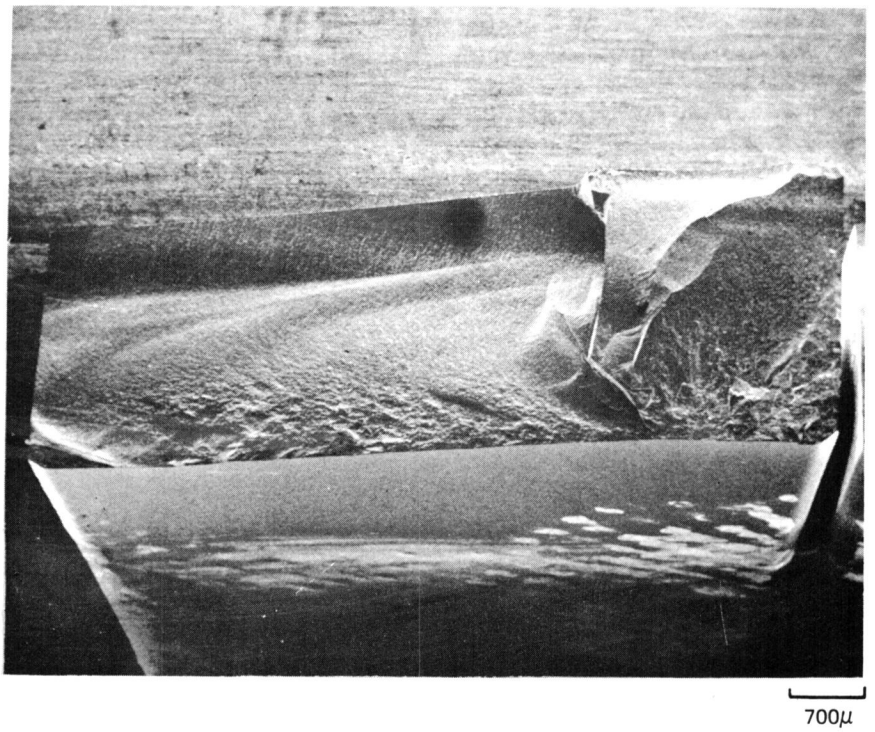

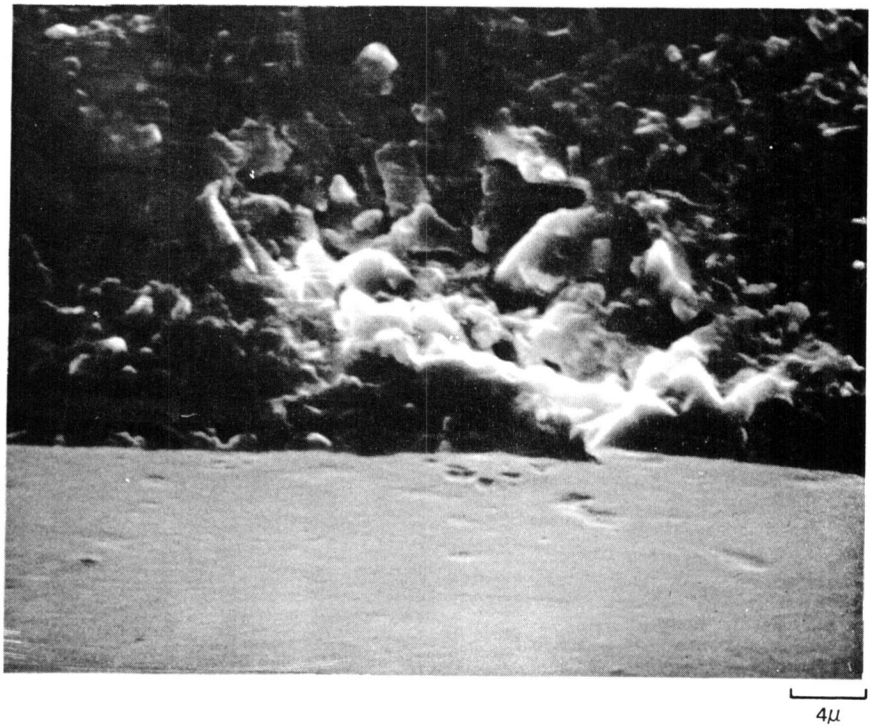

Figure 19 Fracture Initiated at Subsurface Void in $\beta'2 + 5$ w/o Y_2O_3 Sample (σ = 510 MPa)

77–05–35–2

A. OVERALL

700μ

B. INITIATION SITE

10μ

Figure 20 Sample 1105.10 Fracture Surface
(σ = 341 MPa)

78–09–161–5

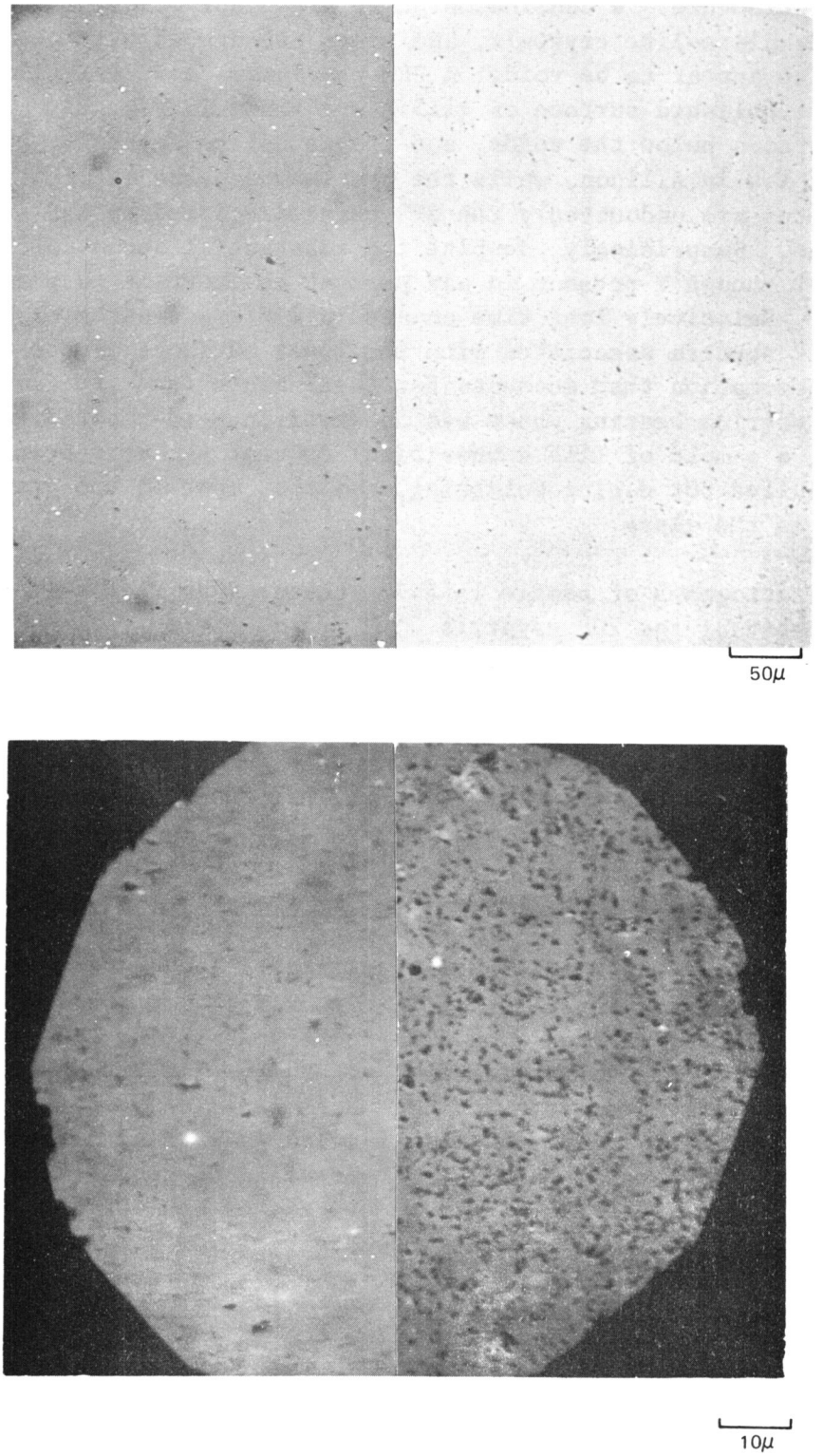

Figure 21 Unetched and HF Etched Polished Sections of Sample **1105.1**

The samples with the lowest strength - those of composition 1115 - exhibited a particularly coarse grained microstructure shown in Fig. 22. This shows a three-phase structure: a continuous phase presumably consisting of β' crystals discontinuous plate-like crystals, and areas associated with the plate-like crystals which appear to be void. A SEM photograph and EDAX silicon and aluminum maps from the polished surface of 1115.2 are shown in Fig. 23. It can be seen that the surfaces below the voids, and the lath-like crystals, are high in aluminum and low in silicon, while the continuous phase is rich in both Al and Si. The plates are undoubtedly the $2H^{\delta}$ phase disclosed by XRD to be present in the sample. Surprisingly, despite the substantial amount of Y in the sample, there was not enough Y present in any part of the surface to permit making an yttrium map. Relatively long time counts in different parts of the surface produced weak spectra associated with the lower surfaces of the void areas. A reasonable assumption that accounts for these facts (and the fact that no crystalline yttrium bearing phase was observed in powder obtained by crushing and grinding a sample of 1115 composition) is that the void areas contained glass that pulled out during polishing, and that most of the yttrium in the samples was present in the glass.

A SEM fractograph of sample 1115.2, presented as Fig. 24 more clearly shows plate-like habit of the $2H^{\delta}$ crystals.

From the above observations it may be concluded that the lower room temperature strength of the high aluminum samples is also related, albeit indirectly, to the lower solidius temperature and higher liquid concentration at sintering temperature in this part of the system, which leads to coarsening of the microstructures.

6. Summary of Properties of Y-Si-Al-O-N Samples

Five 3-phase compatibility tetrahedra and 11 4-phase tetrahedra exist in the quinery system wherein one phase is either Si_3N_4 or a $Si_{3-x}Al_xO_xN_{4-x}$ solid solution. Compositions from all of the 3-phase (or bounding 2-phase planes) and two of the 4-phase tetrahedra (Si_3N_4 - YAG-YS_2-H, and Si_3N_4 - YAG-$2H^{\delta}$-M) where screened for oxidation and mechanical properties. The only sinterable bodies with low parabolic oxidation rate constants at 1400°C (on the order of 0.01 $mg^2cm^{-4}hr^{-1}$) were compositions whose oxides fell in the primary phase field of mullite and produced scales at 1400°C that were about 30 volume percent or more mullite. Unfortunately, these compositions fall in regions of the quinery system where the solidus temperature is low (perhaps below 1500°C) so that 1370°C mechanical properties are poor. No sinterable composition was found that exhibited oxidation and mechanical properties that would be acceptable for high stress applications in oxidizing atmospheres at 1370°C (2500°F). However, bodies were produced which exhibit properties

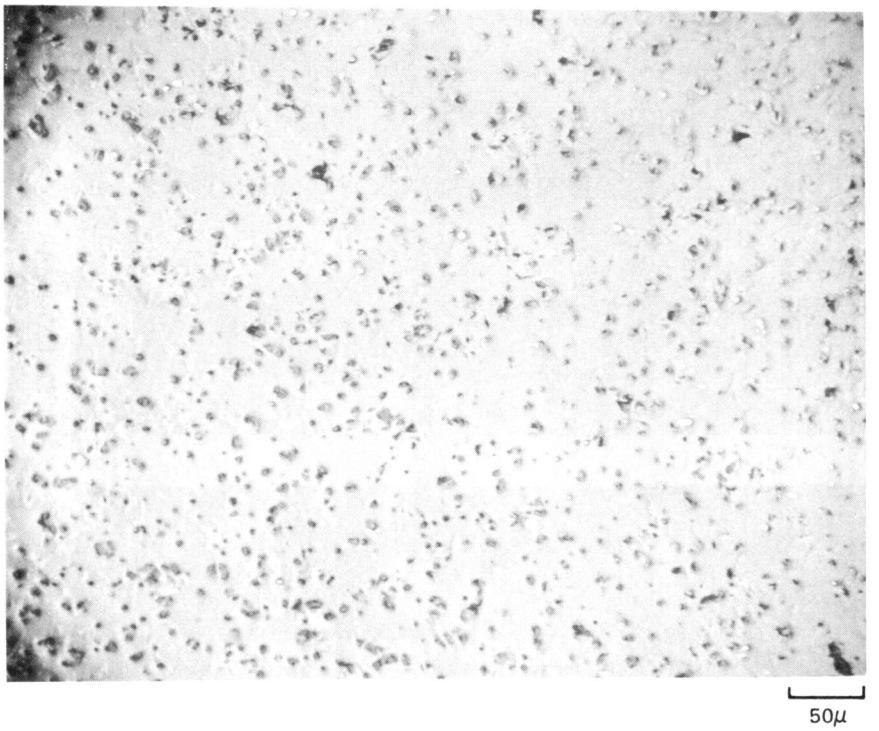

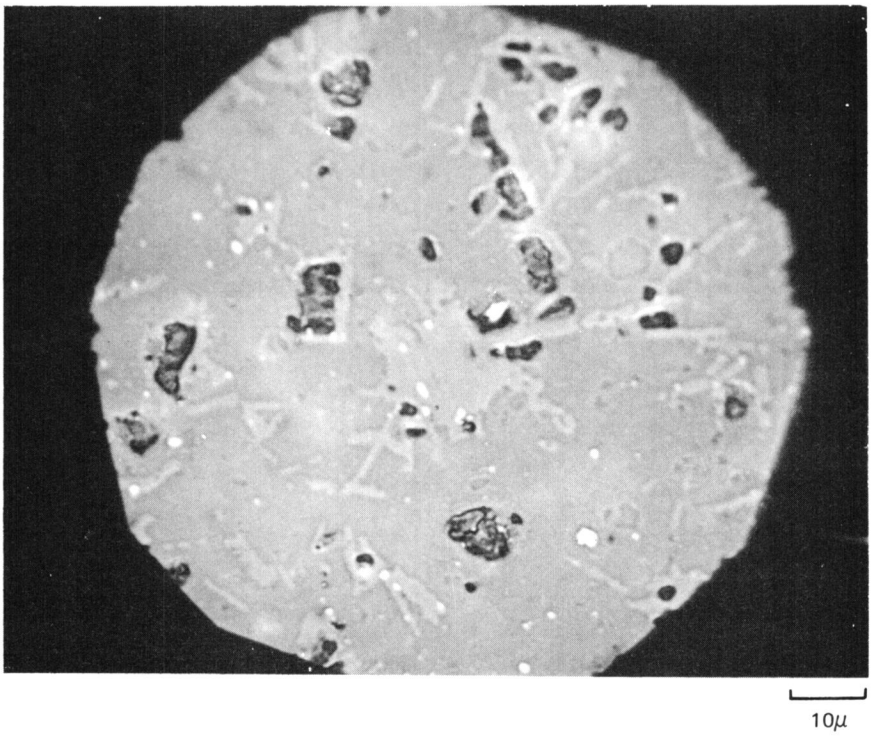

Figure 22 Relief Polished Section of Sample 1115.2

78–09–136–5

A. SEM

B. ALUMINUM MAP

C. SILICON MAP

Figure 23 SEM and EDAX Element Maps of Sample of Composition 1115

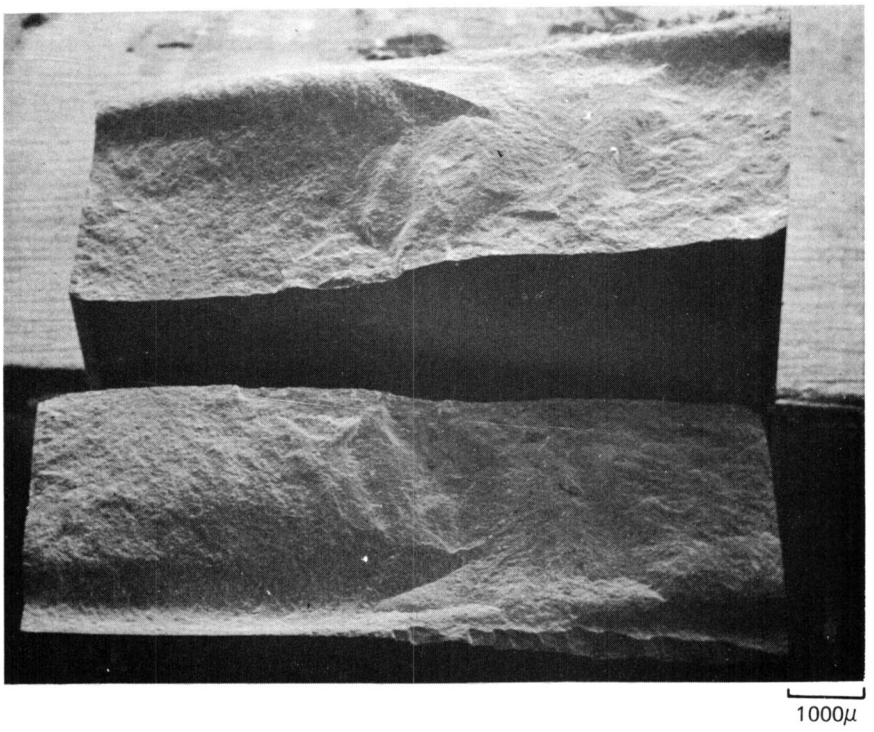

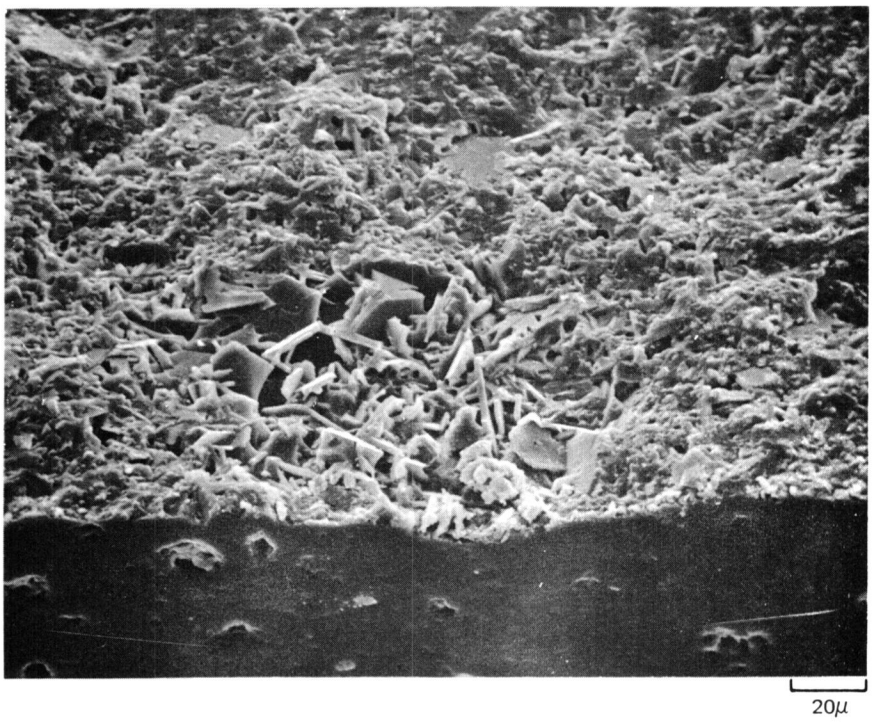

Figure 24 Fracture Surface of Sample 1115.3
(σ = 327 MPa)

79–04–137–14

attractive for stressed application at temperature of 1300°C and below. One formulation, (96.6 m/o $Si_{2.614}Al_{.386}O_{.386}N_{3.614}$ + 2.3 m/o $Y_3Al_5O_{12}$ + 1.0 m/o $Si_3Al_6N_{10}$) and process, produced samples which exhibited the following properties:

Property	Value
1300°C oxidation rate	0.003 $mg^2cm^{-4}hr^{-1}$
25°C MOR (mean)	518 MPa
1370°C MOR (mean)	340 MPa
1370°C, 69 MPa creep	$6 \times 10^{-5}hr^{-1}$

D. System Y-Si-Be-O-N

1. Background

a) System $BeO-Y_2O_3-SiO_2$

Prior work on some binary subsystems includes that or Morgan and Hummel on the $BeO-SiO_2$ system (Ref. 48), Bondar and Galakov on the $Y_2O_3-SiO_2$ system (Ref. 38), Olds and Otto (Ref. 49), and Bartran (Ref. 50) on the system $BeO-Y_2O_3$. Olds and Otto show no compounds between BeO and Y_2O_3, but indicate extensive solution of BeO in Y_2O_3 about 1000°C. Bartram presented a tentative phase diagram which showed three incongruently melting compounds with molor ratios $BeO:Y_2O_3$ of 1:1, 4:1* and 9:1, and indicated the possibility of metastability. Other investigators (Refs. 51, 52 and 53) had prepared the 1:1 compound from the melt, but could not prepare it in the solid state. Harris and Yakel (Ref. 53) determined its crystal structure and speculated that the atomic environment was more nearly representative of liquids than of equilibrium solids. They reported that the compound tended to dissociate into the component oxides when heated (to unspecified temperature).

The only reference located on work in the ternary system is that of Bartram (Ref. 54) who discovered single crystals, later determined to be of composition $Y_2Si_2Be_2O_7$, growing on the surfaces of $BeO-Y_2O_3$ samples fired in a furnace insulated with silica brick. He later heated a pellet of this composition prepared from the component oxides in air of 1350°C and found it to consist of $Y_2SiBe_2O_7$ along the traces of Y_2O_3, Y_2BeO_4 and cristobalite. Bartram determined the structure of $Y_2SiBe_2O_7$, and showed it ot isomorphous with minerals of the melilite family.

*Latter shown to be Y_2SiBeO_7 (Bartram, personal communication).

b) The system Si_3N_4-SiO_2- Y_2O_3-YN

This was discussed in Section IV.B.1.e.

c) The system BeO-SiO_2 - Si_3N_4 - B_3N_2

This system was investigated by Huseby et al, (Ref. 55). His diagram is reproduced as Fig. 25.

2. Experimental Investigation

a) System BeO-Y_2O_3-SiO_2

Given the demonstrated existence of the melilite phase, it was questioned whether other silicate or aluminate analogs exist in this system which could constitute possible fully oxidized matrix phases for Si_3N_4 bodies. Compositions prepared, heat treatments given, and phases observed by XRD are presented in Table 10. Note that the compositions numbers 1, 2, 3 and 4 correspond to possible isomorphs to the melilite, α wollastonite, apatite, and YAM phases respectively, which also have nitrogen substituted analogs in the Si_3N_4 - SiO_2 - Y_2O_3 system (Ref. 20). Pellets fired at 1400°C exhibited little shrinkage, (less than 5 percent) or other evidence of liquid formation.

The only ternary phase that was positively identified was the melilite phase $Y_2Be_2SiO_7$ previously reported by Bartram. Our XRD data for this phase are compared with those of Bartram in Table 11. The pattern of another phase was also observed in a number of the samples. The XRD data for this phase are presented in Table 12 and are compared with the data of Lange for the YAM isomorph $Y_4Si_2O_7N_2$ (J phase) and that of Bartram for Y_2BeO_4.

The observed x-ray diffraction pattern is seen to bear a close resemblance to both the J and Y_2BeO_4 phases. Since all mixtures containing the new phase were multiphase, it is not certain that the diffraction data presented are complete or accurate because of possible overlap with peaks from other phases. Although at first reading the data for the new phase appear more closely to approximate that of J phase, if one eliminates the peaks attributed to $Y_2Be_2SiO_7$ from the pattern it is seen to be very similar to the Y_2BeO_4 pattern, although with a somewhat expanded lattice which could be anticipated if some solubility toward Y_2SiO_5 existed. More significant perhaps, is the fact that the ambiguous 4-phase data for compositions 5, 7, and 11 can be readily interpreted in

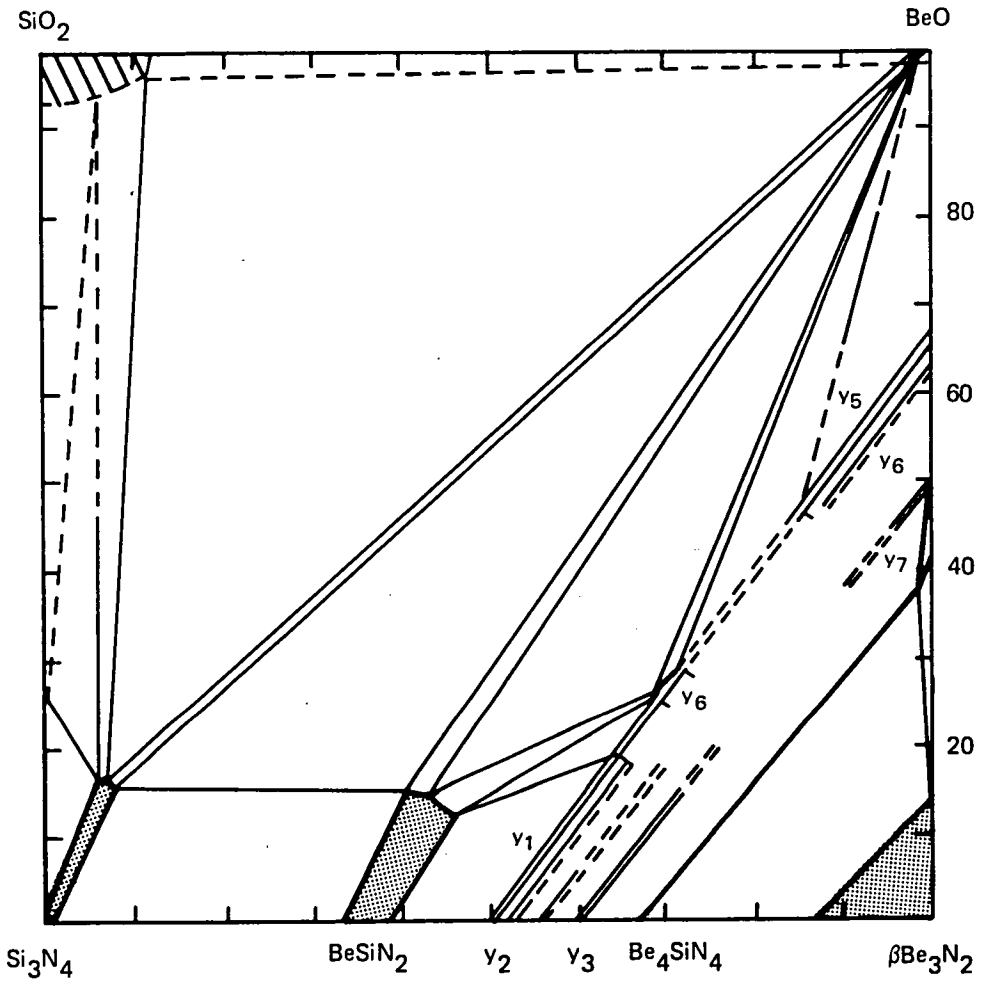

Figure 25 System Si_3N_4–SiO_2–Be_3N_2–BeO at 1760°C, After Huseby et. al. (ref. 53)

79–04–137–21

Table 10

Phase Observed After Heat Treatment of Compositions in the System $BeO-Y_2O_3-SiO_2$

Comp. Number	BeO	Y_2O_3	SiO_2	Heat Treatment*	Phases observed by x-ray diffraction						
					BeO	Y_2O_3	SiO_2	Y_2SiO_5	$Y_2Si_2O_7$	$Y_2B_2SiO_7$	Y_2BeO_4
1	50.0	25	25	A					m	s	
2	33.3	33.3	33.3	A				m	w	s	
3	9	45.5	45.5	A				s		m	
4	25	50	25	A		s		m			s
5	33.3	50	16.7	A		s		w		m	s
6	40	20	40	A			m			s	
7	65	25	10	A	w	m				m	s
7a	65	25	10	B	w	m				s	s
7b	65	25	10	C	w	s				s	s
8	70	7.5	22.5	A	w		m			s	
9	50	10	40	A	w		m			s	
10	33.3	33.3	33.3	A		w				s	w
10a	33.3	33.3	33.3	B				s	m	s	w
11	25	50	25	A		s		m		m	s
11a	25	50	25	B		s		m		m	s
11b	25	50	25	C		s		m		m	s

*A; heated for 60 hours at 1400°C

B; heat treatment A samples crushed to powder recompacted and heated an additional 45 hours at 1200°C.

C; heat treatment B samples crushed to powder recompacted and heated an additional 100 hours at 1000°C.

TABLE 11

X-RAY DIFFRACTION PATTERNS FOR Y_2Be_2SiO7

This work		Bartram[1]		
dA	I/I_1	dA	I/I_1	hkl
5.12	2	5.19	25	110
4.74	17	4.80	35	001
3.63	2	3.67	8	200
3.48	20	3.51	16	111
3.25	20	3.28	100	210
2.88	30	2.906	35	201
2.69	100	2.702	95	211
2.567	5	2.590	18	220
2.376	5	2.391	16	002
2.301	13	2.315	50	310
2.261	8	2.276	35	221
2.159	8	2.172	12	301
2.071	13	2.083	30	311
2.016	2	2.029	8	320
1.989	3	2.000	< 5	202
1.919	30	1.929	25	212
1.819	7	1.829	8	400
1.765	11	1.774	20	410
1.748	1	1.757	< 5	222
1.715	11	1.725	60	330
1.700	9	1.707	35	302
1.653	28	1.662	25	312
1.627	5	1.627	18	420
1.614	15	1.621	35	331
1.585	3	1.592	14	003
1.424	11	1.431	10	510
1.391	4	1.396	4	332
1.364	1	1.371	6	511
1.350	3	1.357	18	223, 422
1.300	10	1.307	16	313

(1) ASTM powder data file #22-110

TABLE 12

COMPARISON OF X-RAY DIFFRACTION DATA OF
SOME Y-Si-Be-O-N PHASES

$Y_4Si_2O_7N_2$ (1)		Observed Pattern		Y_2BeO_4 (2)		
d	I/Io	d	I/Io	d	I	hkl
7.3	15	7.4	10	7.21	14	101
				5.22	12	200
				4.621	7	201
4.57	15	4.53	23	4.484	71	102
4.35	10	(4.33)	*			
3.22	20	3.20	27	3.152	24	103
3.07	100	3.00	100	2.927	100	210
2.93	15	(2.90)	*			
2.87	33	2.87	30	2.844	36	302
				2.807	16	211
2.84	50	2.85	60	2.791	36	203
		2.82	50	2.776	34	112
		2.58	10	2.605	10	400
2.53	15	2.53	23(b)	2.477	6	004
2.51	10			2.411	10	013,311
2.27	10	2.26	7	2.237	9	204
				2.219	15	312
2.05	10	2.01	20	2.095	14	410
				1.980	17	313

(1) After Lange
(2) After Bartram
* $Y_2Be_2SiO_7$ line

terms of high and low temperature compatibility relationships involving the Y_2BeO_4 phase, which has already been demonstrated to be unstable at low temperatures (Ref. 51). It is less straight-forward to interpret the data if one assigns the new diffraction pattern to a YAM phase having the composition Y_4BeSiO_7. In light of these observations, tentative phase relations for the system are suggested to be as shown in Fig. 26. The lower temperature of stability of the Y_2BeO_4 phase is not specified.

b) The Quinary Systems

Composition, fabrication, and test data for Y-Si-Be-O-N samples are found distributed in Appendicies B, C, and D. Compositions, recalculated from Appendix B in terms of equivalent percent Be, Y, and O, and phase compositions calculated on the basis of the XRD data, are presented in Table 13. Compatibility relations inferred from the data of Table 13, in conjunction with the already established phase diagrams for the Si_3N_4-Be_3N_2- BeO-SiO_2 and Si_3N_4-SiO_2-Y_2O_3 systems, permit the establishment of several of the compatibility tetrahedra in the quinery system. These are displayed in the model photographed in Fig. 27. These compatibility tetrahedra are listed in Table 14.

3. Properties of Test Samples

a) Oxidation

Oxidation data for Y-Si-Be-O-N bodies are plotted as functions of compositions using the previously described techniques in Fig. 28. These oxidation rate data may be compared with those in the analogous region of Y-Al-Si diagram, Fig. 12. (Note the difference in scale between Figs. 12 and 28). Oxidation rates in the Be system are seen to be an order of magnitude lower than in the Al system. The absence of liquid in the oxide scales of the Be samples is undoubtedly an important factor in the lower rates. Note that sample 1126 (point falling in the SiO_2 + $Y_2Si_2O_7$ + $Y_2Be_2SiO_7$ field) meets the program goals as far as oxidation rate is concerned.

b) Mechanical Properties

Mechanical properties were measured for samples of composition 1126. The mean room temperature MOR was 434 MPa (63 ksi). The creep sample exhibits a high creep rate of 5.7×10^{-3} hr^{-1} at 1370°C and 69 MPa stress, and failed after eight hours. A second creep sample was heated in air at 1370°C for 200 hours prior to testing. This sample failed minutes after the 69 MPa load was applied.

c) Summary of Y-Si-Be-O-N Data

Only a small number of samples in the Y-Si-Be-O-N system have been investigated, and large regions of the system remain to be explored. Samples of composition 0.5 e/o Be, 3.0 e/o Y and 4.4 e/o O exhibited a low oxidation rate, but a high creep rate at 1370°C make this composition unacceptable for high stress applications.

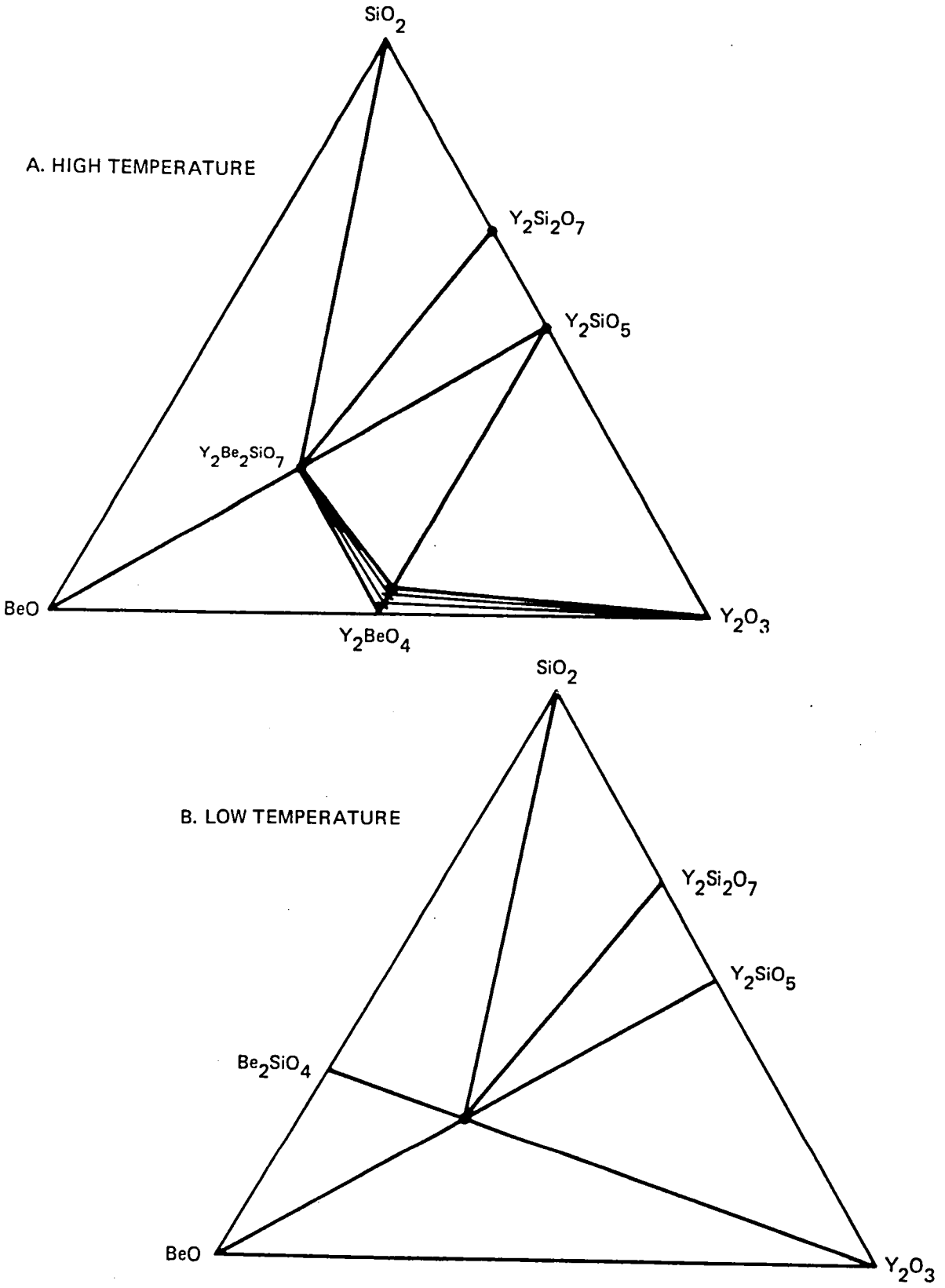

Figure 26 Solid Phase Compatibility Relations in the BeO–Y_2O_3–SiO_2 System

79–04–137–22

TABLE 13

PHASE COMPOSITIONS OF SAMPLES IN THE Y-Si-Be-O-N SYSTEM

Composition Designation (Appendix B)	Equivalent Percent Be	Y	O	XRD Observations	Symbol	Calculated Equilibrium Phase Composition: $\beta Si_{3-x}Be_xO_{2x}N_{4-2x}$ m/o	x	$Y_2Si_{3-y}Be_yO_{3+2y}N_{4-2y}$ m/o	y	Other m/o	Phase
1083	4.7	7.3	16.7	sβ + wM(1)	o	85.0	0	15.0	1.9	0.0	
1084	5.9	1.2	13.0	sβ	•	97.8	0.303	2.2	2.0	0.0	
1113	1.7	2.4	5.8	sβ + wM	o	95.0	0	5.0	2.0	0.0	
1117	1.5	2.9	9.5	sβ + w YS_2	Δ	94.1	0.095	0.0		5.9	$Y_2Si_2O_7$
1126	0.5	3.0	4.4			95.0	0	4.3	0.69	0.7	$Y_5Si_3O_{12}N$
Si_3N_4-$Y_2Be_2SiO_7$	15.4	23.1	53.8	sβ + s M	o	50	0	50	2.0	0.0	
Si_3N_4-"Y_4BeSiO_9"	6.7	40	60	s M + w 2.86 Å (H Phase?)	o			86.7	0.692	13.7	$Y_5Si_3O_{12}N$

(L) M = melilite phase, $Y_2Si_{3-y}Be_yO_{3+2y}N_{4-2y}$

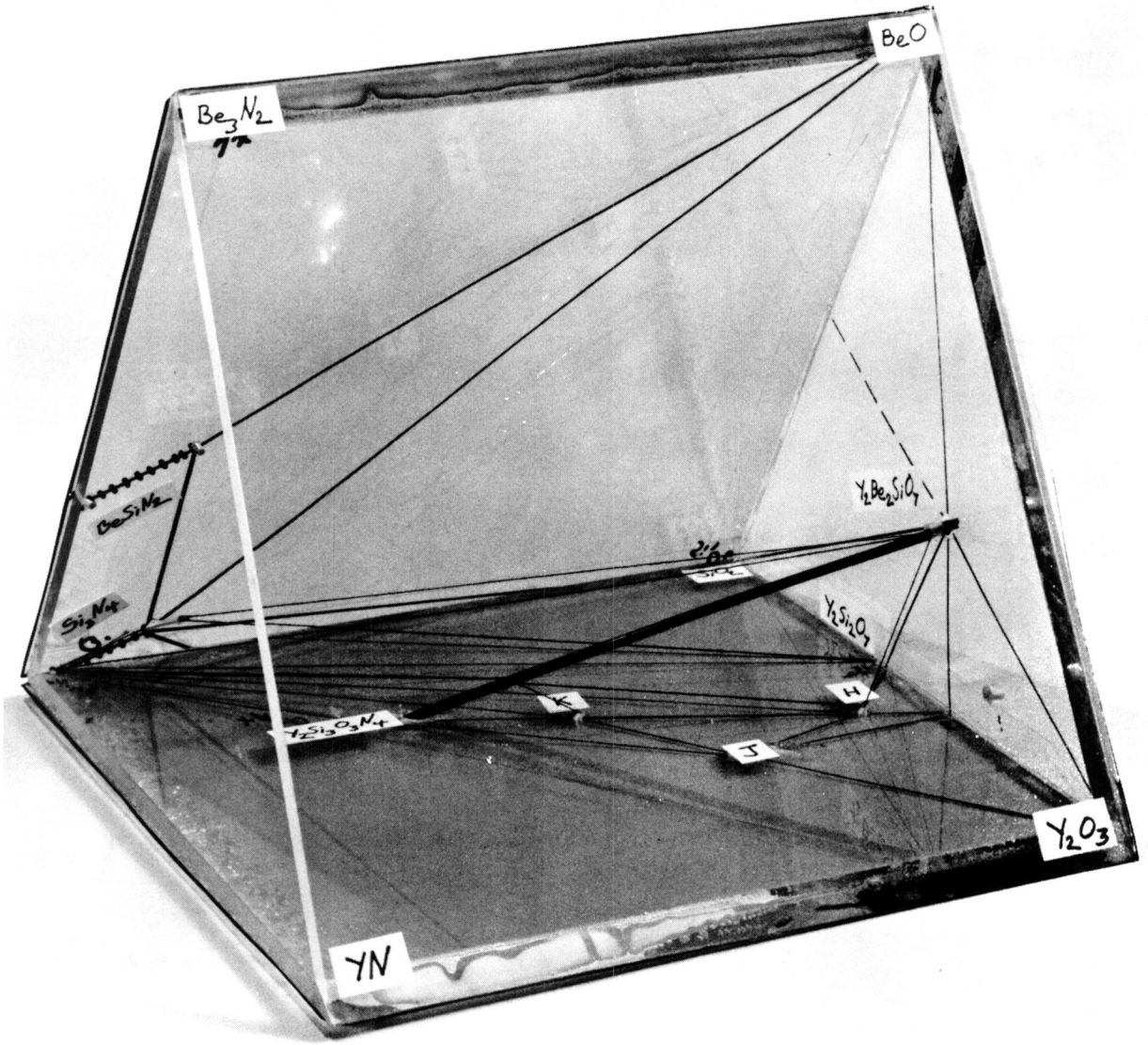

Figure 27 Model of the Y-Si-Be-O-N System

TABLE 14

PARTIAL LIST OF COMPATIBILITY TETRAHEDRA
IN THE Y-Si-Be-O-N SYSTEM

	3 Phase	4 Phase
1)	β_o^* - $M^{**}_{0 \leq y \leq .7}$ -K	
2)		β_o - $M_{y=.7}$ -K - H
3)	β_o - $M_{.7 \leq y \leq 2}$ -H	
4)		β_o - $M_{y=2}$ -H - YS_2
5)	$\beta_{o \leq x \leq .8}$ -$M_{y=2}$ - YS_2	
6)	$\beta_{o \leq x \leq .8}$ -Si_2N_2O - YS_2	
7)		$\beta_{x=.8}$ - Si_2N_2O - YS_2 - SiO_2
8)		$\beta_{x=.8}$ - YS_2 - SiO_2 - $M_{y=2}$
9)		$\beta_{x=.8}$ - SiO_2 - $M_{y=2}$ - BeO

* $\beta = Si_{3-x}Be_xO_{2x}N_{4-2x}$

** $M = Y_2Si_{3-y}Be_yO_{3+2y}N_{4-2y}$ (melilite ss)

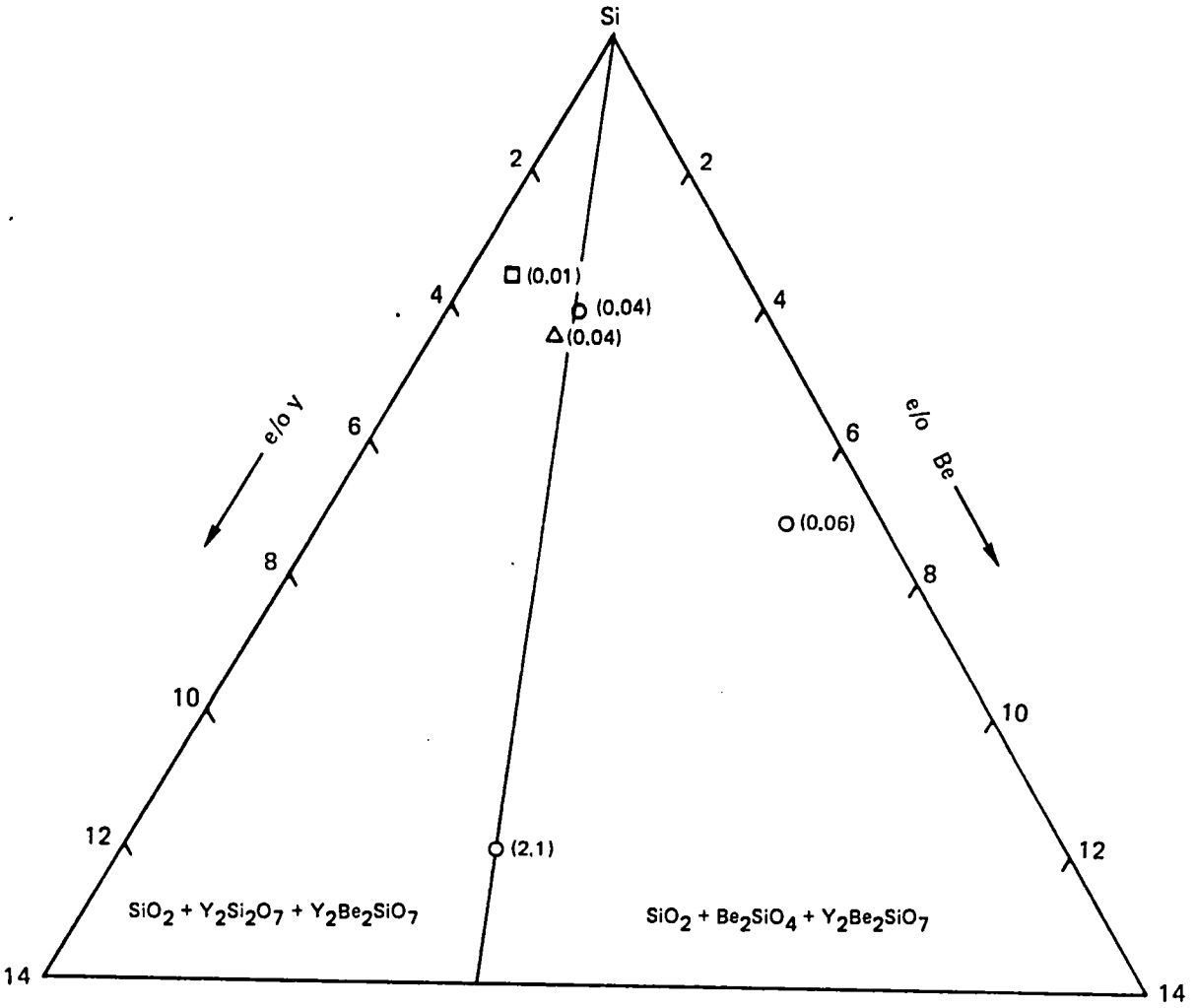

Figure 28 Oxidation Rate Constants ($mg^2\ cm^{-4}\ hr^{-1}$) vs. Composition for Y–Si–Be–O–N Sample

79–04–137–23

E. R-Si-O-N Systems

1. The System Si_3N_4-SiO_2-Y_2O_3

The solid phase compatibility relationships based on the experimental work of Rae et al. (20) Wills et al. (39) and Lange et al. (40) were presented in Fig. 6. In the course of the present work some liquid-solid equilibria data were obtained, as these are relevant to the sintering of Si_3N_4 using Y_2O_3 as the sintering aid. These data are presented in Appendix E, and are interpreted in terms of the phase diagram for the join Y_2SiO_5-$Y_2Si_3O_3N_4$ in Fig. 29. Note that all compositions from about 10 m/o to 50 m/o $Y_2Si_3O_3N_4$ are liquid at 1750°C. Compositions along the join cooled from above the solidus retain some glass at room temperature, as seen in Figs. 4 through 8 of Appendix E.

Understanding of the solid-liquid-phase relationships along the Y_2SiO_3-$Y_2Si_3O_3N_4$ join helps to resolve some of the conflicts in the published phase diagrams for the system Si_3N_4-SiO_2-Y_2O_3 (Ref. 20, 39, 40). Firstly, the failure of Wills et al. (Ref. 39) to find the compound $YSiO_2N$ (K phase) is understandable in terms of the incongruencey of K phase and tendency of the liquids to glass formation.

The composition of H phase was given as $Y_{10}Si_2O_{23}N_4$ by Lange et al. (Ref. 40) and as $Y_5Si_3O_{12}N$, by Wills et al. and initially by Jack (Ref. 56) who noted the similarity of the diffraction pattern of H phase to that of $Y_4Ca(SiO_4)_3O$ which has the apatite structure. Later work by Jack's group (Ref. 20) has assigned the homogeniety range of the H phase to a region near the composition (Y_4Si) $(Si_3O_{11}N)N$, or $Y_4Si_4O_{11}N_2$. Regarding the composition of H phase, our work confirms the assignment of Wills et al., and the earlier assignment of Jack, and shows essentially single phase material at the composition $Y_5Si_3O_{12}N$. This does not of course rule out the possibility that solid solutions occur between the latter composition and the $Y_4Si_4O_{11}N_2$ composition. As is shown by Fig. 6 of Appendix E, compositions richer in the component $Y_2Si_3O_3N_4$ than H phase can cool from temperatures above 1700°C to H phase plus glass. On the basis of x-ray data only such compositions would be assumed to be H phase.

2. The System Si_3N_4-SiO_2-Nd_2O_3

It was assumed that phases isomorphous to those in the Si_3N_4-SiO_2-Y_2O_3 system would form in this system, and that analogous liquid-solid relationships would also exist. The generally lower liquidus temperatures in the Nd_2O_3-SiO_2 system compared to those in the Y_2O_3-SiO_2 system suggested that ternary liquids in the Nd_2O_3-SiO_2-Si_3N_4 (or liquids involving mixtures of Nd_2O_3 and Y_2O_3) would be more reactive than the analogous Y_2O_3 liquids. Two compositions along the $Nd_2Si_2O_7$-$Nd_2Si_3O_3N_4$ join were investigated, namely

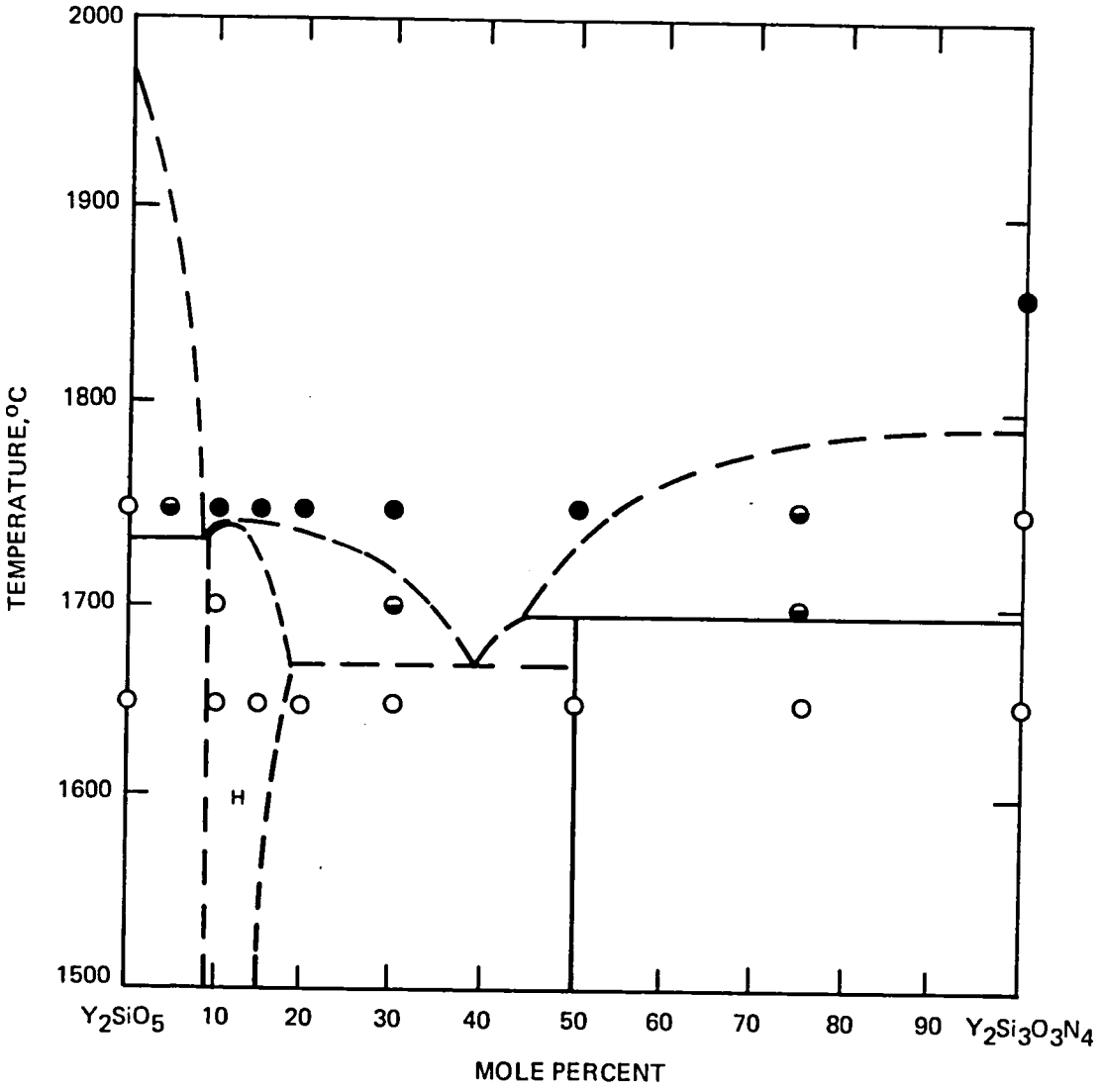

Figure 29 Phase Diagram for the System $Y_2SiO_5 - Y_2Si_3O_3N_4$

79-04-137-26

20 and 50 m/o $Nd_2Si_3O_3N_4$. Data for these compositions is included in Appendix E. Both the H and K phases were found to occur in the system, and their XRD data are included in Appendix E.

As was the case with compositions in the yttria system, so in the neodymia system large areas of matrix liquid failed to crystallize on cooling from 1750°C, and remained as glass at room temperature. Composition $NdSiO_2N$ cooled from 1750 and 1800°C contained no primary crystals, but exhibited dendritic structures. The x-ray pattern showed poorly crystallized H phase and $Nd_2Si_3O_3N_4$ which is probably, but not necessarily, indicative of incongruency of the K phase in this system also.

3. Reaction of Ternary Liquids with Si_3N_4

Samples consisting of different ratios of KBI Si_3N_4 and various ternary mixtures that are known from the above studies to be liquid at 1750°C were pelletized, and fired at 1750°C for 1 hour. These were then tested for apparent porosity, specific gravity, and bulk density according to the ASTM C373-5 water immersion test. A portion of each pellet was crushed for x-ray analysis and a portion used for metallographic examination. Results are presented in Table 15. Metallographs of sections of samples 1054 and 1055 are shown in Fig. 30.

It can be seen that in all cases of 50 w/o mixtures, the bodies fired to high density. Metallography indicates that microstructures consisted of a high volume percent matrix (largely H phase) and discontinuous Si_3N_4 crystals. The 25 percent mixtures however were all quite porous (about 25 percent) although a substantial amount of liquid was present at the firing temperature. This suggested that the liquids do not wet-out the solid phase effectively.

4. Sintering and Property Data for some R-Si-O-N Bodies

Composition, fabrication, and property data for some R-Si-O-N bodies, abstracted from appendices B, C, and D are presented in Table 16. Note that compositions prepared using the amorphous Si_3N_4(SN402) in general sintered to higher density than did compositions prepared with the KBI powder. However, even using the SN402, a composition 94 m/o Si_3N_4 6 m/o $Y_2Si_2O_7$ sintered to only about 80 percent of theoretical density, although SN402 mixed with 6 m/o $Ce_2Si_2O_7$, or $GdSmSi_2O_7$, sintered to near theoretical density. The latter bodies, although well sintered, exhibited very high oxidation rates that would prohibit their use in air of 1370°C.

TABLE 15

Reactions of Si_3N_4 with Y-Si-O-N and Nd-Si-O-N Liquids

Sample Number	Composition (W/O) Si_3N_4	Other	Apparent Porosity (%)	Bulk Density g/cc	Specific Gravity g/cc	β	Phases observed by XRD H	J	K	M
1050	50	50 $NdSiO_2N$	1.0	3.57	3.61	m	s			s
1051	75	25 $NdSiO_2N$	27	2.32	3.16	s			m	
1054	50	50 "$Y_{10}Si_7O_{23}N$	1.8	3.93	4.24	m	s			
1055	75	25 "$Y_{10}Si_7O_{23}N_4$"	26	2.35	3.18	s	m			
1057	50	50 "$Nd_{10}Si_7O_{23}N_4$"	2	4.41	4.53	w	s			
1058	75	25 "$Nd_{10}Si_7O_{23}N_4$"	20	2.63	3.29	m			s	

A. 50 w/o $Y_{10}Si_7O_{23}N_4$ (SAMPLE 1054)

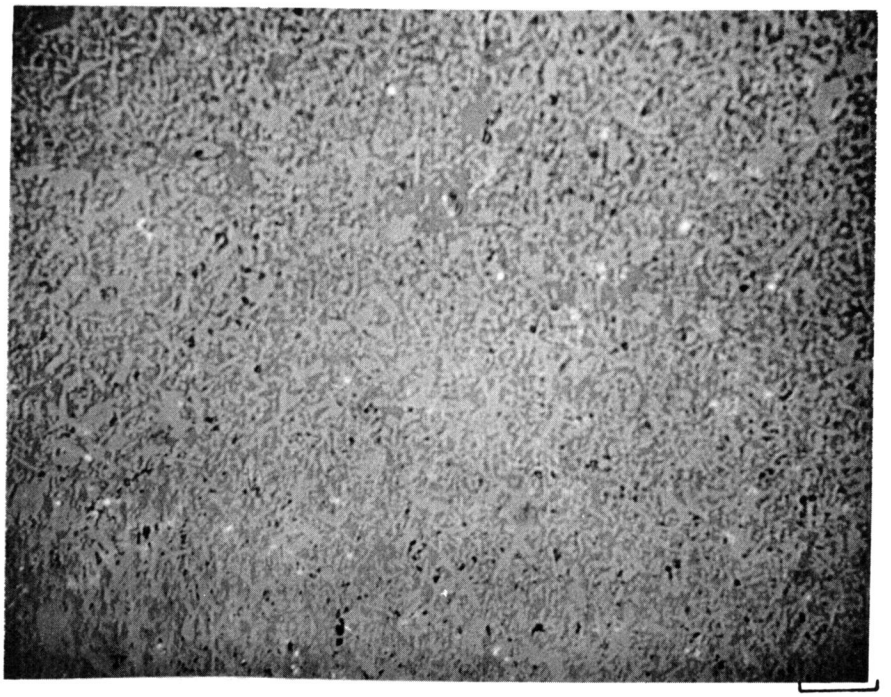

B. 25 w/o $Y_{10}Si_7O_{23}N_4$ (SAMPLE 1055)

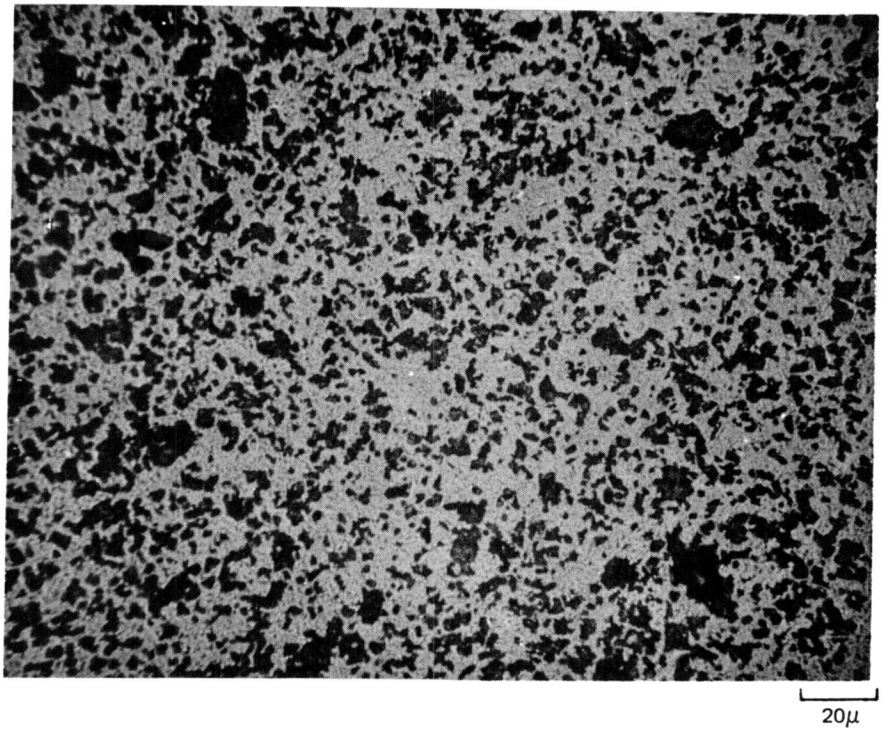

Figure 30 Etched Sections of Samples Containing Si_3N_4 and $Y_{10}Si_7O_{23}N_4$ in Different Proportions fired to 1750°C

77–12–44–5

TABLE 16

Fabrication and Property Data for Some R-Si -O-N Bodies

Sample Number	Calculated Phase Composition (m/o)			Firing Conditions		Apparent Porosity	Bulk Density	Specific Gravity	Oxidation Rate Constant ($mg^2 cm^{-4} hr^{-1}$)	
	Si_3N_4	$R_2Si_2O_7$	Si_2N_2O	Temp (^oC)	Time (hrs)	(%)	(g/cc)	(g/cc)	1370 °C	1400 °C
995	90 KBI	10 $Y_2Si_2O_7$	0	1720	1	35	2.18	3.40		
996	90 KBI	10 $Y_2Si_2O_7$	0	1760	1	37	2.37	3.40		
1116A	63 KBI 31 SN402	6 $Y_2Si_2O_7$	0	1760	2	29	2.32	3.25		
1116B	94 SN402	6 $Y_2Si_2O_7$	0	1760	2	14	2.64	3.08		
1119	94 SN402	6 $Ce_2Si_2O_7$	0	1760	2	0	3.44	3.44		0.3
1129	94 KBI	6 $Ce_2Si_2O_7$	0	1760	2	<1	3.44	3.44	0.75	
1130	94 Starck	6 $Ce_2 Si_2O_7$	0	1760	2	<1	3.05	3.05	0.50	
969	90 KBI	5.5 $Sm_2Si_2O_7$	4.5	1780	4	38	2.15	3.31		
1003	90 KBI	5.5 $(Gd,Sm,Nd)_2Si_2O_7$	4.5	1760	3	14	2.93	3.39		
1135	94 SN402	6 $(Gd,Sm)_2SiO_7$	0	1700	5	<1	3.29	3.29	1.6	
1136	94 SN402	6 $Nd_2Si_2O_7$	0	1700	5	<1	3.36	3.36	1.2	

5. Sintering and Property Data for the System Y-Ce-Si-O-N

a) Sample Formulation and Fabrication

The facts that Ce-Si-O-N bodies sinter to full density, but exhibit poor oxidation behavior, whereas Y-Si-O-N bodies do not sinter to high density, but hot pressed bodies of the nonsinterable compositions can exhibit outstanding properties, lead to the speculation that bodies in the combined Y-Ce-Si-O-N system could afford a viable compromise between sinterability and performance. This question was addressed in the following experiments:

Compositions within the basic formulation $aSi_3N_4 + bY_{2-x}Ce_xO_3 + cSiO_2$ were prepared using SN402 Si_3N_4, calcined yttrium and cercium oxylates, (Y_2O_3 and CeO_2) and Apache-0.03μSiO_2. In these formulations the SiO_2 content of the Si_3N_4 powder was not taken into consideration, and it was assumed that the reaction given below occurred during firing, as reported by Rae et al. (Ref. 20):

$$Si_3N_4 + 12CeO_2 \rightarrow 3SiO_2 + 6Ce_2O_3 + 2N_2.$$

(This procedure was simply for valence bookkeeping.) Compositions prepared are listed in Table 17. The powder batches were processed as described in section IIIA2b, without binder, cold pressed, and fired as described in Sections IIIA3, and IIIA5. No calcining step prior to firing was used. Firing conditions, and property data on the test bars, are listed in Table 18. Samples for mechanical testing were finished on the tensile face, and for oxidation testing were finished on all surface, to 600 grit SiC paper.

b) Densification

The average bulk densities of samples from a given batch are plotted as a function of composition in Fig. 31. Composition is plotted on a log scale in order to space out the points. Also plotted is the theoretical density of one series of compositions. This was calculated by assuming that the samples consisted of a mechanical mixture of the phase Si_3N_4 having a density of 3.20 g/cc, and the phase $Y_{2-x}Ce_xSi_2O_7$. The density of the latter phase was calculated by assuming the density of $Y_2Si_2O_7$ to be 4.15 g/cc and further assuming the lattice parameter of the phase did not change with substitution of Ce for Y. The theoretical density is seen to be essentially constant for all $x < 0.1$. There appears to be a systematic deviation from the theoretical value of the experimentally determined density of sintered samples for which $.02 < x < 1.33$, but in general this deviation is less than about 1.5 percent. This could be indicative of erroneous assumptions regarding the lattice parameters and/or phase constitution of the bodies. (As will be seen later, in fact fired bodies

TABLE 17

Compositions in the Y-Ce-Si-O-N System

Composition Number	Coefficients (1)				Weight Percent of Constituents			
	A	B	C	x	Si_3N_4	Y_2O_3	CeO_2	SiO_2
1134	83.93	5.36	10.71	0.3328	85.92	7.34	2.24	4.49
1137	"	"	"	0.1664	86.16	8.11	1.12	4.61
1138	"	"	"	0.0832	86.28	8.49	0.56	4.67
1139	"	"	"	0.0416	86.340	8.683	0.281	4.695
1140	"	"	"	0.0208	86.370	8.780	0.141	4.709
1141	"	"	"	0.0126	86.383	8.829	0.071	4.716
1142	"	"	"	0.0052	86.393	8.852	0.035	4.720
1145	90.46	4.77	4.77	0.010	90.301	7.611	0.058	2.030
1146	"	"	"	0.005	90.307	7.631	0.029	2.033

(1) In the formula A Si_3N_4 + BY_{2-x} Ce_x O_3 + C SiO_2

TABLE 18

FABRICATION AND TEST DATA For Y-Ce-Si-O-N SAMPLES

Sample Numbers	Firing Conditions Tempo (°C)	Time (hrs)	Bulk Density (g/cc)	Flexural Strength Temp °C	ksi	Mpa	1370°C, 10 ksi Creep Rate (hr^{-1})	Additional Tests
1134.1								1400°C oxidation
.2	1700	5	3.29					
.3			3.29					
1137.1								1400°C oxidation
.2	1700	5	2.33	25	79	543		
.3			3.26					
.4			2.34	25	70	484		
1138.1								1400°C oxidation
.2	1700	5	3.42	25	68	468		
.3			3.44					
.4			3.35	25	85	585		
1139.1								1400°C oxidation
.2	1700	5	3.35	25	66	454		
.3			3.38	25	78	536		
.4								
1140.1								1400°C oxidation
.2	1700	15	3.38	25	60	414		
.3			3.40	25	84	576		
.4								1000°C oxidation
.5			3.39				3.3×10^{-3}	
.6	1700	20	3.29	1370	64	440		
.7			3.28	1370	52	360		
.8			2.29					
.9				25	86	592		
.10	1700	10		25	64	440		
.11				25	85	584		1370°C oxidation
1141.1								1400°C oxidation
.2	1700	10	3.15				4.1×10^{-3}	
.3			3.18	1370	53	370		
.4			3.13	1370	50	345		
.5			3.18					
.6	1700	10	3.23	25	79	545		
.7			3.24	25	74	510		
.8			3.14	25	70	485		
1142.1								1400°C oxidation
.2	1700	10	3.03	25	68	470		
.3			2.98	25	71	490		
.4								1370°C oxidation
.5							4.2×10^{-3}	
1145.1			3.24				1.5×10^{-4}*	
.2	1700	15	3.24					1400°C oxidation
.3			3.26	25	80	550		1000°C oxidation
.4			3.26	25	73	505		
1146.1			3.19					
.2	1700	15	3.19					
.3			3.18					
.4			3.17					

* Average rate between 10th and 15th hour of test. Furnace failure curtailed run. See Text.

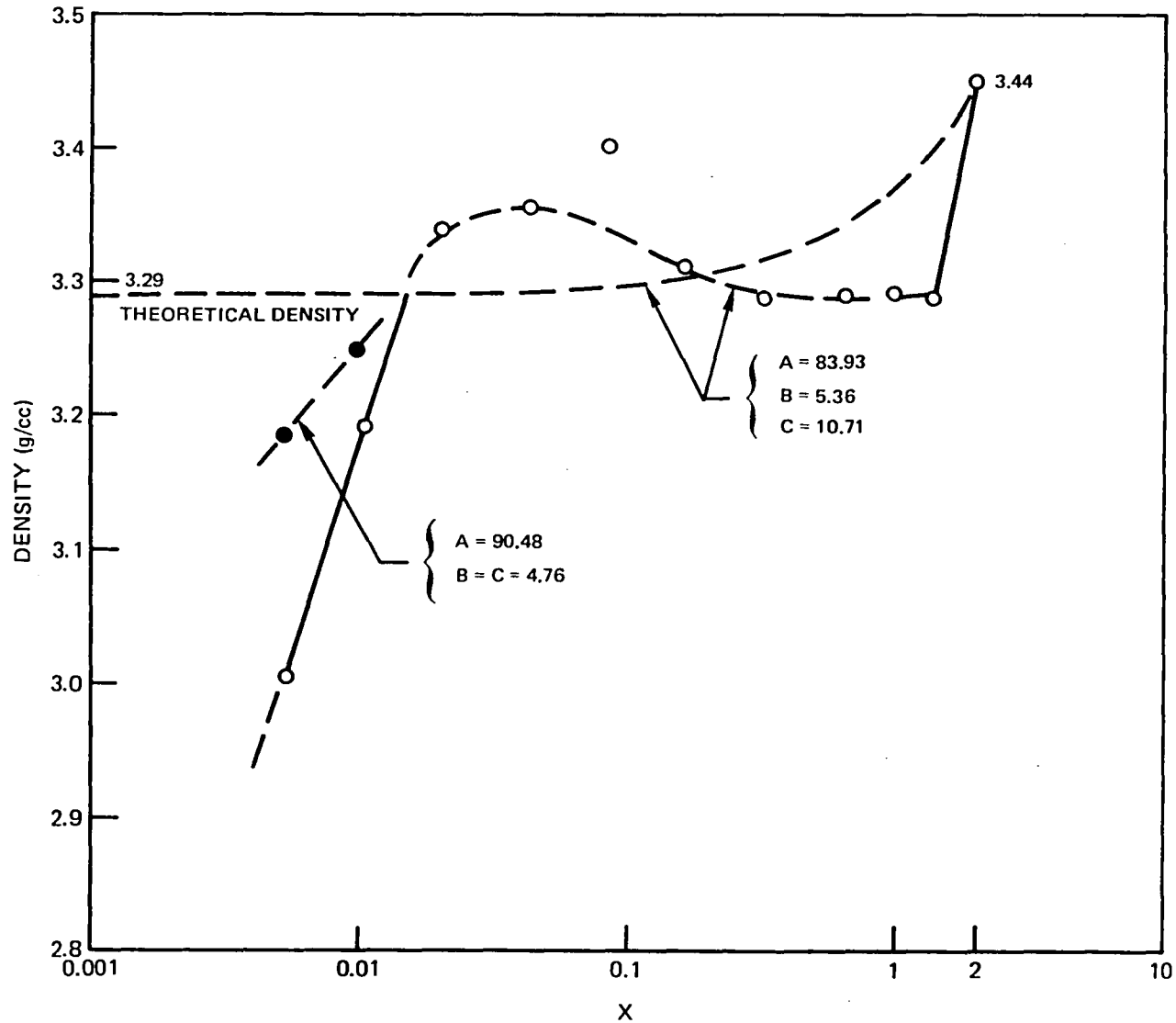

Figure 31 Density of Sintered Bodies of Compositions 94 Si_3N_4 6z ($y_{2-x}Ce_x$ Si_2O_7)

contained a glass phase). However, for the values of $x < 0.01$ there is a significant drop in density with decreasing x. It appears that the value $x = 0.01$ is near the lower limit of x for densely sintered bodies using the given fabrication parameters. This value of x corresponds to a solution in which one in every 200 of the rare earth type cations is cerium.

c) Oxidation Data

The 1400°C parabolic oxidation curves for samples of the various compositions are shown in Fig. 32. Following an initial period of decreasing rate lasting up to about 6 hrs, the oxidation appears to follow parabolic kinetics. The parabolic rate constants calculated from the slopes of the curves of Fig. 32 are plotted against composition on a log-log scale in Fig. 33. Note that the oxidation rate constant decreased monotonically with the variable x for the C = 2B series of compositions for $0.01 < x < 1$ (i.e. for all "theoretically dense" samples) but rose for the less dense sample 1.42 ($x = .005$). The minimum oxidation rate for this composition series (about 0.03 $mg^2cm^{-4}hr^{-1}$) was still a factor of 3 times the target rate of 0.01. XRD from the oxidized surface showed the scales to contain the crystalline phases $Y_2Si_2O_7$ and α-cristobalite. SEM of the oxidized surface, and metallography of transverse sections through the oxidized sample 1140.1 are shown in Fig. 34, and indicate the presence also of a major glassy phase.

Samples of composition 1145 exhibited the lowest oxidation (0.015 $mg^2cm^{-4}hr^{-1}$) which approaches the target value. The scale on sample 1145.1, shown in Fig. 35, is thin, with little glass present. XRD shows the scale to contain $Y_2Si_2O_7$ and cristobalite, with the former phase showing a strong 0k0 orientation with respect to the surface.

Samples of compositions 1140 and 1145 tested at 1000°C for 75 hrs showed essentially zero weight gain, and there was no evidence of cracking.

d) Mechanical Test Data

Room temperature flexural strengths for all of the Y-Ce-Si-O-N samples tested ranged from about 420 to 620 MPa (60 to 90 ksi), with an average value for 17, tests of 515 MPa (75 ksi). The average strength at 1370°C for composition 1140 and 1141 samples (4 tests) was 380 MPa (55 ksi). Those room temperature fracture surfaces that were examined by SEM were seen to initiate of processing flaws (voids), exemplified by Fig. 36. 1370°C fracture surfaces exhibited areas of slow crack growth.

The 1370°C, 69 MPa creep rates for several samples are listed in Table 18. All of the samples formulated as $ASi_3N_4 + BY_{2-x}Ce_xO_3 + 2BSiO_2$ (i.e., 94

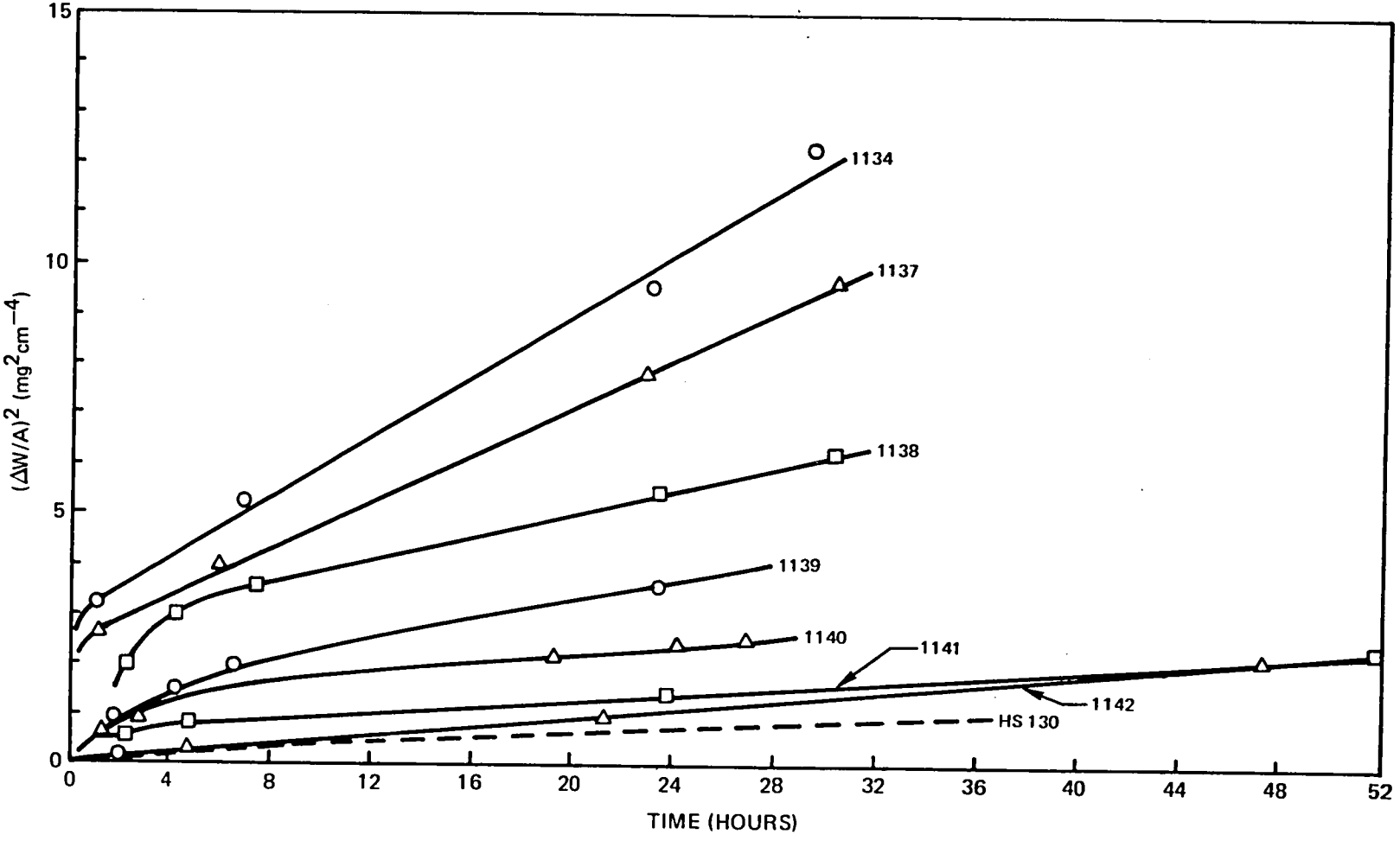

Figure 32 1400°C Oxidation Curves for Compositions 94 m/o Si_3N_4 + 6 m/o $Y_{2-x}Ce_xSi_2O_7$

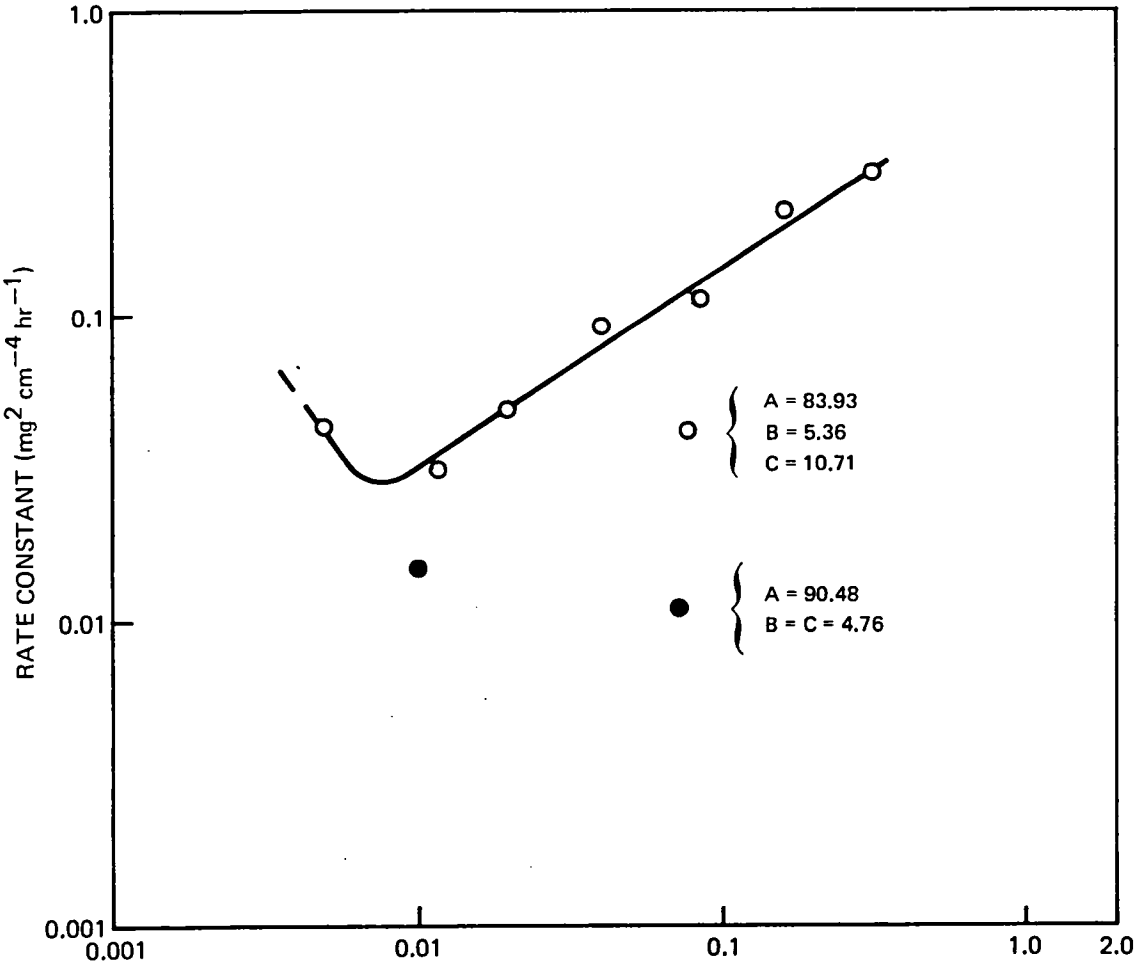

Figure 33 1400°C Parabolic Oxidation Rate Constants for Compositions 94 m/o Si_3N_4 6/6 m/o $Y_{2-x}Ce_xSi_2O_7$

79–04–137–40

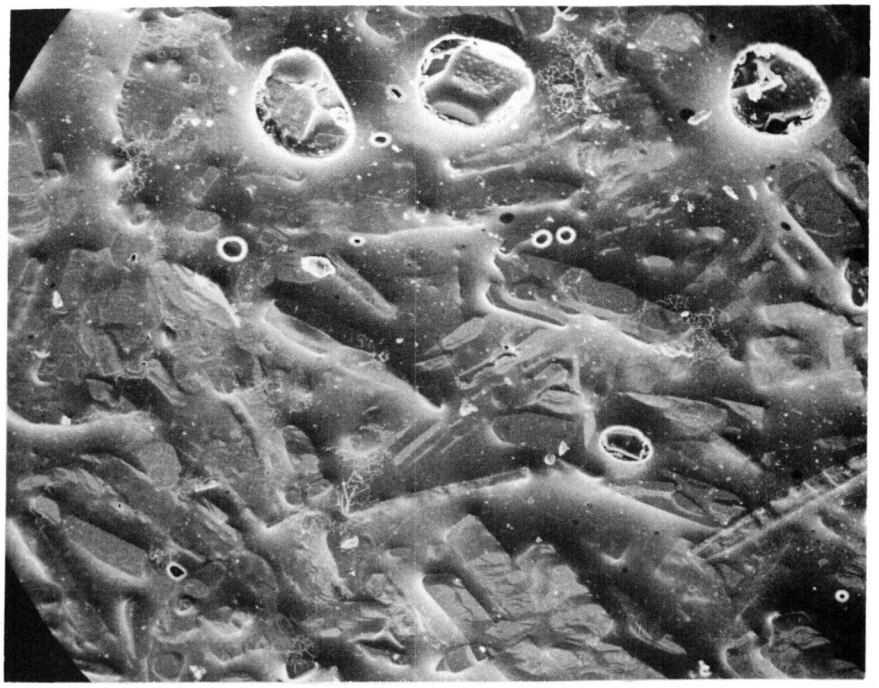

a) SEM, SURFACE, 30° INCIDENCE — 100μ

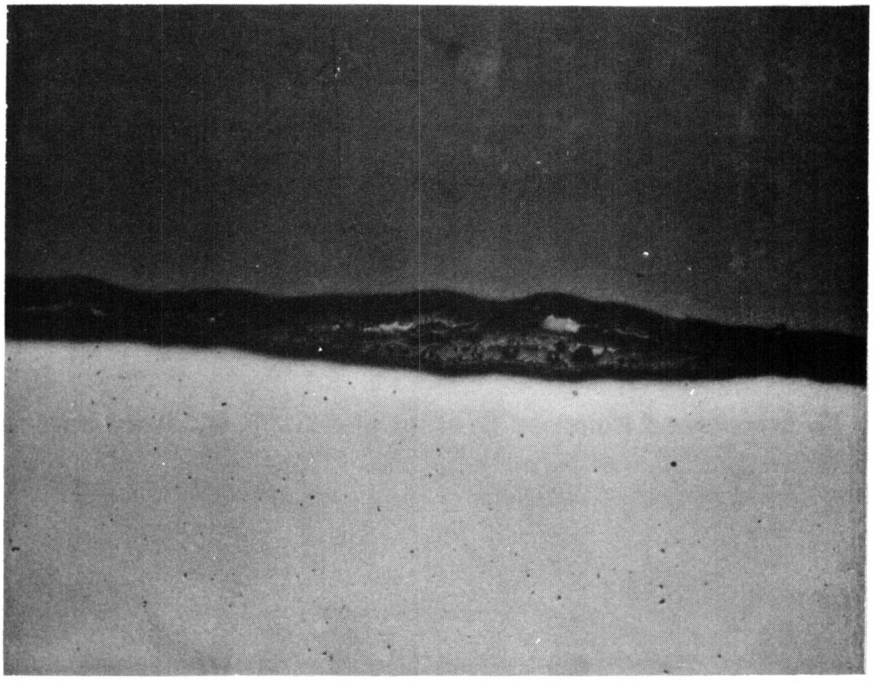

b) TRANSVERSE POLISHED SECTION — 100μ

Figure 34 Microscopy of 1400 °C Oxidized Sample 1140:1

79–04–137–46

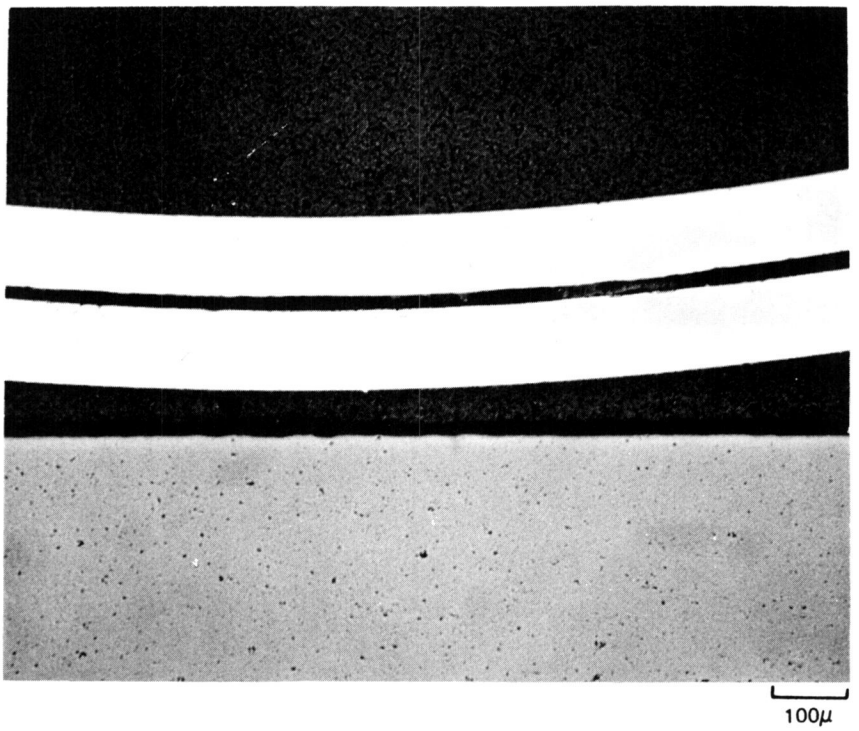

Figure 35 Tranversed Polished Section of 1400 °C Oxidized Sample 1145:2

79–04–137–45

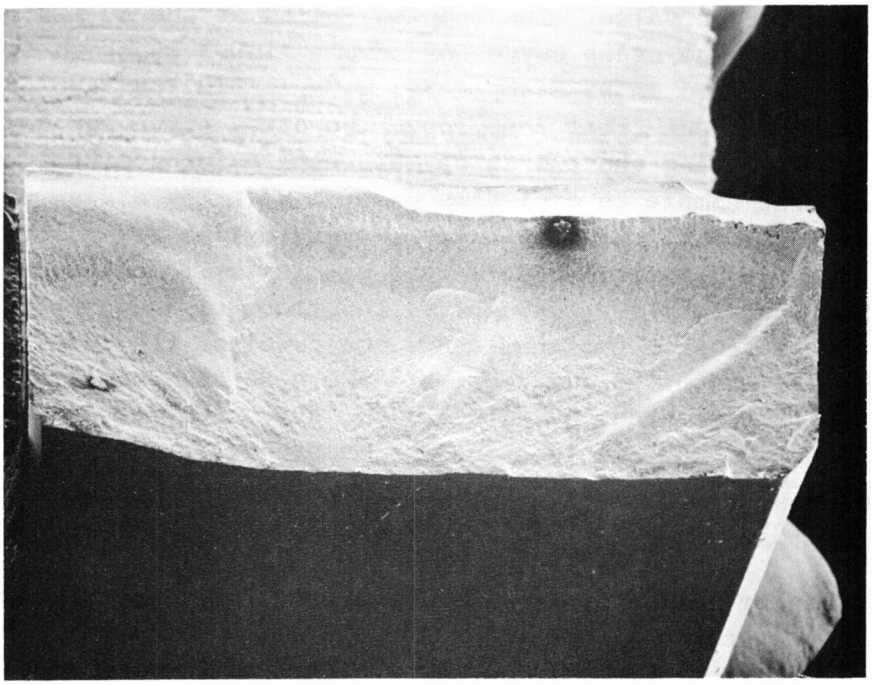

a) OVERALL (X13)

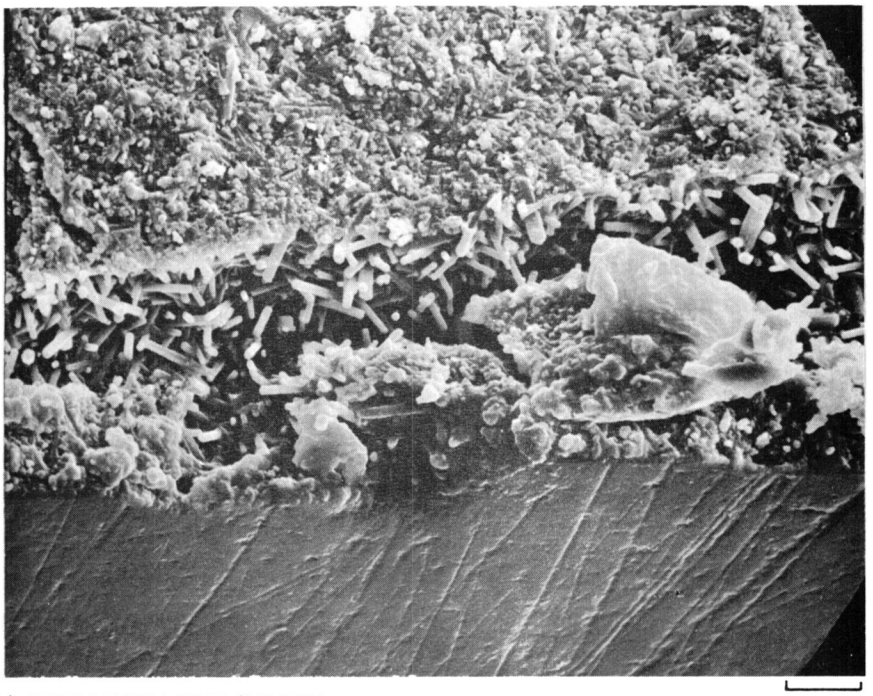

b) INITIATION SITE (X1000)

10μ

Figure 36 Fracture Surface of Sample 1140:9

79–04–137–44

Si_3N_4+ $6Y_{2-x}Ce_xSi_2O_7$) are seen to have creep rates about two orders of magnitude greater than the target value. The samples failed at the 69 MPa stress level after about 10 hrs. The creep curve for sample 1140.5 is shown in Fig. 37. Sample 1145.1 formulated as 95 Si_3N_4 + $5Y_{1.99}Ce_{0.01}SiO_5$) on the other hand, exhibited quite different creep behavior. The creep curve for this sample is shown in Fig. 38. During the course of the test, a furnace failure occurred which permitted the sample to cool-down under load. The strian rate of the time of furnace shut-down was 1.67×10^{-4} hr^{-1}. Information regarding sample strain during cool-down was not retrieved. After repairs were made, the sample was returned to the test facility, brought to temperature, load reapplied, and the test continued. Note that the sample did not continue the initial secondary creep curve, but instead exhibited a new primary and secondary creep behavior with a secondary creep rate of about 5×10^{-5} hr^{-1}. The samples failed after about 16 hrs of the second run without entering a tertiary creep regime.

e) Instrumental Analysis of Test Specimens

A rim of higher reflectivity around the exterior region of the fractured surface of creep specimen 1154.2 was noted under the binocular microscope, as shown in Fig. 39A. It was also noted that the external surface of the sample was discolored particularly in the region of contact with the tungsten loading bars. The fracture surface was examined in SEM, Backscatter electron microscopy (Fig. 39B) and EDS spectroscopy (Fig. 39C). No differences could be detected between the interior and exterior zones of the fracture surface using any of the above techniques. Fresh transverse fractures were made in the sample and showed the same characteristics as the original fracture surface.

One half of the specimen was waxed to a plate and thin layer of material removed to expose a clean surface of the lighter zone. An x-ray diffraction pattern was obtained from this surface. More material was then removed to expose a surface of the dark inner region, and again an XRD pattern obtained. Patterns were also obtained from the surfaces of room temperature test specimens of composition 1145, and also from powder obtained by crushing and comminuting room temperature test specimens of compositions 1145 and 1141. The low angle portions of some of the XRD patterns are reproduced in Fig. 40. In general, the patterns obtained from different samples of the powder obtained by crushing a single fired bar were quite variable in terms of the d-spacings and relative intensities of the low intensity minor phase peaks. In no case could the identity of the minor crystalline components be established with certainty. In the case of sample 1141.6 (and other C = 2B compositions that were X-rayed) the minor phase reflections were very faint, and it is assumed that the grain boundary material is largely glass, which could account for the high creep rate at 1370°C. What minor phase reflections were visible were around 3.07 and 2.89 Å, as exemplified by Fig. 40, Trace A.

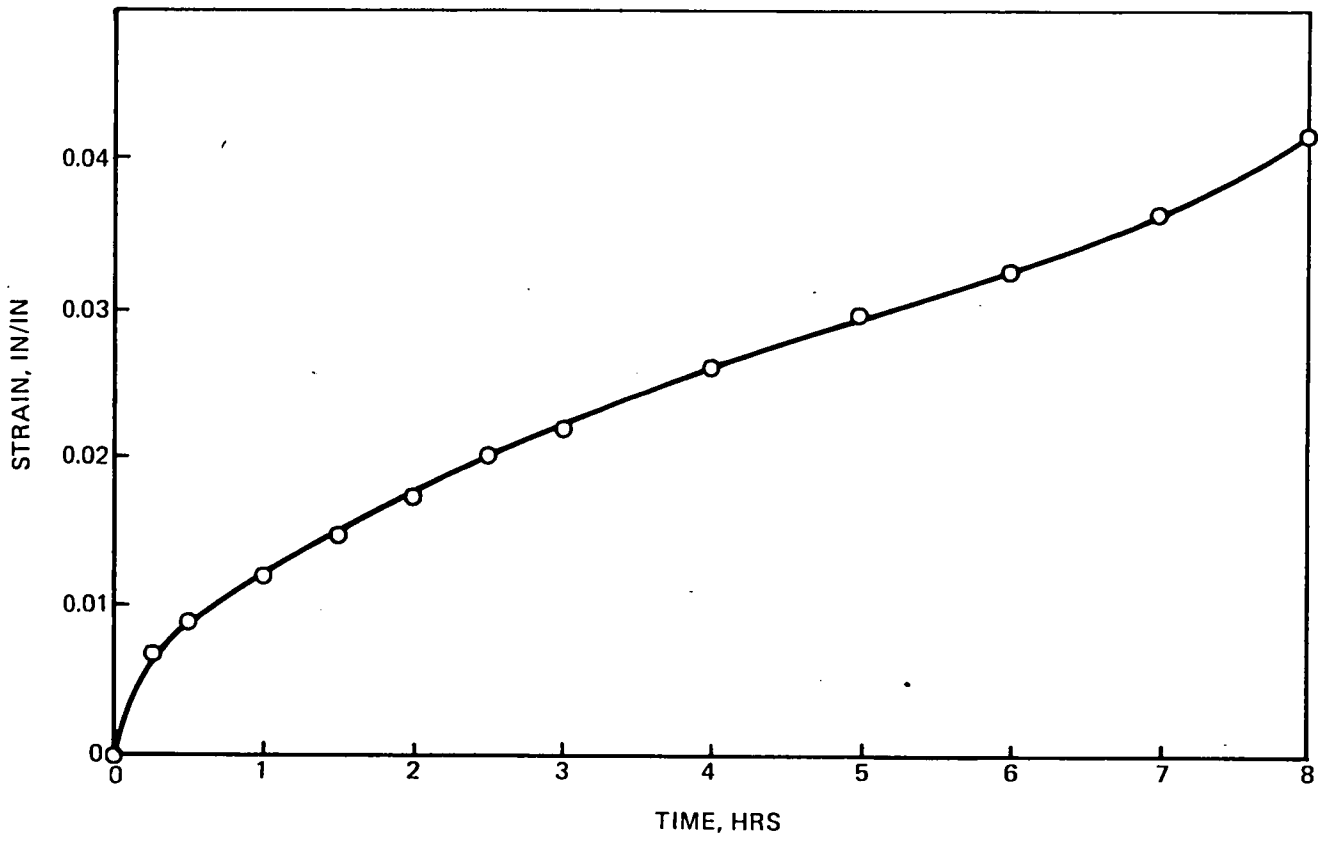

Figure 37 1370°C, 69 MPG Creep Curve for Sample 1140:5

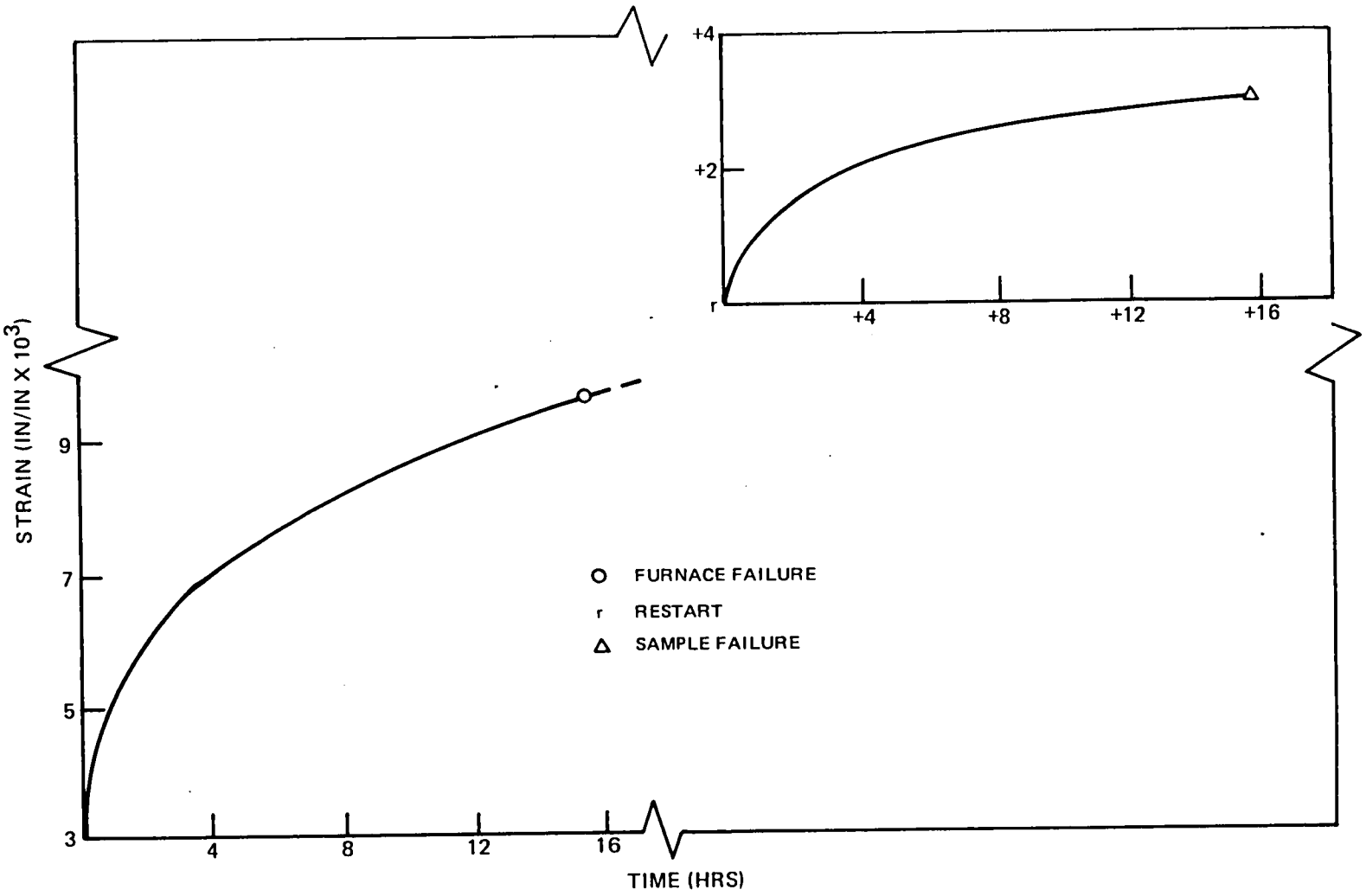

Figure 38 1370°C, 69 MPa Creep Curve for Sample 1145:1

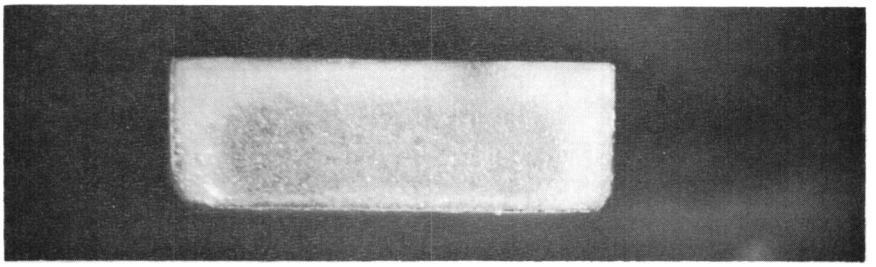

A) OPTICAL MACROGRAPH

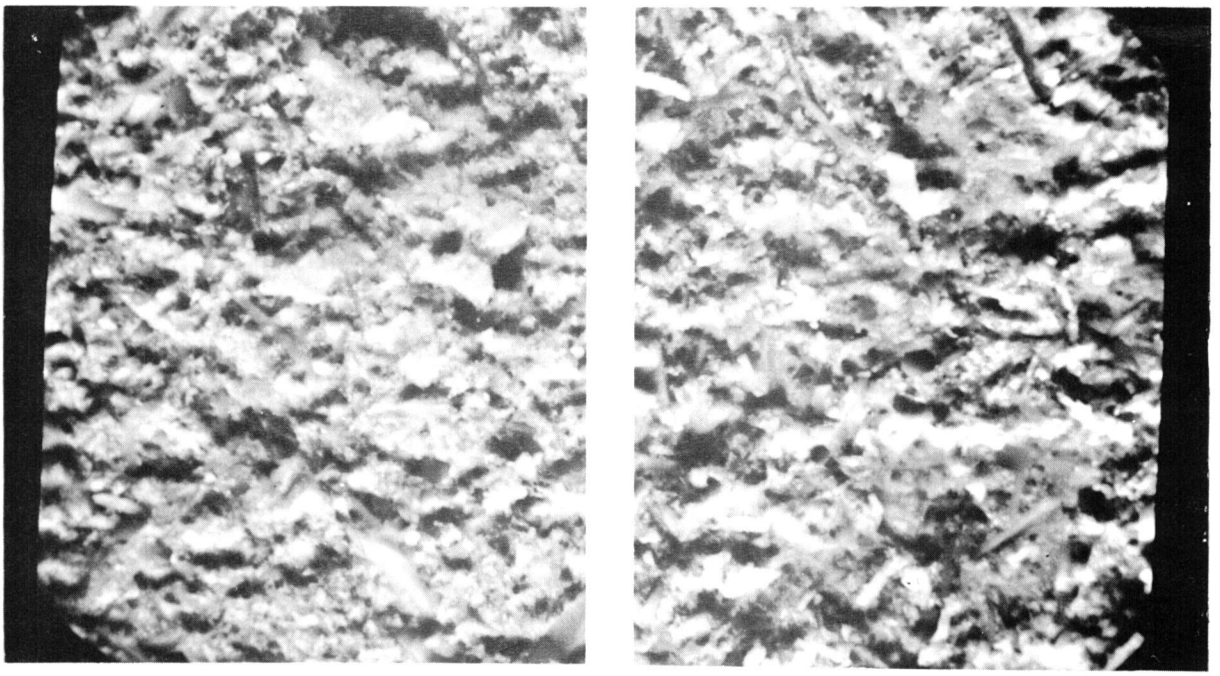

B) BACKSCATERED ELECTRON MICROGRAPHS

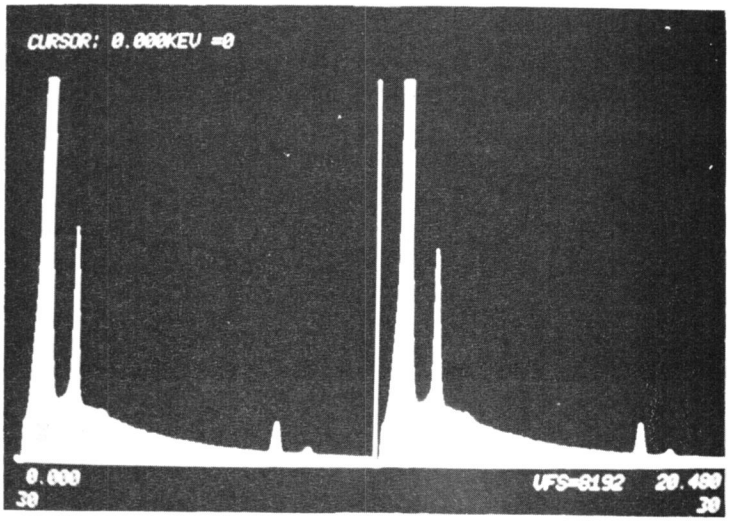

C) EDS SPECTRA, INSIDE AND OUTSIDE

Figure 39 Rim Around Creep Specimen 1145:2

79–04–137–41

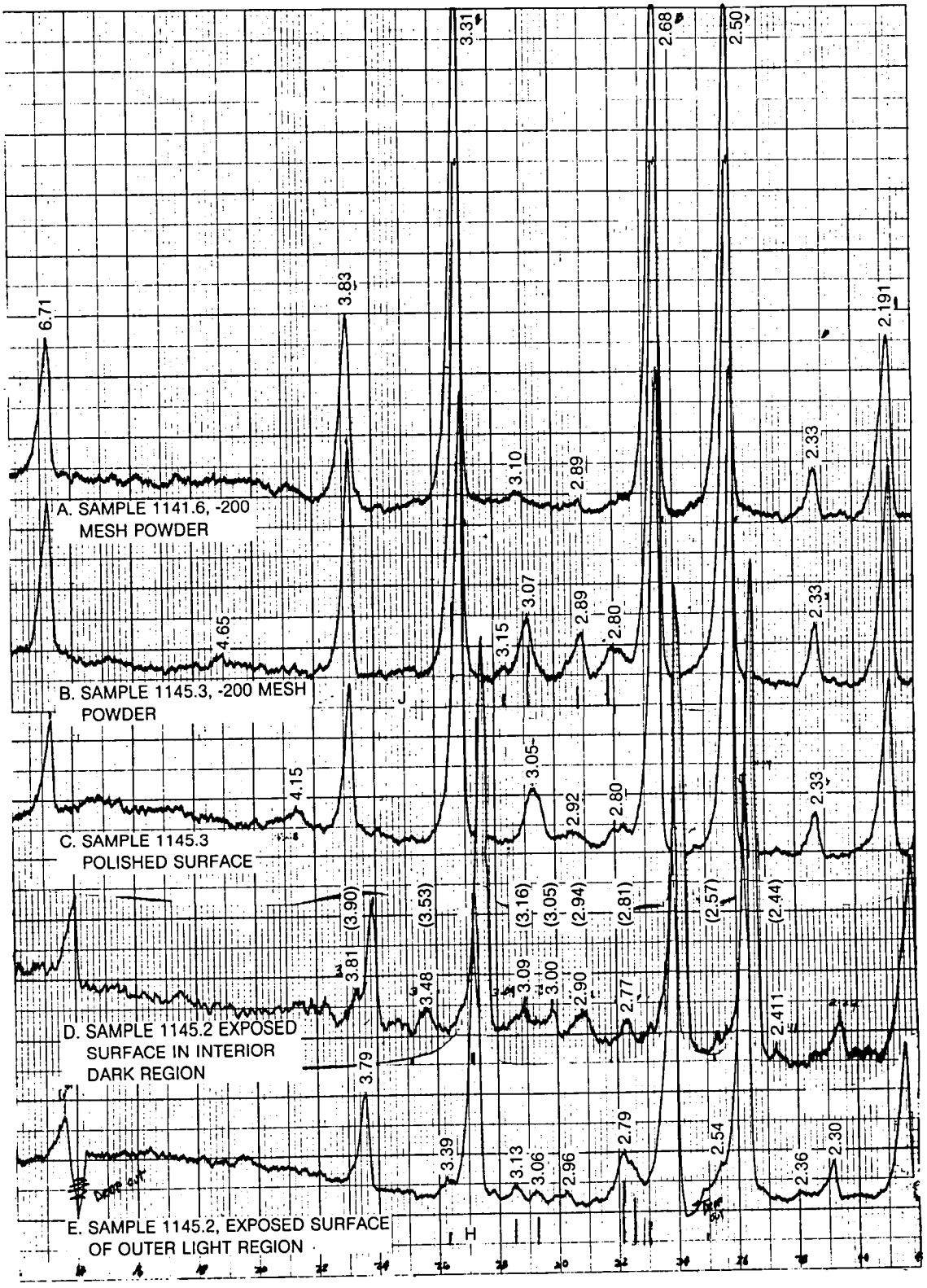

Figure 40 XRD Patterns for Some As-Fired and Heat Treated Y-Ce-Si-O-N Sample

79–09–65–2

For sample 1145.3 (C = B) which under equilibrium conditions should consist of major Si_3N_4, minor H phase, and trace $Y_2Si_2O_7$, intensities of minor phase peaks were substantially greater than for C = 2B samples. The strongest of these were centered around 3.05 to 3.07, 2.89 to 2.92, and 2.77 to 2.80 Å, with quite irreproducible relative intensities. Traces B and C are representative of the variability. Conceivable such variability could result from a non-uniform mixture of several of the $Y_2Si_2O_7$ modifications, perhaps with the additional presence of J phase. It also could perhaps result from the presence of poorly crystallized and/or highly stressed quench crystals. Whatever the true nature of the crystalline component in the grain boundaries, it is clearly a metastable assemblage.

After the 1370°C heat treatment in argon (i.e., the creep test), quite different XRD patterns were observed from surfaces exposed by grinding into the dark inner region, and the light outer region of the sample, as shown in Traces D and E, respectively. The outer region now clearly contains the (presumably) equilibrium H and $Y_2Si_2O_7$ phases.

The patterns from these surfaces apparently are displaced. What appears to be a large lattice shift for the Si_3N_4 is probably the spurious result of sample misalignment. When the sample was crushed to powder and the XRD pattern obtained, lattice parameters were within experimental error of those of the non-heat treated samples. The shifts are too great reasonably to be attributed to elastic strain in the heat treated sample, which would require a compressive stress on the order of 2000 MPa. Shifting Pattern D the indicated amount results in $\underline{d}$ values for the minor phase reflections shown in parenthesis above the original values. Taking into account the shifted $\underline{d}$ values, trace D indicates a new phase superimposed on the variable minor phase pattern in the original samples. This appears to be the X_2-Y_2SiO_5 phase, although again such an identification cannot be considered as highly reliable.

While the creep sample showed evidence of phase transformations in the grain boundaries during 1370°C heating under stress in argon atmosphere, the samples which were heated in air at 1370°C for 100 hours gave no evidence of grain boundary transformation (save for minimal surface oxidation). The above results lead one to suspect that the metastability of non-equilibrium grain boundary phases, at least in some Si_3N_4-R_2O_3-SiO_2 bodies can be radically altered by environment and/or stress. Further development of S_3N_4 bodies from derivations of the Si_3N_4-Y_2O_3-SiO_2 system must pay particular attention to optimizing grain boundary composition and heat treatments to insure long term stability under anticipated stress and environment.

REFERENCES

1. Jack, K. H. and W. I. Wilson: Ceramics Based on the SiAlON and Related Systems, Nature Phys. Sci., pp. 238, 8028, 1972.

2. Oyama, Y. and O. Kamigaito: Solid Solutility of Some Oxides in Si_3N_4. Japan J. Appl. Phys. 10, p. 1637, 1972.

3. Morgan, P. E. D.: Paper 4-52-74, American Ceramic Society Meeting, April 1974. Also, J. Amer. Ceramic Society, pp. 53, 392, 1974.

4. Land, P. L., et al: Paper 68-B-75, American Ceramic Society Meeting, Washington, D. C., May 6, 1975, and J. Amer. Ceramic Society, pp. 61, 56, 1978.

5. Gauckler, L. J., et al: Paper 67-B-75, American Ceramic Society Meeting, Washington, D. C., May 6, 1975. Also, J. American Ceramic Society, pp. 58, 346, 1975.

6. Layden, G. K.: Process Development for Pressureless Sintering of SiAlON Ceramic Components, Final Report, Naval Air System Command Contract N00019-75-C-0232, February 1976.

7. Jack, K. H.: SiAlONs and Related Nitrogen Ceramics, J. Mat. Sci. 11, pp. 1135-1158, 1976.

8. Jack, K. H.: Trans. Brit. Ceram. Soc. 7, p. 376, 1972.

9. Huseby, I. C., H. L. Lucas and G. Petzow: J. Amer. Ceramic Soc., 58, p. 377, 1975.

10. Gauckler, L. J., H. L. Lucas and T. Y. Tien: Mat. Res. Bull., 11, p. 503, 1976.

11. Layden, G. K.: Pressureless Sintering of SiAlON Gas Turbine Components, Report Number NADC-75207-30, February 23, 1977.

12. Layden, G. K.: Final Report, Contract N62269-77-C-0248 for Naval Air Development Center, Warminster, PA, p. 18974, January 27, 1979.

13. Mazdiyasni, K. S. and C. M. Cooke: American Ceramic Society Bulletin, 53, p. 392, 1974, abstract.

REFERENCES (Cont'd)

14. Wills, R. R.: Journal of the American Ceramic Society 57, 1974.

15. Lange, F. F.: Final Report, Contract N00019-73-C-0208, February 26, 1974.

16. Rice, R. W. and W. J. McDonough: American Ceramic Society Bulletin 54, p. 406, 1975, abstract.

17. Terwilliger, G. R. and F. F. Lange: Pressureless Sintering of Si_3N_4, J. Mat. Sci. 10, pp. 1169-1174, 1975.

18. Gazza, G. E: Effect of Y_2O_3 Additions on Hot-Pressed Si_3N_4, Bulletin of the American Ceramic Society 54, pp. 778-781, 1975.

19. Venables, J. D., D. K. McNamara, and R. G. Lye: High Strength Silicon Nitride Prepared with Eutectic Flux Additions, F. L. Riley, Editor, Nitrogen Ceramics, Proceedings of the N.A.T.O. Advanced Study Institute, Canterbury, August 1976.

20. Rae, A.W.J.M., D. P. Thompson, and K. H. Jack: The Role of Additives in the Densification of Nitrogen Ceramics, presented the NATO Advanced Study Institute on Nitrogen Ceramics, Canberbury, England, August 1976.

21. Layden, G. K.: Development of SiAlON Materials, NASA CR 135290, December 1977.

22. Layden, G. K. and S. Holmquist: Ninth Quarterly Progress Report on NASA Control NAS3-19712, February 1978.

23. Juza, R., A. Rabenau and I. Nitschke: Z. Anorg. Allg. Chem., p. 332, 1964, 1-4.

24. Aramaki, S. and R. Roy: J. Am. Ceram. Soc., 42, (12) p. 644, 1959.

25. Welch, J. W.: Nature. 186, (4724), p. 546, 1960.

26. Geller, R. F. and S. M. Lang: National Bureau of Standards. 1959, Phase Diagram for Ceramists, Fig. 361.

27. Butterman, W. C. and W. R. Foster: Am. Mineralogist, 52, p. 884, 1967.

28. Lejus, A.: Rev. Hautes Temper. et Refract. t. 1, p. 53, 1964.

REFERENCES (Cont'd)

29. Gilles, J. C.: Corrosion Anti Corrosion. 12, (1), p. 15, 1964.

30. Claussen, N. E., R. Wagner, L. J. Gauckler and G. Petzow: Ceramic Bulletin, 56, #3, p. 301, 1977, abstract.

31. Kordyuk, R. A. and N. Y. Gulko: Dokl. Akad. Nauk. SSSR, p. 154, (5), p. 1183, 1964.

32. Herold, P. G. and W. J. Smothers: J. Am. Ceram. Soc., 37, (8), p. 353, 1954.

33. Sorrell, C. A. and C. C. Sorrell: J. Am. Ceram. Soc., 60, (11), p. 495, 1977.

34. Olds, L. E. and H. E. Otto: In Phase Diagram for Ceramists. The Am. Ceram. Soc., Fig. 311, 1964.

35. Toropov, I. A. et al.: ibid, Fig. 2344.

36. Noguchi, T. and M. Mizuno: ibid, Fig. 4370.

37. Toropov: ibid, Fig. 2388.

38. Bondar and Galakov: ibid, Fig.

39. Wills, R. R. et al.: J. Mat. Sci., 11, p. 1305, 1976.

40. Lange, F. F., S. C. Singhal and R. C. Kuzniki: J. Am. Ceram. Soc., 60, p. 249, 1977.

41. Holmquist, S.: Report, U. S. Air Force Contract F33615-C-4155.

42. Tien, T. Y.: Technical Report # 014536-78-1, Contract No. AFOSR-76-3078.

43. Arias, A.: NASA Technical Paper, p. 1249, 1978.

44. Dutte, S.: NASA Technical Memorandum, p. 78950, 1977.

45. Bacon, J.: Final Report Contract NASW-1301 and NASW-2013, January 1971.

46. Weaver, G. Q. and J. W. Lucek: Am. Ceram. Soc. Bull. 57, p. 1131, 1978.

REFERENCES (Cont'd)

47. Brennan, J. J.: Third Quarterly Progress Report Contract NAS3-21375, April 1979.

48. Morgan, R. A. and F. A. Hummel: J. Am. Ceram. Soc., 32, 1949.

49. Olds, L. E., and H. E. Otto: In Phase Diagrams for Ceramists, Am. Ceram. Soc., Fig. 311, 1964.

50. Bartram, S. F.: G. E. Co. Report DC 61-7-10, (see. Ref. 53).

51. Wier, C. E., and A. Van Valkenburg: J. Res. N.B.S., 64A, p. 103, 1959.

52. Potter, R. A.: Met. Div. Rept. ORNL-2988, p. 180, Oak Ridge Labs, 1965.

53. Harris, L. A. and H. L. Yakel: Acta Cryst. 22, p. 354, 1967.

54. Bartram, S. F.: Acta Cryst. 1325, p. 791, 1969.

55. Huseby, I. C., H. L. Lukas and G. Petzow: J. Am. Ceram. Soc. 58, p. 377, 1975.

56. Jack, K. H.: J. Mat. Sci. 11, p. 1135, 1976.

APPENDIX A

COMPOSITIONS INVESTIGATED IN THE YSiAlON SYSTEM, AND TEST RESULTS

Join	Molecular Formula Y	Si	Al	O	N	Components Y_2O_3	Si_3N_4	SiO_2	Al_2O_3	AlN	Firing Conditions Temp °C	time hrs	Shrinkage (%)	Phases Present	Observations
$Y_4Al_2O_9$ - $Y_4Si_2O_7N_4$	4	1	1	8	1	2	0	1	0	1	1750	1	5	YAM_{ss}	
						8	1	1	2	0	1750	1	5	YAM_{ss}	
$Y_3Al_5O_{12}$ - "$Y_3Si_5O_7N_5$"	3	0	5	12	0	3	0	0	5	0	1550	1	2	YAG	
	3	2	3	10	2	3	1	1	3	0	1600	1	15		
											1550	1	5	sYAG, w 3.03, 2.87, 2.79, 2.74	
											1500	1	3		Bloated
	3	1	4	11	1	3	0	2	3	2	1475	1	4		
											1525	1	6	sYAG, w H	
											1600	1			Melted
						6	1	1	8	0	1475	1	2		
											1525	1	4	sYAG, w H	
											1600	1			Melted
	3	2	3	10	4	3	1	1	3	0	1475	1	4		
											1525	1	4	sYAG, w J, w H	
											1600	1			Melted
	6	5	5	19	5	3	0	5	0	5	1475	1	2		
											1525	1	2	sYAG, m H	
											1600	1			Melted
						12	5	5	10	0	1475	1	2		
											1525	1	2	sYAG, m H, w J	
											1600	1			Melted
	3	4	1	8	4	3	2	2	1	0	1475	1	0		
											1550	1	4	sH, m YAG, w α Si_3N_4	
											1600	1	17		
	3	3	2	9	2	6	3	3	4	0	1475	1	2		
											1525	1	3	sYAG, m H, w J	
											1600	1			Melted
$SiAl_2O_2N_2$ - Y_2O_3	2	3	6	9	6	1	1	0	2	2	1300	1	0		
											1600	1	0		
											1625	1	15	w YAG, w, ξ	
											1700	1			Bloated
							1	3	0	6	1575	4	0	sYAG, m 2.81, ξ, ϵ	
											1625	1	-2	sYAG, tr β' tr ϵ	
											1650	1	5		
											1700	1	4	sYAG	
											1725	1		mYAG	Melted
	1	6	12	15	12	1	0	6	0	12	1625	1	-3	sYAG, w β', tr ξ, ϵ	
	6	6	12	21	12	3	0	6	0	12	1625	1	-2	sYAG. w $Y_2Si_3O_3N_4$, tr ϵ	
$SiAl_4O_2N_4$ - Y_2O_3	2	3	12	9	12	1	0	3	0	12	1725	1	1		
											1750	2	1	sYAG, s ϵ	
						1	1	0	2	8	1725	1	8		
											1750	2	10	sYAG, s ϵ	
$SiAl_2O_2N_2$ - $Y_2Si_3O_3N_4$	2	6	6	9	10	1	2	0	2	2	1600	2	1		
											1625	1	1	s YAG, m β'	
											1700	1	17		
						1	1	2	0	6	1600	2	1		
											1625	1	1	s YAG, m β'	
											1700	1	16		
$SiAl_2O_2N_2$ - $Y_4Si_2O_7N_2$	8	13	18	32	22	12	13	0	20	14	1425	7	15	s YAG, many v.w.	
											1550	1	1		
											1650	1	15		
											1700	2			Bloated
						4	1	10	0	18	1425	7	7	s YAG, m 2.8, many v.w.	
											1550	1	0		
											1700	1			Foamed
$SiAl_4O_2N_4$ - $Y_2Si_3O_3N_4$	2	6	12	9	16	1	1	3	0	12	1650	1	0	s YAG, m $Y_2Si_3O_3N_4$, m ϵ	
											1700	1	2	m ϵ, ξ	
						1	2	0	2	8	1650	1	10	s YAG, m $Y_2Si_3O_3N_4$, m ϵ	
											1700	1	13	m ϵ, ξ	
$Y_2Si_3O_3N_4$ - AlN	2	3	4	3	8	1	1	0	0	4	1650	1	0		
											1750	1	0	s $Y_2Si_3O_3N_4$, AlN	
	2	3	2	3	6	1	1	0	0	2	1650	1	0		
											1750	1	0	s $Y_2Si_3O_3N_4$, AlN	
$SiAl_2O_2N_2$ - $Y_2SiO_2N_2$	2	5	6	10	8	3	5	0	7	4	1600	1	2		White
											1650	1	15		Black
						4	3	11	2	20	1600	1	-3		Grey
											1650	1	12		Black
$Si_3Al_6O_{12}N_2$ - Y_2O_3	2	6	12	27	4	1	1	3	6	0	1325	1	2		
											1400	1	17		
						1	0	6	4	4	1325	1	3		
											1400	1	11		
											1500	1			Bloated
$SiAl_4O_2N_4$ - $Y_4Al_2O_9$	4	6	26	21	24	2	0	6	1	24	1650	1	-2		
											1700	1	0	sYAG, m ϵ, w 2.81	
						2	2	0	5	16	1650	1	1		
											1700	1	7	sYAG, m ϵ, w 2.81	
$SiAl_4O_2N_4$ - $Y_3Al_5O_{12}$	6	9	46	42	36	3	0	9	5	36	1650	1	0		
											1700	1	-1	s YAG, m ϵ	
						6	3	0	11	24	1650	1	2		
											1700	1	4	s YAG, m ϵ, w ξ	

APPENDIX B

BATCH COMPOSITIONS FOR VARIOUS TEST SAMPLES

TABLE 5

BATCH COMPOSITIONS OF TEST BARS

Batch Number	Weight Percent of Components				
	Si_3N_4	SiO_2	Y_2O_3	Al_2O_3	AlN
1078	67.98	5.82	25.00	1.19	-
1079	79.94	2.82	12.12	5.12	-
1080	65.24	7.45	14.00	9.49	3.82
1081	52.06	7.43	13.97	18.92	7.61

Table 7

Batch Compositions

Comp. No.	Molecular Composition	Batch Constituents (w/o) Si_3N_4	Al_2O_3	AlN	Be_2SiO_4	Y_2O_3
1082	$Si_{5.42}Al_{.29}Be_{.29}O_{.87}N_{7.13}$	88.74	3.73	1.5	6.03	0
1083	$Si_{2.71}Be_{.29}O_{.58}N_{3.42}+.15Y_2O_3$	71.46	0	0	9.36	19.18
1084	$Si_{2.66}Be_{.34}O_{.68}N_{3.32}+.022Y_2O_3$	81.84	0	0	13.16	5.00

TABLE 2

COMPOSITIONS STUDIED

Batch No.	Composition (mole percent)			Constituents (Weight Percent)				
	β or β'	$Y_3Al_5O_{12}$	$Y_2Si_2O_7$	Si_3N_4	SiO_2	Al_2O_3	AlN	Y_2O_3
1085	95 Si_3N_4	5	0	81.78	0	7.82	0	10.40
1086	95 Si_2AlON_3	5	0	54.24	0	27.49	7.92	10.34
1087	95 $SiAl_2O_2N_2$	5	0	26.98	0	46.96	15.77	10.29
1088	95 Si_3N_4	4	1	83.04	0.75	6.36	0	9.85
1089	95 Si_3N_4	3	2	84.25	1.53	4.87	0	9.35
1090	95 Si_3N_4	2	3	85.60	2.33	3.30	0	8.77
1091	95 Si_3N_4 + 2.5 $SiAl_4O_2N_4$ + 2.5 $Y_2Si_3O_3N_4$			62.82	0	22.83	10.56	3.79

TABLE 1

COMPOSITIONS OF TEST SAMPLES INVESTIGATED

Composition Number	Intended Phase Composition (m/o)	Weight Percent of Constituents (1) Si_3N_4 KBI	Si_3N_4 SN402	SiO_2	Al_2O_3	AlN	Y_2O_3	Other	Grinding Media Al_2O_3	Grinding Media Si_3N_4	Phases Observed by x-rays
1103	95 Si_3N_4, 2.5 $Y_3Al_5O_{12}$, 2.5 $Y_2Si_2O_7$	82.85	0	2.02	6.36	0	8.77	0	x		
1104	97.5 Si_2AlON_3, 2.5 $Y_3Al_5O_{12}$	58.36	0	1.52	24.73	9.99	5.40	0	x		s β'
1105	95 Si_2AlON_3, 2.5 $SiAl_4O_2N_4$, 2.5 $Y_2Si_3O_3N_4$	62.42	0	1.61	20.21	12.00	3.77	0	x		s β', w 15R
1105A	95 Si_2AlON_3, 2.5 $SiAl_4O_2N_4$, 2.5 $Y_2Si_3O_3N_4$	63.25	0	0.39	20.45	12.14	3.81	0		x	s β', w 15R
1111	95 Si_3N_4, 2$Y_3Al_5O_{12}$, 3 $Y_2Si_2O_7$	81.62	0	2.29	3.65	0	12.44	0	x		
1112	95 Si_3N_4, 3$Y_2Si_2O_7$, 2 $Si_3Al_6O_{12}N_2$	87.69	0	3.57	4.33	0	4.41	0	x		
1113	95 Si_3N_4, 5 $Y_2Be_2SiO_7$	87.03	0	1.78	0	0	0	11.19 $Y_2Be_2SiO_7$		x	s β' w $Y_2Be_2SiO_7$
1114	95 $Si_{2.5}Al_{.5}O_{.5}N_{3.5}$ 2.5 $YSi_3O_3N_4$ 2.5 $SiAl_4O_2N_4$	78.33	0	1.58	12.53	3.60	3.96	0		x	
1115	81.4 $Si_{2.5}Al_{.5}O_{.5}N_{3.5}$ 16.1 $SiAl_4O_2N_4$ 2.5 $Y_2Si_3O_3N_4$	64.72	0	1.31	15.7	14.68	3.59	0		x	s β', w $2H^{\delta}$
1116	94 Si_3N_4, 6 $Y_2Si_2O_7$	54.49	27.52	6.36	3.06	0	8.57	0	x		
1116A	94 Si_3N_4, 6 $Y_2Si_2O_7$	56.38	28.72	6.10	0	0	8.79	0		x	
1116B	94 Si_3N_4, 6 $Y_2Si_2O_7$		85.76	5.50	0	0	8.74	0		x	
1116C	94 Si_3N_4, 6 $Y_2Si_2O_7$		84.07	5.39	0	0	8.57	2 carbowax		x	
1117	85 Si_3N_4, 9Si_2N_2O, $Y_2Si_3O_7$, 4$Y_2Be_2SiO_9$	54.34	27.69	5.88	0	0	8.47	1.45 BeO 2.17 carbowax		x	
1118	80 Si_3N_4, 17.5 $Si_3Al_6N_{10}$ 2.5 Y_2O_3	72.68		1.46	0	22.86	3.00			x	

(1) Values listed include contribution from grinding media wear, and SiO_2 impurity in Si_3N_4

Table 1 (Cont)

Composition of Test Samples

Composition Number	Intended Phase Composition, (m/o)	Weight Percent of Constituents					
		Si_3N_4 (1)	SiO_2	Y_2O_3	CeO_2	Al_2O_3	BeO
1119	94 Si_3N_4, 6 $Ce_2Si_2O_7$	83.64	3.40	0	12.96	0	0
1120	94.5 Si_3N_4, 4.5 $Ce_2Si_2O_7$, 1 $Ce_3Al_5O_{12}$	83.26	2.25	0	12.90	1.59	0
1122	94 Si_3N_4, 5 $Ce_2Si_2O_7$ 1 $Ce_2Be_2SiO_7$	83.70	3.20	0	12.97	0	0.31
1123	94 Si_3N_4, 3 Ce_2SiO_7 3 $Ce_2Be_2SiO_7$	83.80	3.61	0	12.98	0	1.50
1124	94 Si_3N_4, 1 $Ce_2Si_2O_7$ 5 $Ce_2Be_2SiO_7$	83.91	1.51	0	13.00	0	1.57
1125	97 Si_3N_4, 3 Ce_4BeSiO_9	86.53	0	0	13.00	0	0.47
1126	97 Si_3N_4, 3 Y_4BeSiO_9	89.42	1.18	8.90	0	0	0.49

(1) SN402

Table 1 (Cont)

Compositions of Test Samples

Composition Number	Intended Phase Composition, (m/o)	Weight Percent of Constituents				
		Si_3N_4(1)	SiO_2	Y_2O_3	CeO_2	Other
1129	$94Si_3N_4$, $6Ce_2Si_2O_7$	83.64(2)	3.40	0	12.96	
1130	$94Si_3N_4$, $6Ce_2Si_2O_7$	83.64(3)	3.40	0	12.96	
1131	$94Si_3N_4$, $6CeYSi_2O_7$	85.99	2.92	4.39	6.70	
1132	$94Si_3N_4$, $6Ce_{1.33}Y_{0.67}Si_2O_7$	84.54	3.82	2.88	8.76	
1133	$94Si_3N_4$, $6Ce_{0.67}Y_{1.33}Si_2O_7$	85.46	4.27	5.83	4.44	
1134	$94Si_3N_4$, $6Ce_{0.33}Y_{1.67}Si_2O_7$	85.92	4.49	7.34	2.24	
1135	$94Si_3N_4$, 6 GdSm Si_2O_7	82.22	4.49	0	0	13.29 $GdSmO_3$
1136	$94Si_3N_4$, 6 $NdSi_2O_7$	82.82	4.53	0	0	12.68 Nd_2O_3
1137	$94Si_3N_4$, $6Ce_{0.17}Y_{1.83}O_7$	86.16	4.61	8.11	1.12	
1138	$94Si_3N_4$, $6Ce_{0.08}Y_{1.92}O_7$	86.28	4.67	12.98	0.86	

1) SN_4O_2 unless otherwise noted
2) KBI high purity grade
3) Stark hot pressing grade

APPENDIX C

FABRICATION AND TEST DATA FOR VARIOUS TEST SAMPLES

TABLE 6

Fabrication and Test Data for SiAlON Compositions

Batch Number	Sample Numbers	Firing Conditions: Time (hr)	Firing Conditions: Temp (°C)	Average Density Data: Apparent Porosity (40)	Average Density Data: Specific Gravity ($kgm^{-3} \times 10^{-3}$)	Average Density Data: Bulk Density ($kgm^{-3} \times 10^{-3}$)	Phases Observed by X-Ray Diffraction
1078	1,2,3	1	1700	0.2	3.53	3.51	Surface: sβ ,sδ $Y_2Si_2O_7$. About 0.02 cm below surface: sβ', wK + w 3.0 Å. Crushed sample, sβ' + m J_{ss}
	4,5,6	2	1765	0.2	3.55	3.54	
	7,8,9	1	1790	1	3.48	3.44	
1079	1,2,3	1	1725	6	3.39	3.25	β' only
	4,5,6	2	1765	0	3.39	3.38	
	7,8,9	2	1770	1	3.36	3.33	
1080	1,2,3	2	1750	bloated, large internal voids			β' only
	4,5,6	1	1580	0	3.56	3.56	sβ' + w αSi_3N_4
	7,8,9	1	1525	0	3.36	3.36	
1081	1,2,3	2	1710	bloated, large internal voids			β' only
	4,5,6	2	1650	bloated, large internal voids			
	7,8,9	1	1550	0	3.24	3.24	

TABLE 3

SAMPLE FIRING AND CHARACTERIZATION DATA

Sample Number	Firing Conditions: T (°C)	Firing Conditions: Time (hrs)	Density Data: Apparent Porosity (%)	Density Data: Bulk Density (g/cc)	Density Data: Specific Gravity (g/cc)	Notes	Minor Phases
1085.1	1725	2	7	3.01	2.80		
1085.2	1715	2	<1	3.14	3.14	refired 64 hrs at 1400°C	YAG
1085.3			<1	3.22	3.23		glass
1085.4			<1	3.18	3.19		
1086.1	1725	2	1	3.11	3.13		
.2	1760	2	1	3.13	3.16	refired	YAG
.3			1	3.17	3.19		$SiAl_4O_2N_4$
1087.1	1775	2				melted	
.2						reduced	
.3	1725	2	17	2.67	3.23	bloated	
.4			17	2.63	3.18	refired	
1088.1	1725	2	<1	3.23	3.24		glass
.2			<1	3.21	3.22	refired	glass
1089.1	1725	2	1	2.70	2.72		glass
.2			1	2.71	2.73	refired	glass
1090.1	1725	2	1	2.96	2.98		glass
.2			1	2.83	2.91	refired	glass
1091.1	1725	2					
.2							

TABLE 2

SAMPLE FABRICATION AND TEST DATA

Sample Number	Standard Pressing Conditions Yes	Standard Pressing Conditions No	Firing Conditions Max Temp (°C)	Firing Conditions Time (hrs)	Firing Weight Loss (%)	Apparent Porosity (%)	Bulk Density (g/cc)	Specific Gravity (g/cc)	Heat Treatment Atm	Heat Treatment Temp (°C)	Heat Treatment Time (hrs)	Surface Finish	Flexural Strength (ksi)	Flexural Strength (mPa)	Flexural Strength (avg mPa)	Additional Tests
1103.1						0.4	3.25	3.26				Linde A				1400° Oxidation
.2	✓		1760	2		0.3	3.28	3.29				Linde A				1300° Oxidation
.3						0.2	3.24	3.24								
.4						0.4	3.22	3.23								
1104.1						0.5	3.12	3.13				Linde A				1400° Oxidation
.2	✓		1760	2		0.6	3.11	3.13				Linde A				1300° Oxidation
.3						0.6	3.11	3.12								
.4						0.8	3.12	3.14								
.5						0.0	3.29	3.29								
.6	✓		1680	2		0.0	3.26	3.26								
.7						0.0	3.28	3.28								
.8						0.0	3.26	3.26								
1105.1						0.2	3.21	3.22				Linde A				1400° Oxidation
.2	✓					0.3	3.21	3.22				Linde A				1300° Oxidation
.3			1760	2		0.7	3.23	3.25								
.4						0.4	3.20	3.21				Linde A				Low Temperature Oxidat
.5																
.6													38.4	265		
.7	✓		1760	2					air	1300	100	240	48.1	332		
.8												Grit	57.7	398	329	
.9													44.5	307		
.10													49.5	341		
.11													50.6	349		
.12												240	60.2	415		
.13	✓		1760	2								Grit	34.4	237	331	
.14													41.7	287		
.15													53.0	366		
.16													33.5	231		
.17													27.5	190		
.18	✓		1760	2					air	1370	100	240	35.9	247	232	
.19												Grit	28.7	198		
.20													42.8	295		
.21						0.0	3.24	3.24					45.2	311		
.22	✓		1760	2		0.0	3.22	3.22				Linde A	52.7	363	331	
.23						0.3	3.21	3.21					46.4	320		
.24																1370° Creep

Table 2

Sample Fabrication and Test Data

Sample Number	Standard Pressing Conditions Yes	Standard Pressing Conditions No	Firing Conditions Max Temp (°C)	Firing Conditions Time (hrs)	Firing Weight Loss (%)	Apparent Porosity (%)	Bulk Density (g/cc)	Specific Gravity (g/cc)	Heat Treatment Atm	Heat Treatment Temp (°C)	Heat Treatment Time (hrs)	Surface Finish	Flexural Strength (ksi)	Flexural Strength (mPa)	Flexural Strength (avg mPa)	Additional Tests
1111.1	✓		1760	2	1.54	0.0	3.40	3.40								1400° Oxidation
.2						0.7	3.37	3.35								
.3					1.48	0.0	3.37	3.37								
1112.1																
.2	✓				3.78	0.0	3.07	3.07								1400° Oxidation
.3			1760	2		0.0	3.08	3.08								
.4					3.82	0.0	3.09	3.09								
1113.1	✓		1760	2												1400° Oxidation
1114.1																
.2	✓		1760	2												
.3					1.67	0.0	3.19	3.19								1400° Oxidation
.4					1.57	0.0	3.19	3.19								
1115.1					0.93							Linde A	38	259		
.2	✓		1760	2	0.80	0.0	3.09	3.09								1400° Oxidation
.3					0.70	0.0	3.11	3.11					48	327		
.4					1.12											
.5	✓					0.0	3.01	3.01								1000° Oxidation
.6			1760	2		0.0	3.08	3.08								
.7						0.0	3.07	3.07								
.8	✓		1760	2		0.0	3.04	3.04					35	240		
.9						0.0	3.17	3.17	air	1370	100	240	26	181		
.10						0.0	3.11	3.11				grit	25	171		
1115A.1					0.92	0	3.13	3.13				Linde A	34	235		
.2																
.3		✓														1400° Oxidation
.4		Binder	1760	2	1.12	0.0	3.15	3.15					41	284		
.5						0.3	3.19	3.20								1000° Oxidation
.6						0.0	3.17	3.17								
1116.1						0.1	3.25	3.25								1400° Oxidation
.2						0.1	3.24	3.24								
.3	✓		1760	2		0.1	3.29	3.29								
.4						0.0	3.25	3.25								1000° Oxidation
1116A.1	✓		1760	2		28.5	2.32	3.25								
.2						28.2	2.32	3.24								
.3	✓				11.8											
.4			1760	5	12.5											
1116B.1	✓		1760	2		14.4	2.64	3.08								
.2						14.6	2.62	3.07								
.3			1760	5	18.6	20.0	2.59	3.11								
.4					18.4	21.7	2.59	3.15								
.5			1700	12		32.1	2.24	3.30				As Fired				1400 Oxidation
.6																
.7						32.5	2.22	3.28								
1116C.1		✓	1700	5	12.3	10.9	2.69	3.02								
.2		Binder			13.0	13.5	2.67	3.09								
1117.1					5.35											1400° Oxidation
.2		✓	1760	4	4.60	0.1	3.11	3.11				Linde A	50	342		
.3		Binder			4.99	0.0	3.10	3.10								
.4						0.0	3.11	3.11								
1118.1	✓				1.25	43.3	1.87	3.30								
.2			1760	4	1.25	43.1	1.88	3.30								
.3					1.42	42.6	1.84	3.21								
.4					1.20	42.3	1.86	3.22								

Table 2 (Cont)

Sample Firing and Test Data

Sample Number	Firing Conditions Max Temp (°C)	Time (Hrs)	Apparent Porosity (%)	Bulk Density (g/cc)	Specific Gravity (g/cc)	Surface Finish	Flexural Strength ksi	mPa	Additional Tests
1119.1			0	3.49	3.49				1400°C Oxidation
.2	1760	2	0.03	3.44	3.44	Linde A	52.6	363	
.3			0.03	3.42	3.42	Linde A	45.7	315	
.1						Linde A	53.1	366	
1120.2	1760	2	0	3.32	3.32	Linde A	49.2	339	
.3			0	3.32	3.32				1400°C Oxidation
.1			0	3.32	3.32	As Fired			
1123.2	1760	2	0	3.32	3.32	As Fired			1400°C Oxidation
.3									
.1			0	3.35	3.35	As Fired			
1124.2	1760	2	0	3.35	3.35	As Fired			1400°C Oxidation
.3									
.1			0	3.34	3.34	As Fired			
1125.2	1760	2	0	3.33	3.33	As Fired			
.3									
.1			1.67	3.05	3.00	400 Grit			1370°C Creep
.2			2.61	3.06	2.98	As Fired			1400°C Oxidation
1126.3	1760	2				As Fired			1000°C Oxidation
.4			6.12	2.98	3.17	400 Grit	68.8	474	
.5			6.00	2.99	3.16				
.6			2.25	3.06	3.13	400 Grit	67.9	467	
.7			2.64	3.08	3.16	400 Grit	52.0	358	
1129.1			0.07	3.48	3.48	As Fired			1370°C Oxidation
.2	1760	2	0.03	3.39	3.39	As Fired			1000°C Oxidation
.3									
1130.1									
.2									
.3	1760	2	0.11	3.05	3.05				1370°C Oxidation
.4			0.20	3.05	3.05				
1131.1			0	3.32	3.32	As Fired			1400°C Oxidation
.2	1700	15	0	3.32	3.32	As Fired			1370°C Oxidation
.3			0	3.32	3.32	Linde A	92	632	
.4									
.5			0	3.25	3.25	Linde A	40	276	
.6	1700	5	0	3.25	3.25	Linde A	52	359	
.7			0	3.25	3.25	Linde A	49	341	
1132.1			.09	3.28	3.28	As Fired			1400°C Oxidation
.2	1700	5	.13	3.28	3.28	600 grit			
.3			.15	3.30	3.30	600 grit			1370°C Oxidation
1133.1						As Fired			1400°C Oxidation
.2	1700	5	0.06	3.29	3.29	600 grit	62	429	
.3			0.0	3.28	3.28	600 grit	57	393	
1134.1						As Fired			1400° Oxidation
.2	1700	5	0	3.29	3.29	600 grit	58	401	
.3			0	3.29	3.29	600 grit	67	461	
1135.1						As Fired			1400° Oxidation
.2	1700	5	0.03	3.29	3.29	600 grit			
.3			0.01	3.22	3.22	600 grit			
1136.1						As Fired			1400° Oxidation
.2	1700	5	0.08	3.38	3.38	600 grit			
.3			0.05	3.33	3.33	600 grit			

Table II

Fabrication and Test Data

Sample Numbers	Firing Conditions Temp (°C)	Time (hrs)	Bulk Density (g/cc)	Flexural Strength ksi	MPa	Additional Tests
1134.1						
.2	1700	5	3.29			1400°C oxidation
.3			3.29			
1137.1						
.2	1700	5	2.33	79	543	1400°C oxidation
.3			3.26			
.4			2.34	70	484	
1138.1						
.2	1700	5	3.42	68	468	1400°C oxidation
.3			3.44			
.4			3.35	85	585	
1139.1						
.2	1700	5	3.35	66	454	1400°C oxidation
.3			3.38	78	536	
.4						
1140.1						
.2	1700	15	3.38	60	414	1400°C oxidation
.3			3.40	84	576	
.4						
.5			3.39			1000°C oxidation
.6	1700	20	3.29			
.7			3.28			
.8			2.29			
.9				86	592	
.10	1700	10		64	440	
.11				85	584	1370°C oxidation
1141.1						
.2	1700	10	3.15			1400°C oxidation
.3			3.18			
.4			3.13			
.5			3.18			
.6	1700	10	3.23			
.7			3.24			
.8			3.14			
1142.1						
.2	1700	10	3.03			1400°C oxidation
.3			2.98			
.4						1370°C oxidation

APPENDIX D

OXIDATION DATA FOR VARIOUS TEST SAMPLES

Rate Data for Samples Oxidized in Air at Different Temperatures

1400°C

Sample Number	t (hr)	$\frac{\Delta W^2}{A^2}$ ($g^2cm^{-4} \times 10^7$)	$\frac{\Delta W^2}{A^2 t}$ ($g^2cm^{-4}\ hr^{-1} \times 10^7$)	Average Parabolic Rate Constant ($g^2cm^{-4}\ hr^{-1} \times 10^7$)
1078.1	1.0	0.86	0.86	1.54
	3.0	3.62	1.62	
	4.3	7.15	1.66	
	5.5	9.52	1.75	
	8.5	13.32	1.58	
	11.2	19.55	1.75	
	26.9	40.65	1.51	
	96.6	140.3	1.57	
1079.1	1.0	12.5	12.5	5.46
	3.0	14.6	4.86	
	4.3	25.6	5.95	
	5.5	31.8	5.78	
	8.5	34.0	4.00	
	11.2	58.4	5.21	
	26.9	85.8	3.19	
	96.6	236.2	2.40	
1080.1	1.25	168.0	134.0	134.0
1080.7	1.25	202.0	162.0	162.0
1081.6	1.0	166.0	166.0	166.0
HS 130*				0.33
		1000°C		
1078.2	65.0	62.9	0.97	0.97
1079.2	65.0	0.33	0.005	0.005
1080.2	26.0	0	0	0

*From data of Tripp and Graham

TABLE 4

WEIGHT GAIN OF SAMPLES HEATED IN AIR AT 1400°C

Sample # / time (hrs)	1085.2 ΔW/A (mg/cm^2)	1085.3 ΔW/A	1086.1 ΔW/A	1086.2 ΔW/A	1088.1 ΔW/A	1088.2 ΔW/A	1089.1 ΔW/A	1089.2 ΔW/A	1090.1 ΔW/A	1090.2 ΔW/A
1	4.38	5.57	2.04	1.65	3.53	2.84	1.29	1.30	0.90	0.70
3	4.54	5.82	2.35	2.19	3.81	3.02	1.57	1.63	1.35	1.14
10.75	4.87	6.42	2.60	3.80	4.74	4.07	1.61	2.54	2.42	2.06
23.25	7.23	8.16	2.85	4.64	5.68	4.99	3.75	3.52	3.21	2.86
47.25	8.36	10.37	3.41	5.19	7.02	6.29	4.74	4.42	4.18	3.84
59.25	9.17	10.52	3.60	5.40	7.66	6.81	5.28	4.82	4.70	4.28

Sample # Time (hrs)	1084.1 ΔW/A	1091.1 ΔW/A
1.0	0.4	
2.5		0.65
2.83	0.63	
4.25		0.76
5.75	0.91	
6.25		0.76
22.25	1.54	0.84
46.0	1.65	
58.75		1.16

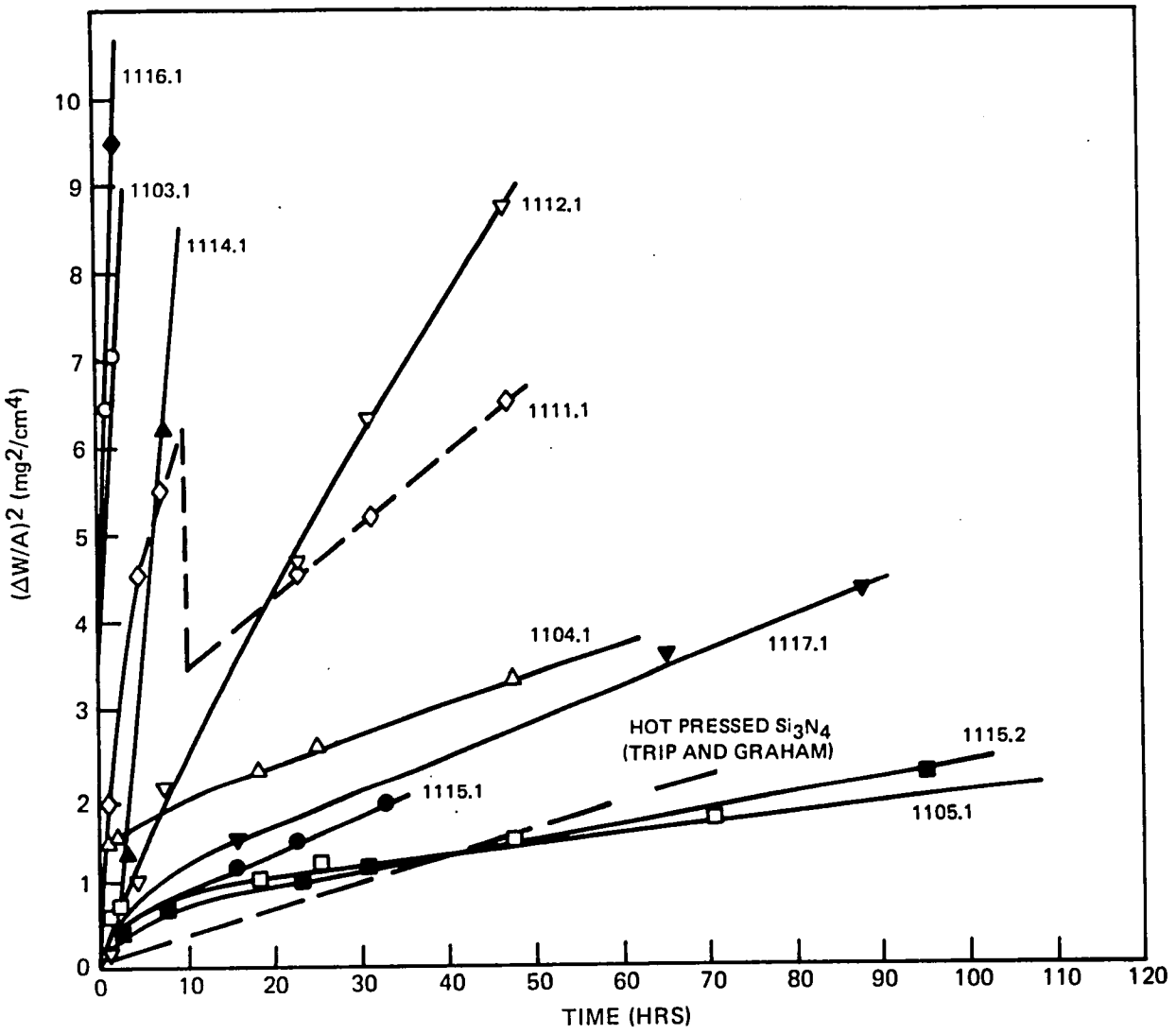

Fig. 5 Weight Gain in Air at 1400°C for Some Compositions in the YSiAlON and YSiBeON Systems

78-09-153-2

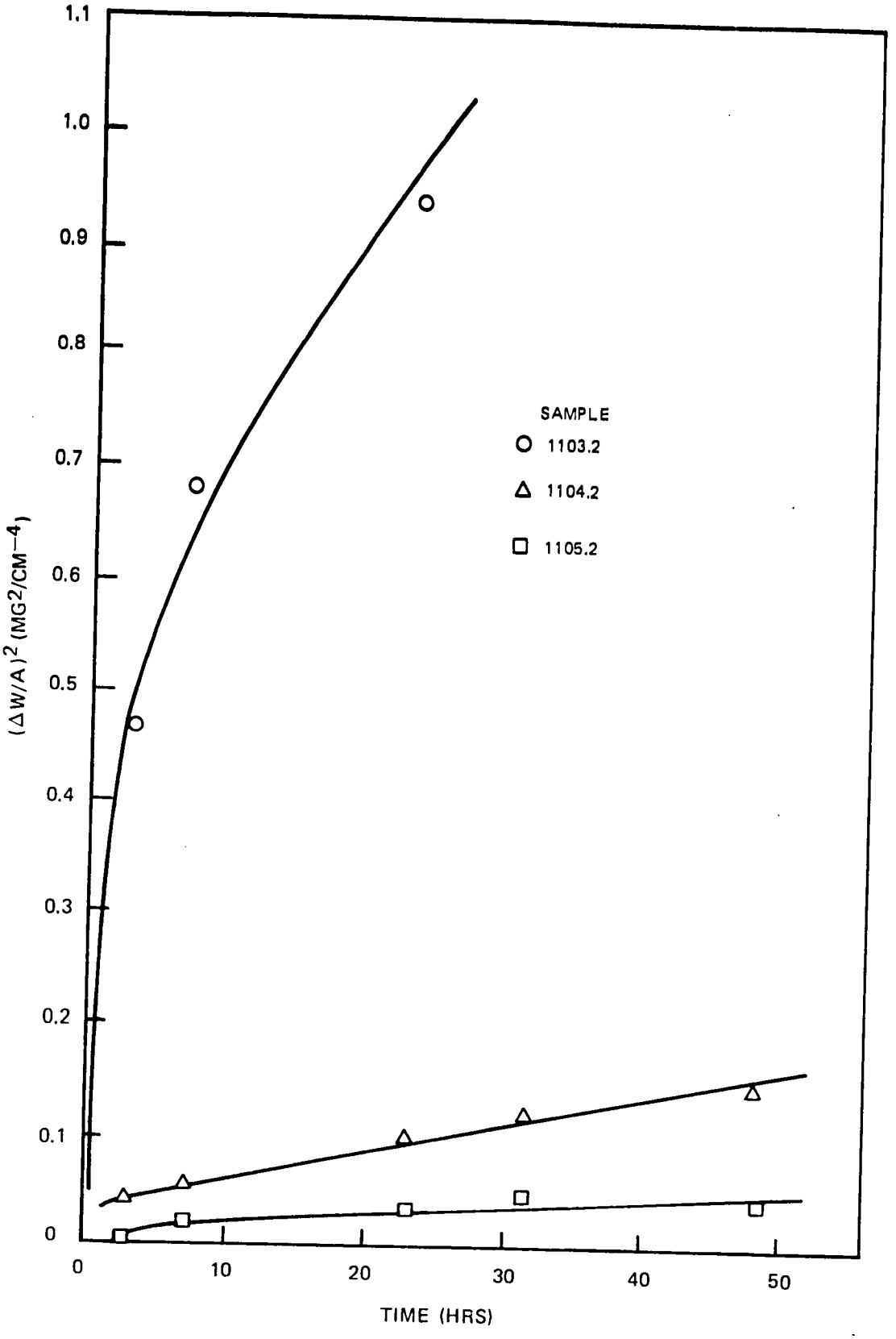

Fig. 6 Weight Gain in Air at 1300°C for Compositions in the System YSiALON (Parabolic Plot)

78-07-41-2

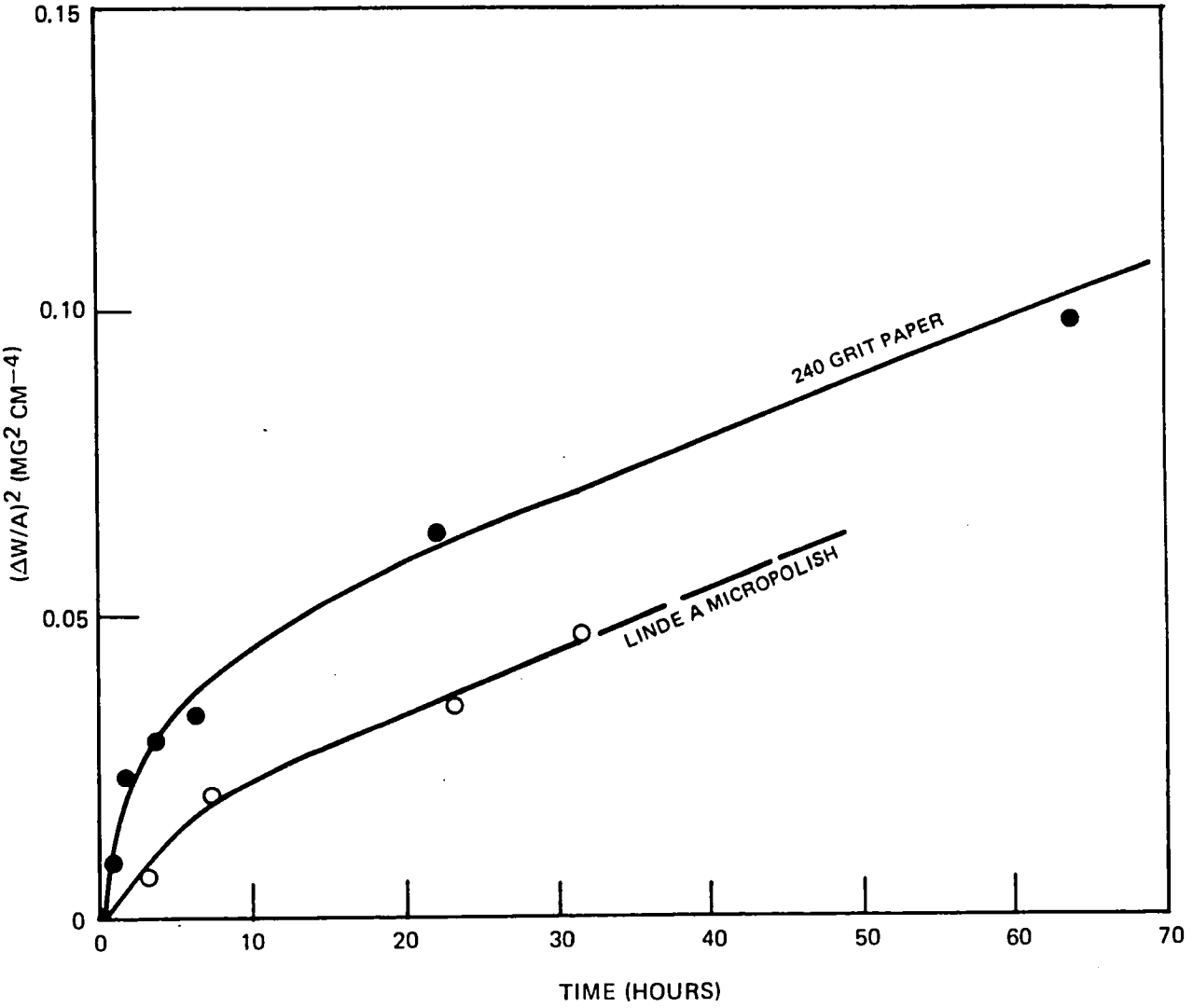

Fig. 7 Weight Gain in Air at 1300°C for 1105 Sample Having Different Surface Finishes

78-08-5-1

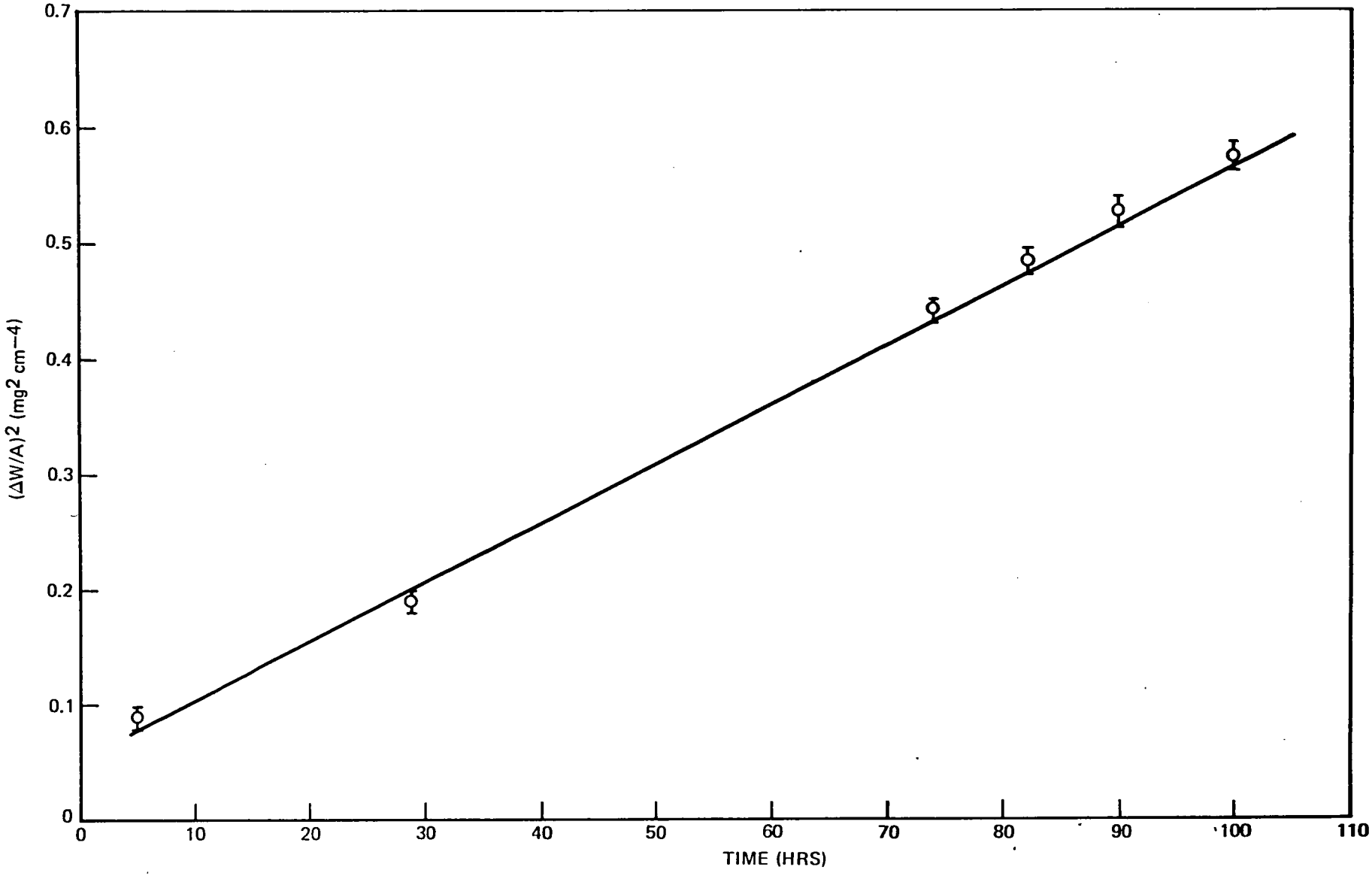

Fig. 8 Weight Gain in Air at 1370°C of Samples of Composition 1105

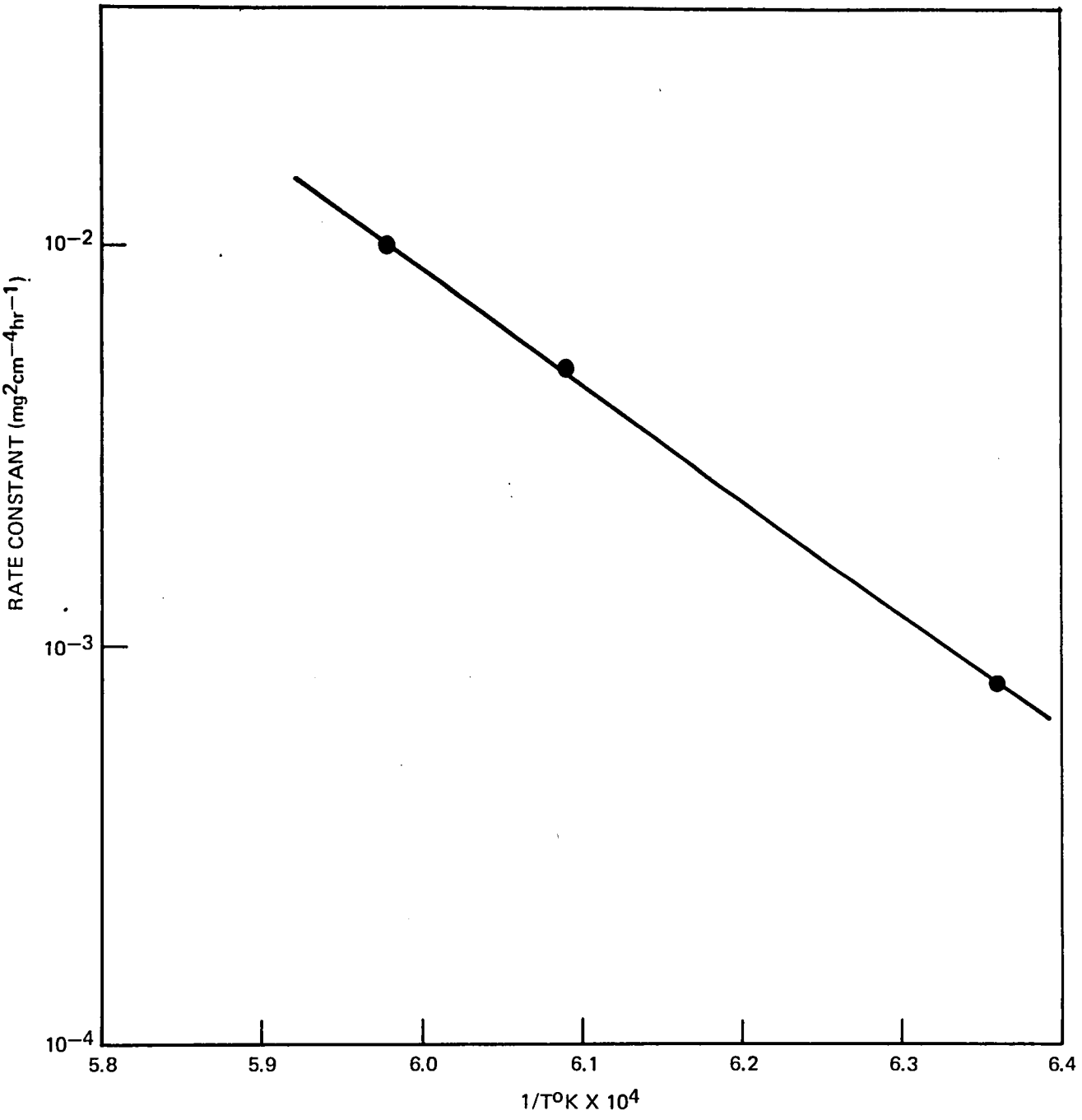

Fig. 9 Temperature Dependance of Oxidation Rate for Composition 1105 Samples

78-09-153-4

TABLE 4

Parabolic Oxidation Rates in Air at 1400°C and Principle Components of Oxide Scales of Samples of Different Composition

Composition	Oxidation Rate Constant $(mg^2 cm^{-4} hr^{-1}) \times 10^2$	Principle Components of Scale
1103	100	glass, cristobalite
1104	3.5	mullite
1105	1.0	mullite
1111	8.3	glass, cristobalite, $Y_2Si_2O_7$
1112	15.6	glass, cristobalite $Y_2Si_2O_7$
1113	4.0	glass, cristobalite
1114	100	glass, cristobalite
1115	1.6	mullite
1116	100	glass, cristobalite
1117	4.0	glass, cristobalite
HS130	2.7*	glass, cristobalite

*Data of Tripp and Graham.

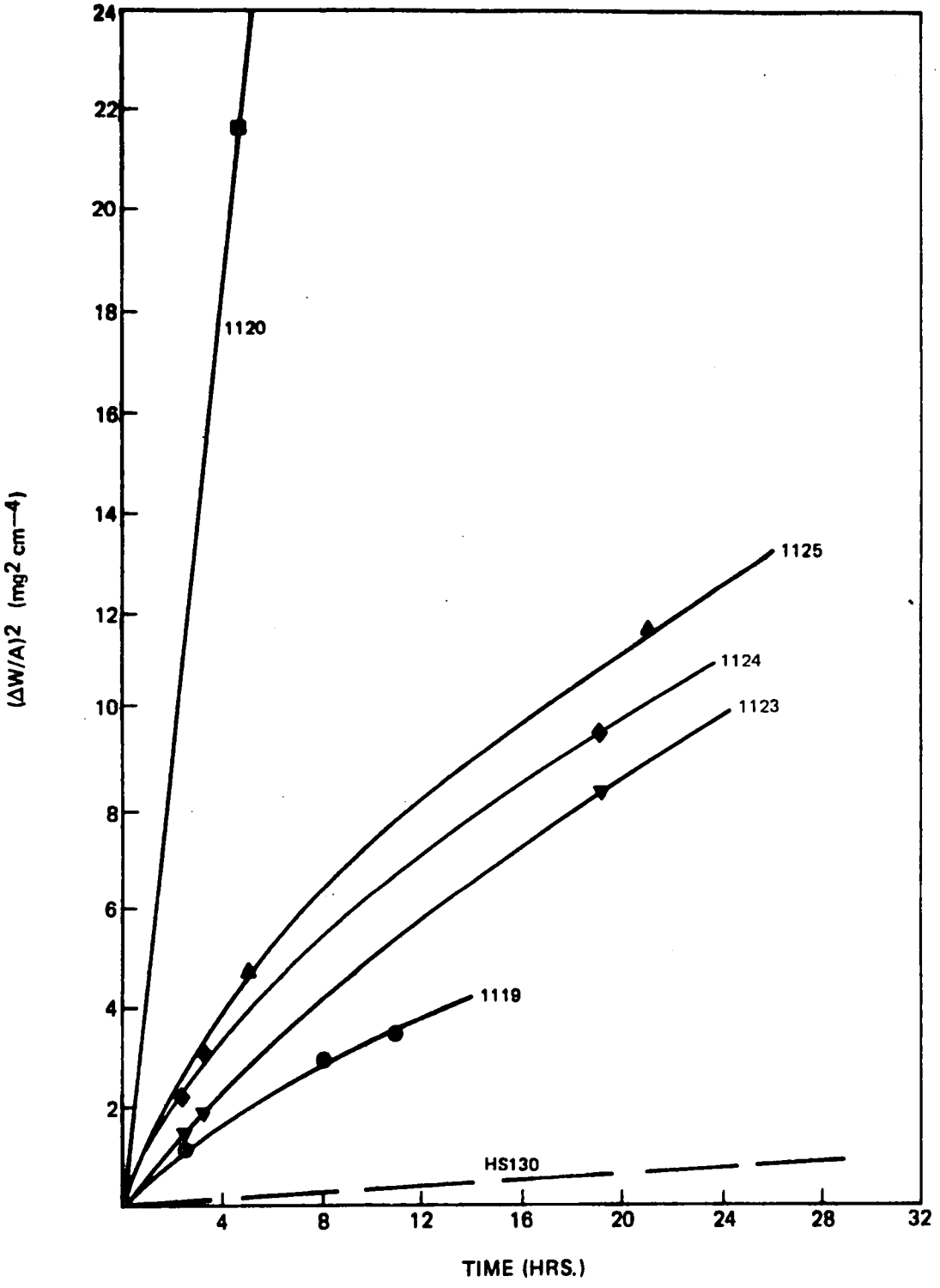

Fig. 3 1400°C Oxidation Curves for Some Compositions in the CeSiON, CeSiAlON, and CeSiBeON Systems

78-11-45-1

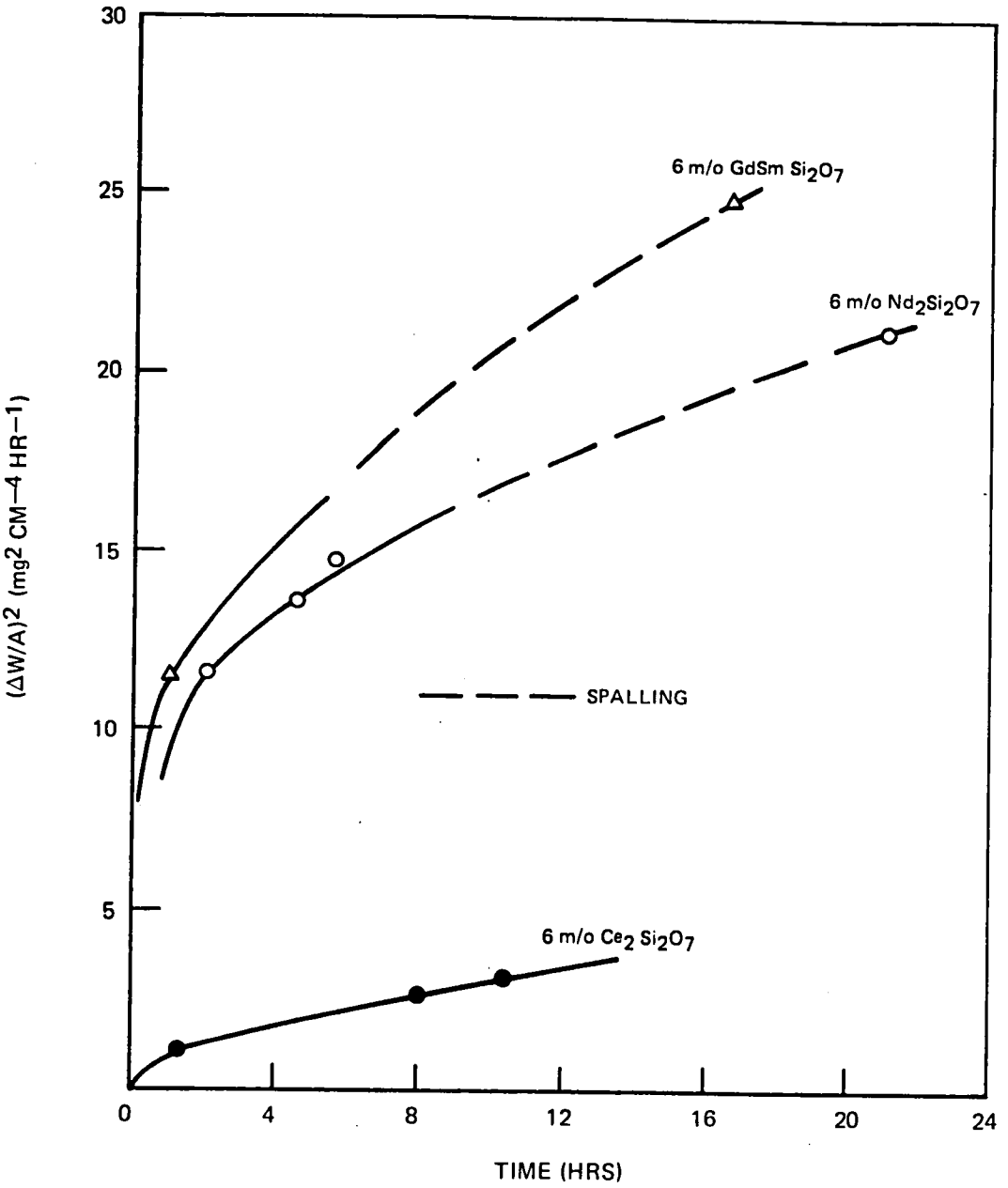

Fig. 4 1400°C Oxidation Curves for Samples 94 m/o Si_3N_4 6 m/o R_2 Si_2O_7

78–12–31–3

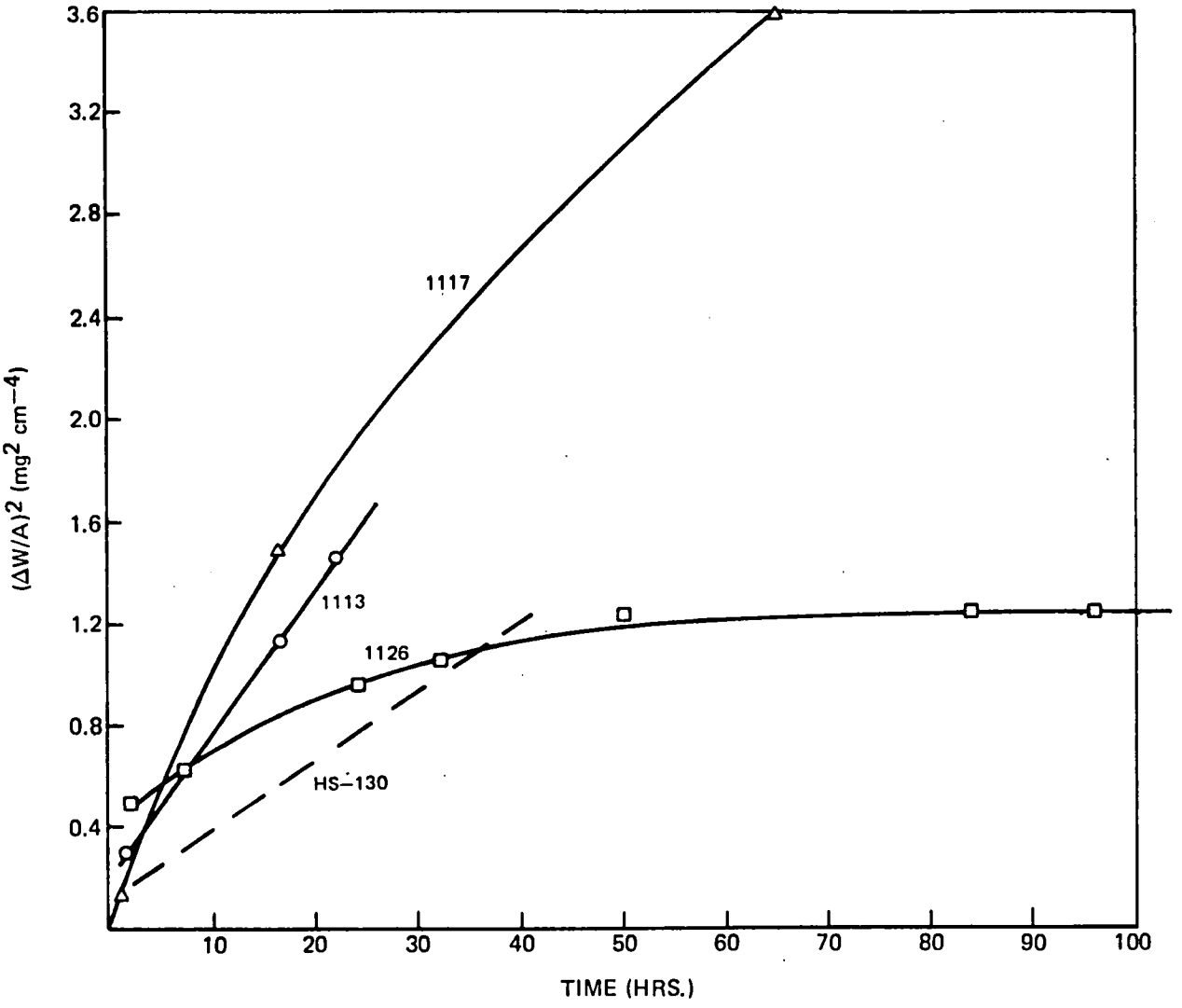

Fig. 5 1400°C Oxidation Curves for Some Compositions in the YSiBeON System

78-11-45-2

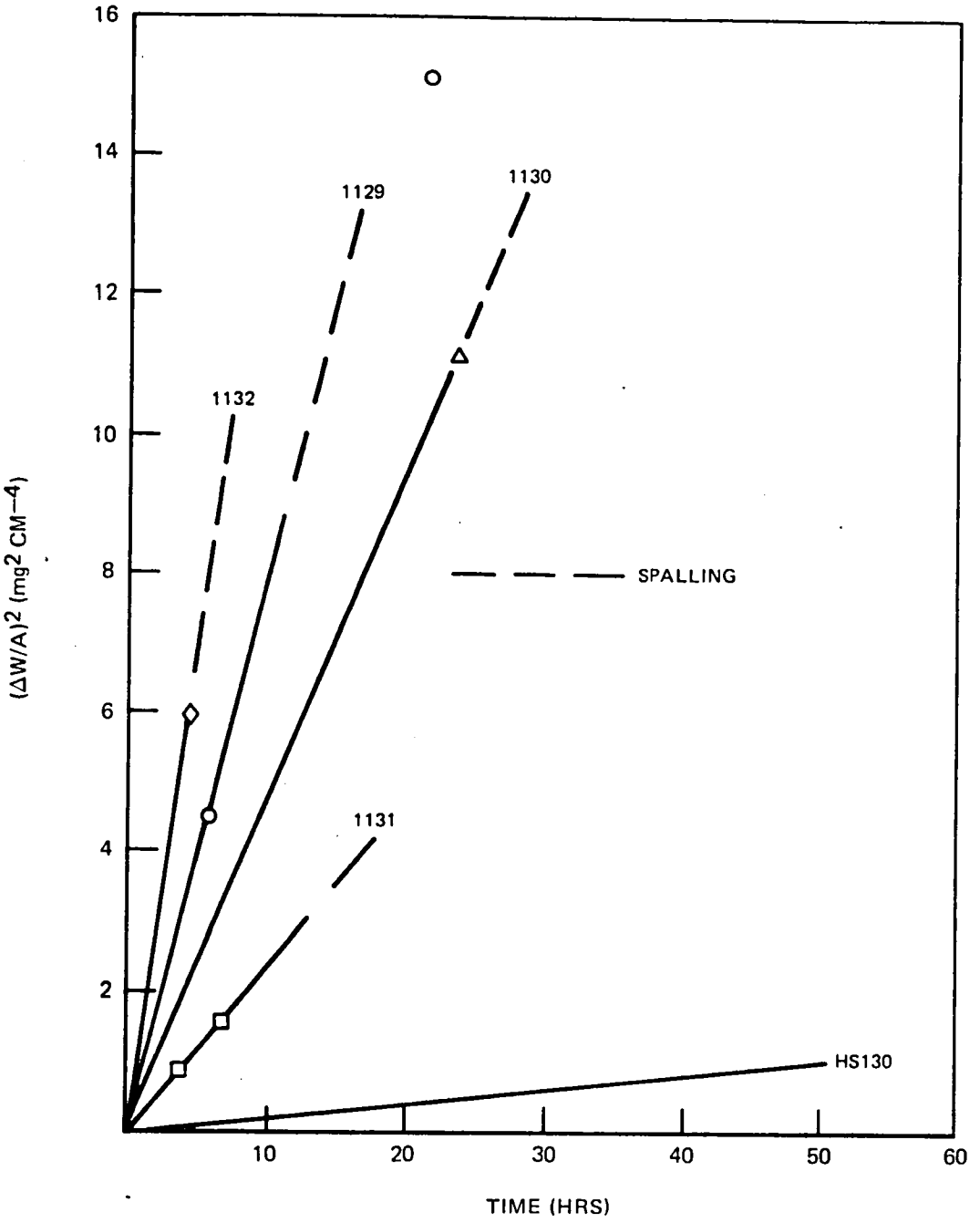

Fig. 6 1370°C Oxidation Curves for Some Compositions in the Y Ce Si on System

78-12-31-1

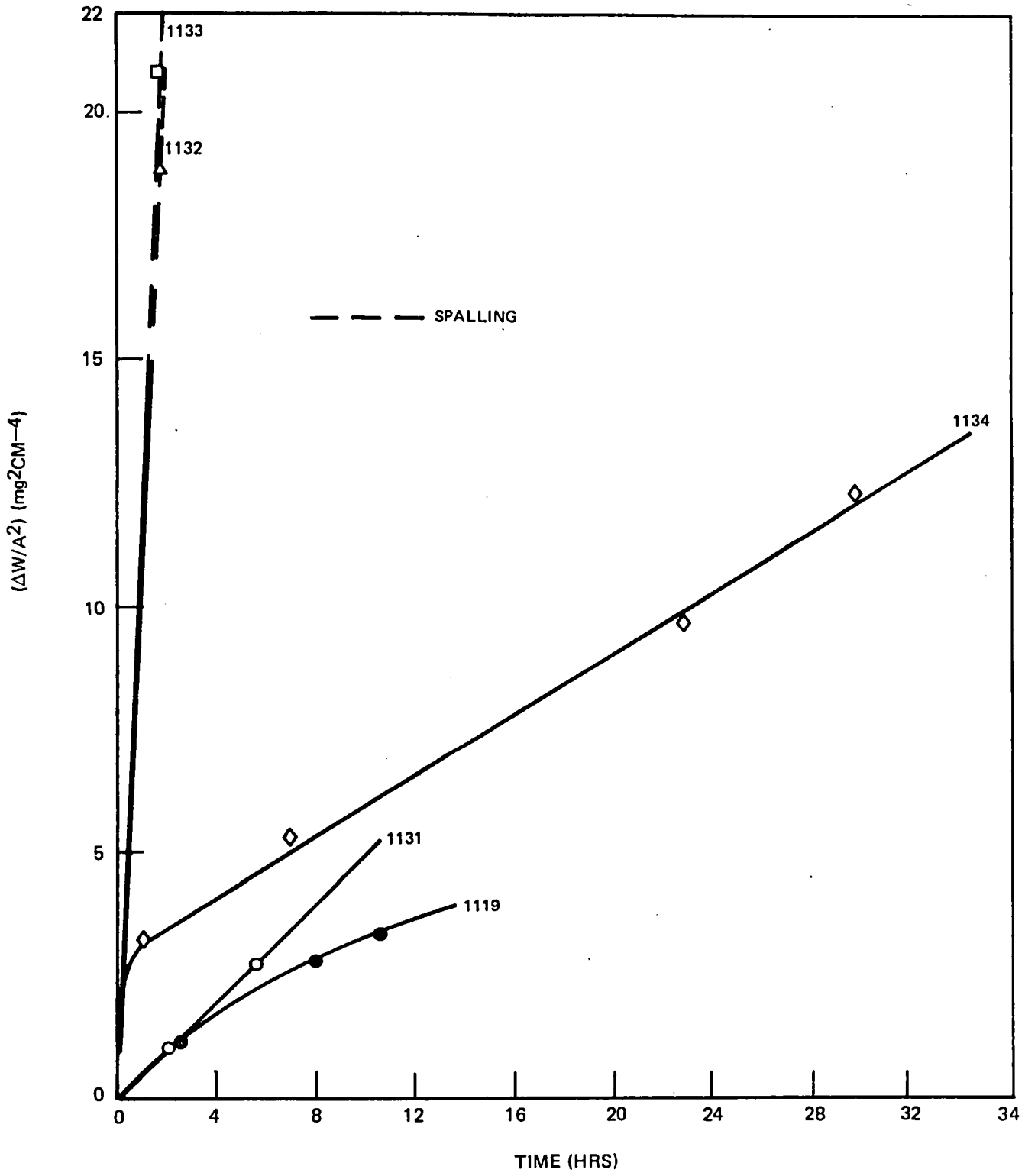

Fig. 7 1400°C Oxidation Curve for Some Compositions in its Y Ce Si ON System

78-12-31-4

APPENDIX E - SOLID-LIQUID EQUILIBRIA IN THE Y-Si-O-N AND Nd-Si-O-N SYSTEMS

A. Y-Si-O-N System

In order to obtain a better understanding of the interactions of the melts with Si_3N_4, the melting behavior of ternary compounds in the systems Si_3N_4 - SiO_2 - Y_2O_3 and Si_3N_4-SiO_2-Nd_2O_3 was investigated. This led to a systematic investigation of liquid-solid equilibria along the join Y_2SiO_5 - $Y_2Si_3O_3N_4$ in the former system. In these investigations, compositions were prepared from raw materials in ten or twenty gram batches by grinding under acetone until dry, pressing into pellets, and firing to 1650° for two hours. The fired pellets were examined for evidence of melting, crushed to pass 200 mesh screen, and x-ray diffraction patterns obtained. Portions of the crushed powder were then repelletized and heated to high temperature in small boron nitride crucibles. When there was evidence of melting, the recrystallized material was cut into two pieces. One piece was examined metallographically and the other was crushed and x-rayed. Compositions investigated in this fashion, and the results, are presented in Table E1. Micrographs of polished sections etched with HF of recrystallized samples in the Y_2O_3 - SiO_2 - Si_3N_4 system are shown in Figs. E2 through E10. From these data a tentative phase diagram for the joint Y_2SiO_5-$Y_2Si_3O_3N_4$ is constructed and presented in Fig. 29 in the main section of the report. Aspects of the proposed phase diagram are discussed in terms of the metallographic and x-ray data below. Composition points refer to Fig. E1.

1. Composition Point 13 (5 m/o $Y_2Si_3O_3N_4$)

Metallography and x-ray results show this composition to be solid at 1700°C and a mixture of primary crystals of Y_2SiO_5 (X_2 phase) and liquid (which crystallized to H phase) at 1750°C.

2. Compositions Points 14-17 (10 through 30 m/o $Y_2SiO_3N_4$)

Composition 14 showed no evidence of melting at 1700°C, but appeared to have been all liquid at 1750°C. The micrograph of the 10 m/o $Y_2Si_3O_3N_4$ composition cooled from 1750°C (Fig. E3) appears to be very nearly single phase with just a trace of what appears to be a eutectic microstructure at triple points between primary H phase cyrstals. Figure E4 shows large primary crystals of H phase and eutectic matrix indicating that composition 15 m/o $Y_2Si_3O_3N_4$ cooled through a two phase region. Not shown in Fig. E4 are occasional small pockets of material that, on the basis of its etching characteristics, appears to be residual glass. Figure E5 shows the 20 m/o $Y_2Si_3O_3N_4$ composition cooled from 1750°C, and again shows the presence of large primary H phase cyrstals, and, in areas of the sample, a eutectic like matrix. In other areas of the sample, however, the matrix phase appears quite different, as though residual glass has been etched to disclose

crystalline dendrites. Figure E6 shows small primary H phase crystals in a glassy matrix for the 30 m/o $Y_2Si_3O_3N_4$ composition cooled from 1700°C. The matrix phase has taken on many colors ranging from purples and blues through yellows and brown. These colors are probably interference colors resulting from films which formed on the glass as a result of HF etch. The primary H phase crystals were the only phase detected by x-rays in this sample.

3. Composition Points 18 and 19 (50 and 75 m/o $Y_2Si_3O_3N_4$)

Composition point 18 was K phase at 1650°C, but crystallized to mostly $Y_2Si_3O_3N_4$ and H phase when cooled from 1750, indicated either that K phase melts incongruently to $Y_2Si_3O_3N_4$ and liquid, or perhaps that K phase melts to two liquids. As in the case of sample 1007B (20 m/o $Y_2Si_3O_3N_4$, Fig. E5), the matrix phase appeared to differ in different regions of the sample. There appears to be little contrast between primary crystals and matrix phases in one area, while the matrix phase shows strong interference colors in another region, as shown in Fig. E7. This sample was repolished and re-etched with the same result, and it seems resonably sure that the matrix phase did not crystallize in certain regions during cool down of the sample from 1750°C. Sample 19 (75 m/o $Y_2Si_3O_3N_4$) cooled from 1700°C, shown in Fig. E8, contains both $Y_2Si_3O_3N_4$ crystals which were growing, and small rounded crystals of K phase which were dissolving in a liquid which has cooled to a glass. Clearly then, the K phase melts incongruently at very nearly 1700°C.

4. Composition Point 10 (J Phase)

This composition point appeared single phase to x-rays and metallographic examination at all temperatures investigated. It is solid at 1750°C.

B. Nd-Si-O-N System

The generally lower liquidus temperatures in the Nd_2O_3-SiO_2 system compared to those in the Y_2O_3-SiO_2 system suggested that ternary liquids in the Nd_2O_3 SiO_2-Si_3N_4 (or liquids involving mixtures of Nd_2O_3 and Y_2O_3) would be more reactive than the analogous Y_2O_3 liquids. Only the composition points 16 and 18 (Fig. E1) were investigated in the neodynium system. Data for these points are presented in Table E1. E-ray data for the neodynium H and K phases are presented in Tables E2 and E3. Micrographs are shown in Figs. E10 and E11. As was the case with composition point 16 in the yttria system, so in the neodymia system, large areas of matrix liquid failed to crystallize on cooling from 1750°C and remained as glass at room temperature. The amount of glass retained was considerably greater in the neodymia case than in that of yttria. Composition 18 (that of K phase) cooled from 1750 and 1800°C contained no primary cyrstals, but exhibited dendritic structures. The x-ray pattern showed poorly crystallized H phase and $Nd_2Si_3O_3N_4$ which is probably, but not necessarily, indicative of incongruency.

APPENDIX E

TABLE E1

METALLOGRAPHIC AND X-RAY DATA FOR TERNARY COMPOSITIONS

Sample Number	Batch Composition (grams) Si_3N_4	SiO_2	Y_2O_3	Other	Composition Point (Fig. 4)	Firing Conditions T °C ± 30	Time (hrs)	Visual and/or Metallographic Observation	Phases Observed by X-ray Diffraction(1) β	H	J	K	M	Other
1007A	1.858	3.184	14.956		16	1650	2	Solid		s		w		
1007B	1.858	3.184	14.956		16	1750	2	Melted		s		w		
1007C	1.858	3.184	14.956		16	1850	0.5	Melted			m	m		s Y_2SiO_5
1008	4.304	1.844	13.852		18	1650	2	Solid			w	s		
1008A	4.304	1.844	13.852		18	1850	0.5	Melted		s	w		m	
1048	4.304	1.844	13.852		18	1750	0.5	Melted		m	w		s	
1024	2.542	1.089	16.369		11	1650	2.5	Solid			s			
1039	2.542	1.089	16.369		11	1850	0.5	Melted			s			
1065	2.542	1.089	16.369		11	1750	0.5	Solid			s			
1029	7.664		12.336		12	1650	2.5	Solid	w		s		m	YSi
1040	7.664		12.336		12	1850	0.5	Melted, partially reduced						
1046	7.664		12.336		12	1650	2.5	Solid	m		m		s	
1066	7.664		12.336		12	1750	0.5	Solid					s	
1071A	1.052	2.550	11.29		15	1750	0.5	Melted		s				
1072A	0.701	2.705	11.29		14	1750	0.5	Melted						
1072B	0.701	2.705	11.29		14	1650	1.0	Solid						
1072C	0.701	2.705	11.29		14	1700	1.0	Solid		s				
1073A	0.351	2.855	11.29		13	1750	0.5	Partial Melting		w				w Y_2SiO_5
1074A	1.402	2.404	11.29		17	1750	1.0	Melted		s				Weak undecipherable
1074B	1.402	2.404	11.29		17	1700	1.0	Partial Melting	s					
1078A	5.258	0.751	11.290		19	1700	1.0	Partial Melting		m		m		
1078B	5.258	0.751	11.290		19	1750	0.5	Partial Melting		w			s	
1033	1.606	0.688		Nd_2O_3 7.706	18	1650	2.5	Solid		w(2)			s(3)	
1041	1.606	0.688		1033	18	1850	0.5	Melted, dendites		m			w	m YSi
1047	1.606	0.688		1033	18	1750	0.5	Melted, dendites		m			w	
1056	1.403	2.404		Nd_2O_3 16.825	16	1650	2.0	Partial Melting		s		w		
1057	1.403	2.404		1056	16	1750	0.5	Melted		s		w		

(1) Letters s, m, w indicate: Strong, medium and weak intensity pattern.
the letters β, H, J, K and M are: β'Si_3N_4, N - apatite, N - YAM, N - α wollastonite, M - N - melilite

(2) the x-ray diffraction pattern for the neodymium H phase is given in Table 4.

(3) the x-ray diffraction pattern for the neodymium K phase is given in Table 5.

TABLE E2

X-RAY DIFFRACTION PATTERN FOR
NEODYMIUM H PHASE

d(Å)	I/I_o
4.21	10
4.04	8
3.65	8
3.30	20
3.17	20
2.90	100
2.80	20
2.32	5
2.19	5
2.09	8
2.00	20
1.940	10
1.901	20
1.847	8
1.816	20
1.799	20
1.783	10

TABLE E3

X-RAY DIFFRACTION PATTERN FOR
NEODYMIUM K PHASE

d(Å)	I/I_o
4.72	15
3.66	30
3.40	5
3.20	10
2.88	100
2.36	10
2.097	20
1.975	20
1.913	20

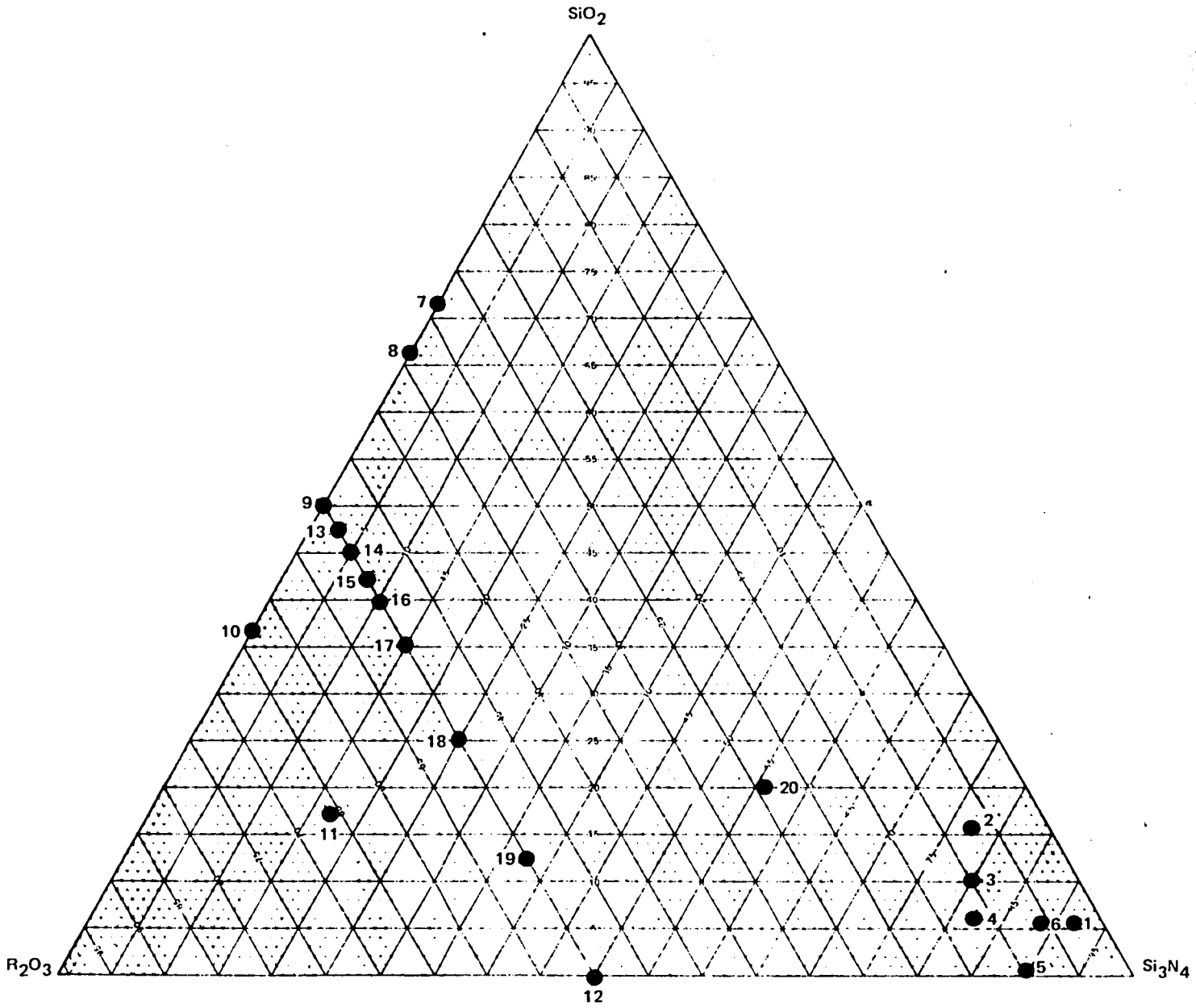

Figure E1 Compositions Investigated

TOP OF SAMPLE

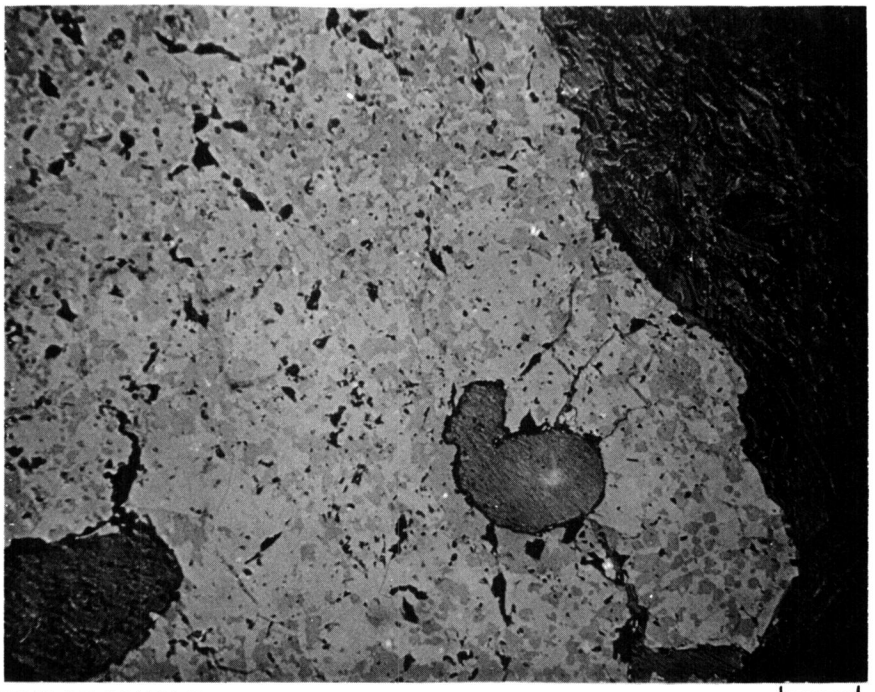

BOTTOM OF SAMPLE

50μ

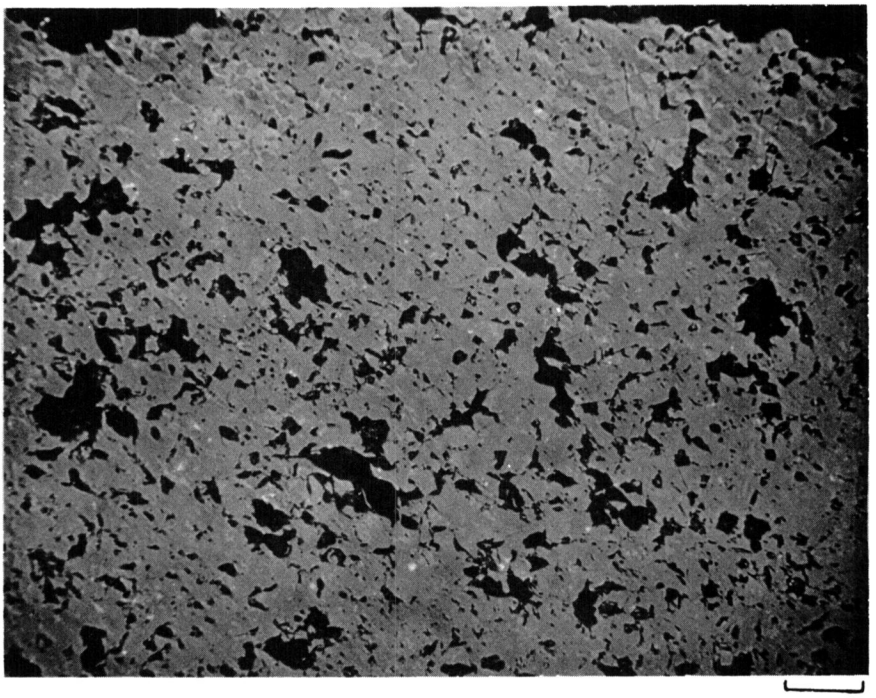

50μ

Figure E2 Etched Sections of Sample 1073A (5 m/o $Y_2Si_3O_3N_4$ Cooled From **1750°C**)

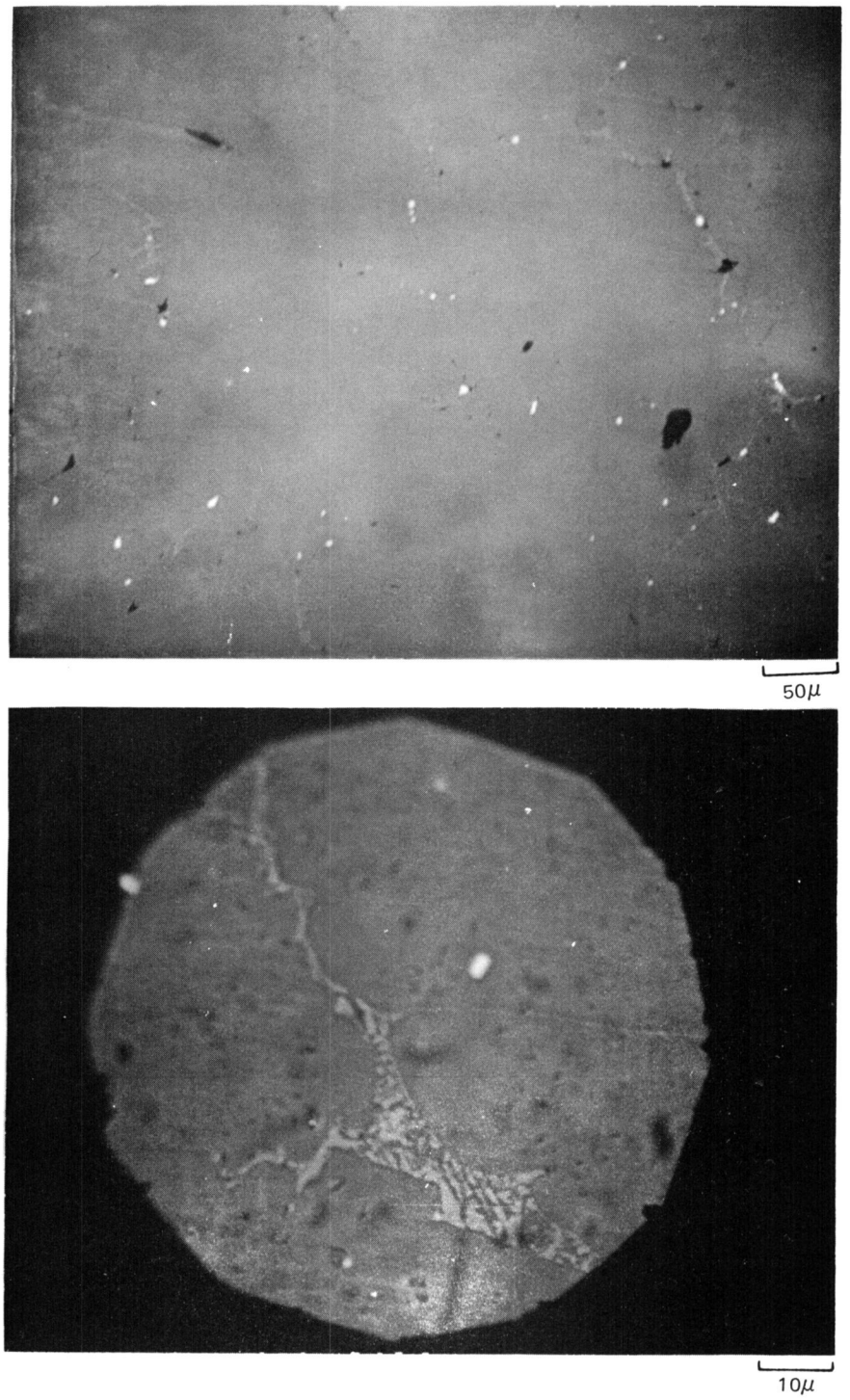

Figure E3 Etched Sections of Sample 1072A (10 m/o $Y_2Si_3O_3N_4$ Cooled From 1750°C

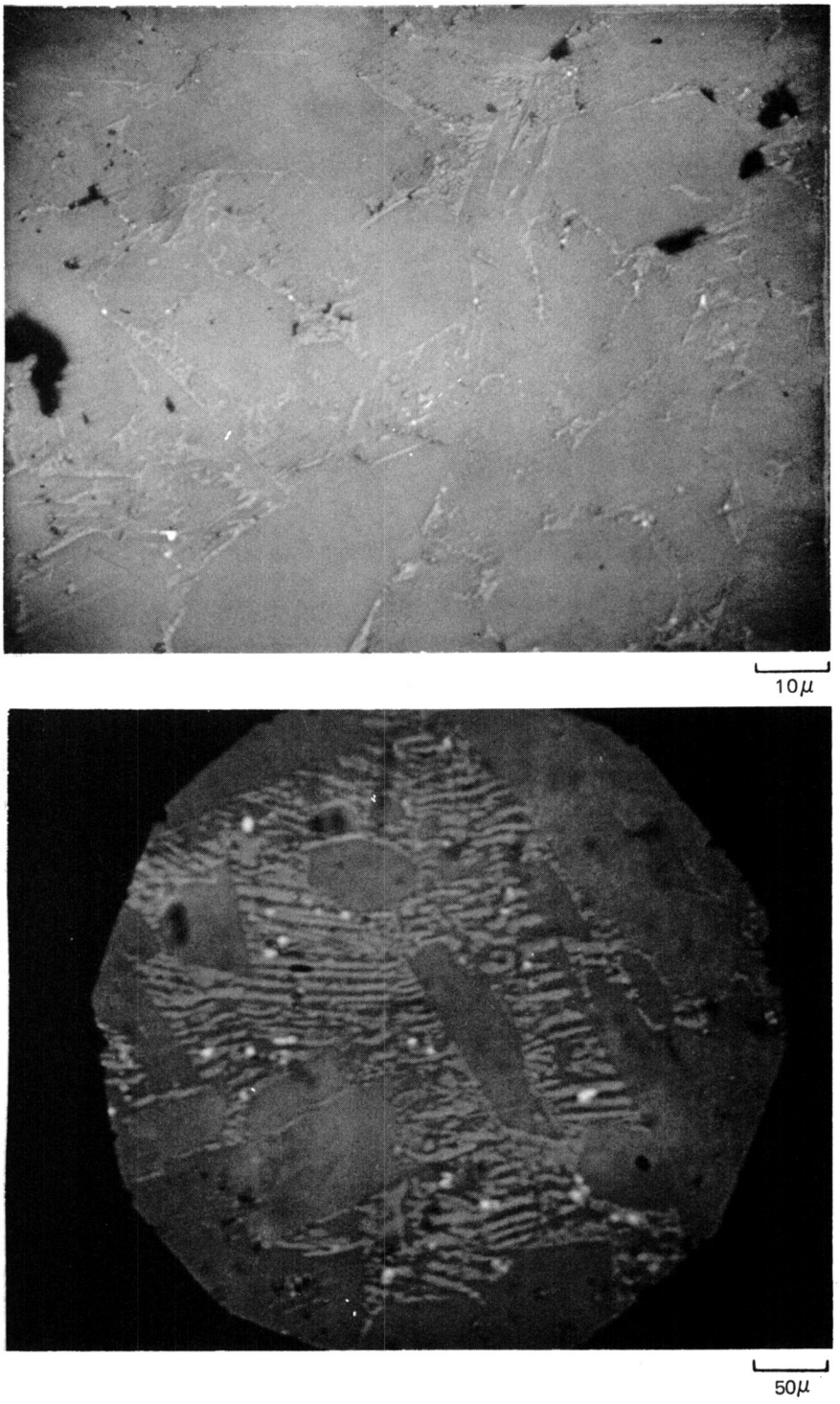

Figure E4 Etched Sections of Sample 1071 (15 m/o $Y_2Si_3O_3N_4$ Cooled From **1750°C**)

77–12–44–11

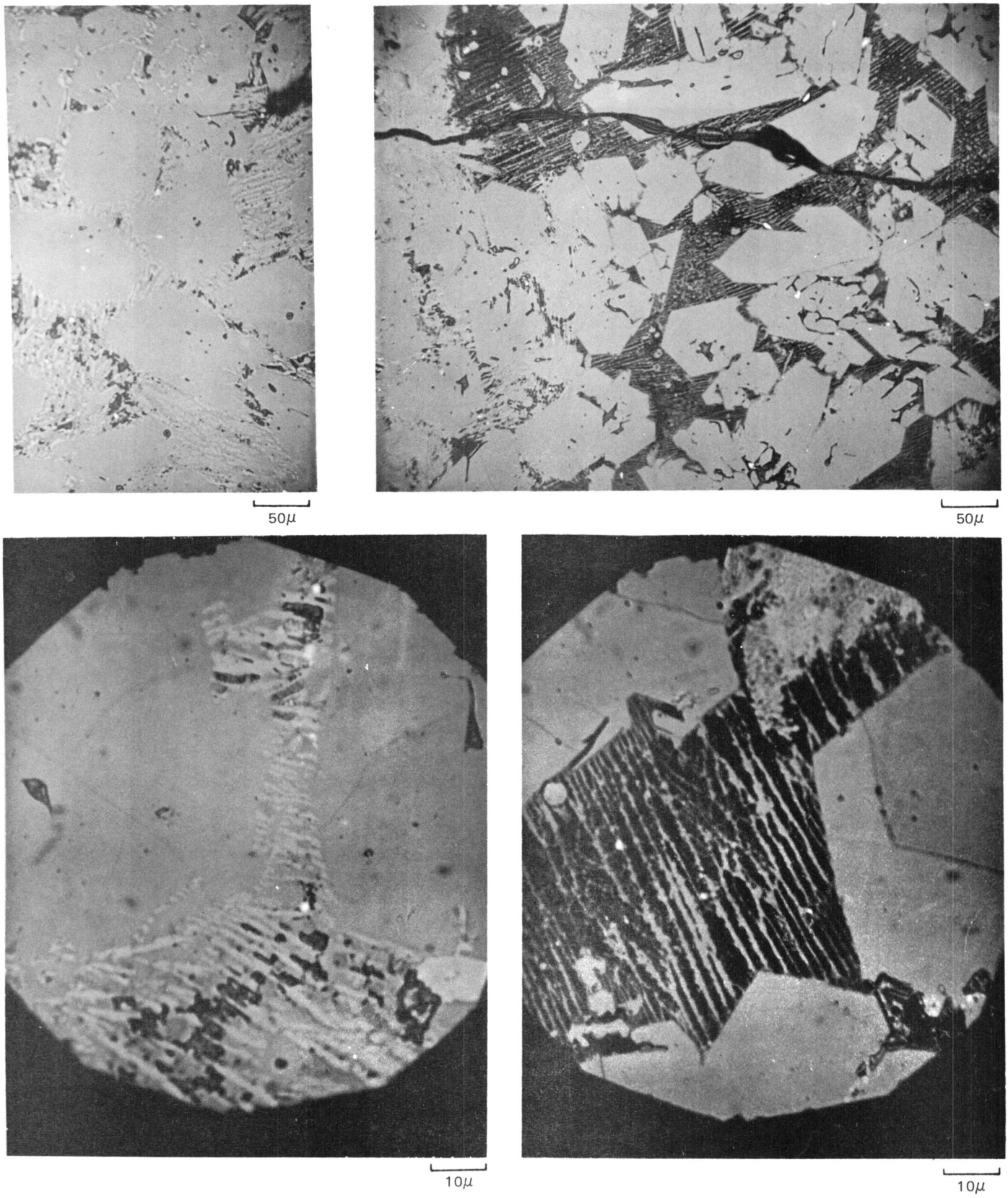

Figure E5 Etched Sections of Sample 1007B (20 m/o $Y_2Si_3O_3N_4$ Cooled From 1750°C)

77–12–44–10

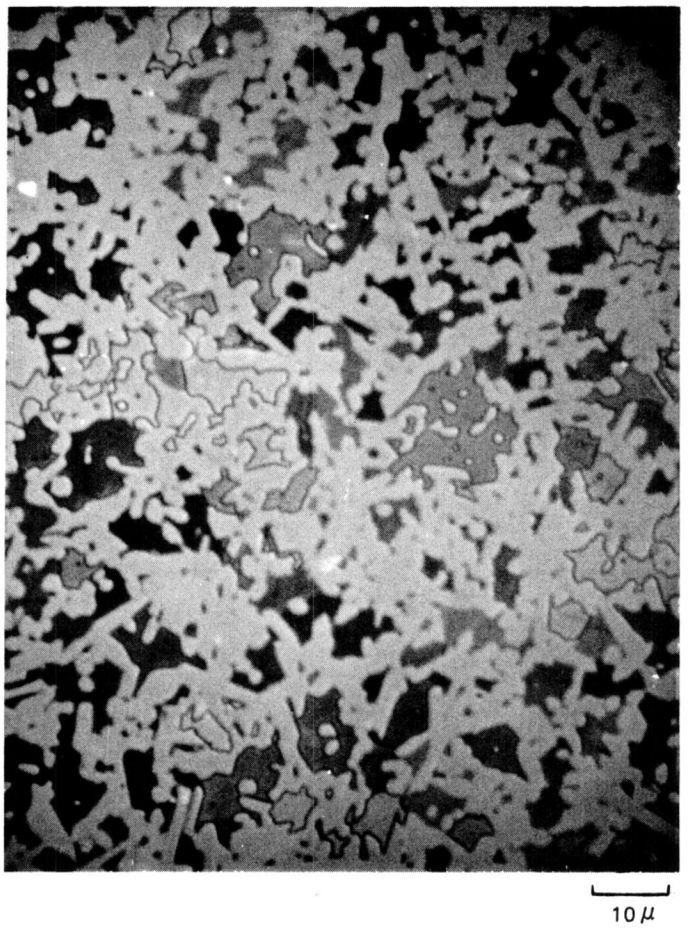

Figure E6 Etched Section of Sample 1074 B (30 w/o $Y_2Si_3O_3N_4$ Cooled From 1700°C

77–12–44–17

A. LOW CONTRAST REGION (ALL CRYSTALLINE 2)

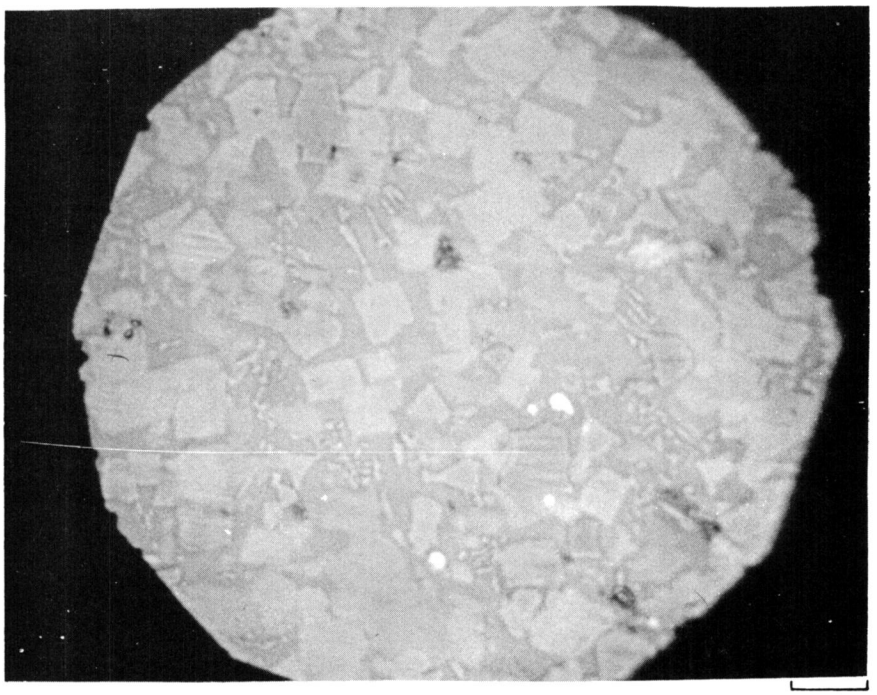

10μ

B. (HIGH CONTRAST REGION (GLASSY MATRIX 2)

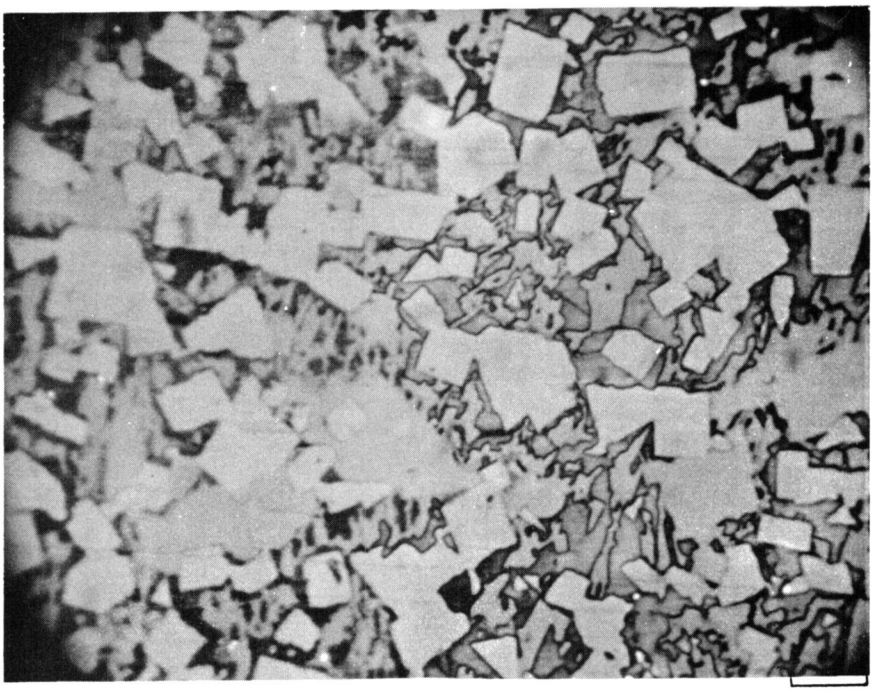

10μ

Figure E7 Etched Sections of Sample 1048 (50 m/o $Y_2Si_3O_3N_4$) Cooled From **1750°C**

77–12–44–9

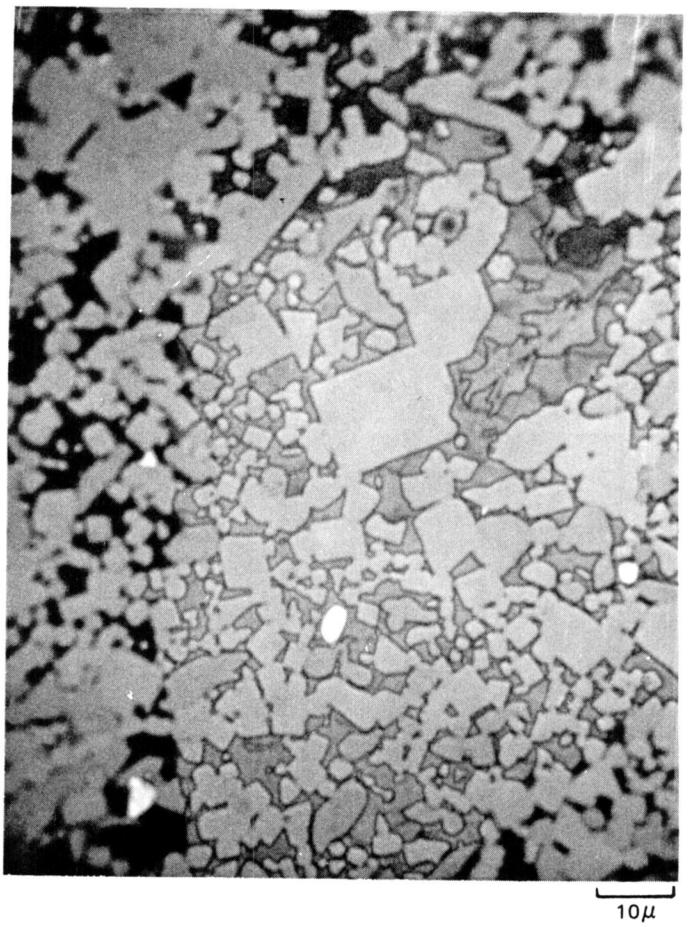

Figure E8 Etched Section of Sample 1078 A (75 w/o $Y_2Si_3O_3N_4$ Cooled From 1700°C

77–12–44–16

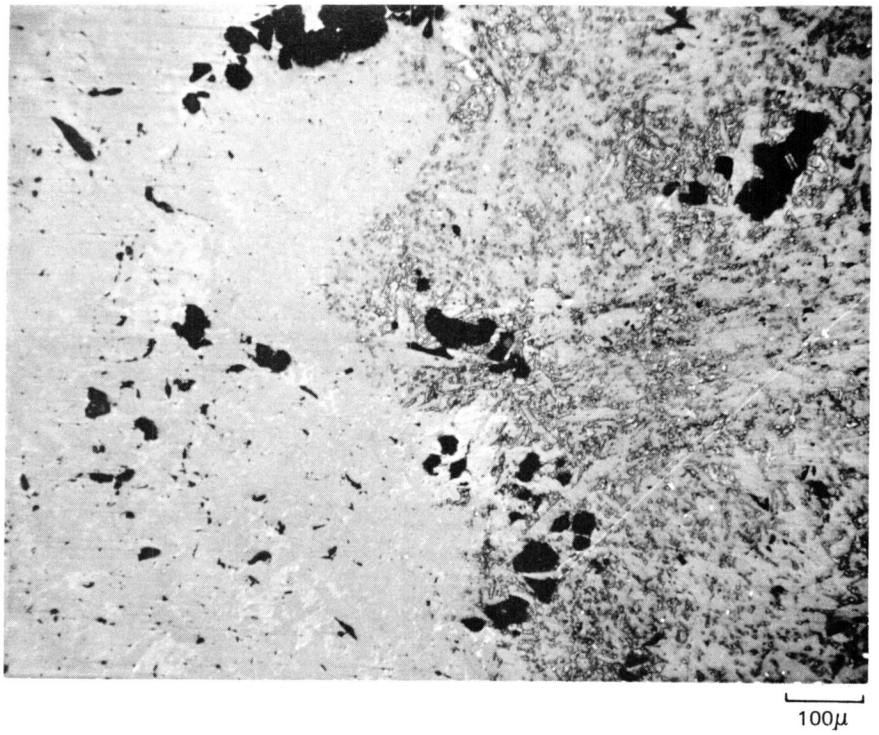

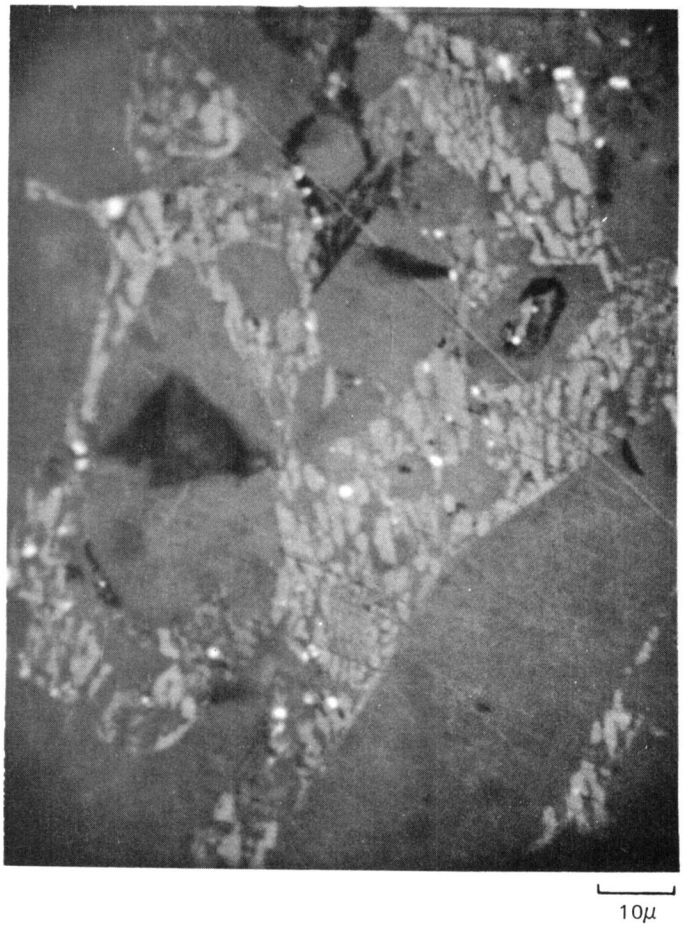

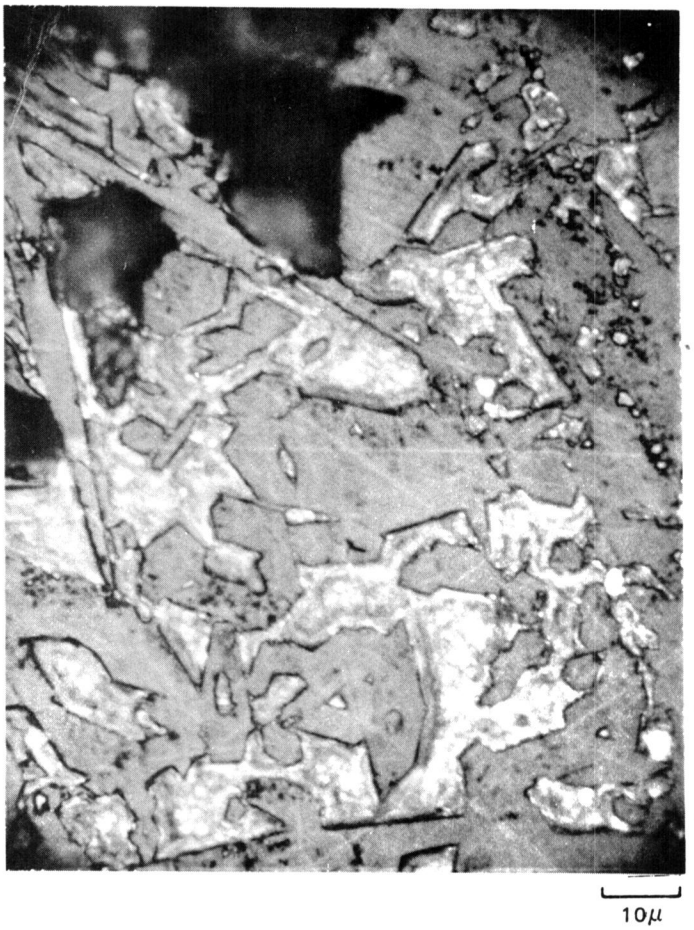

Figure E9 Etched Section of Sample 1068 (20 m/o $Nd_2Si_3O_3N_4$) Cooled From 1750°C

A. 1750°C (SAMPLE 1041)

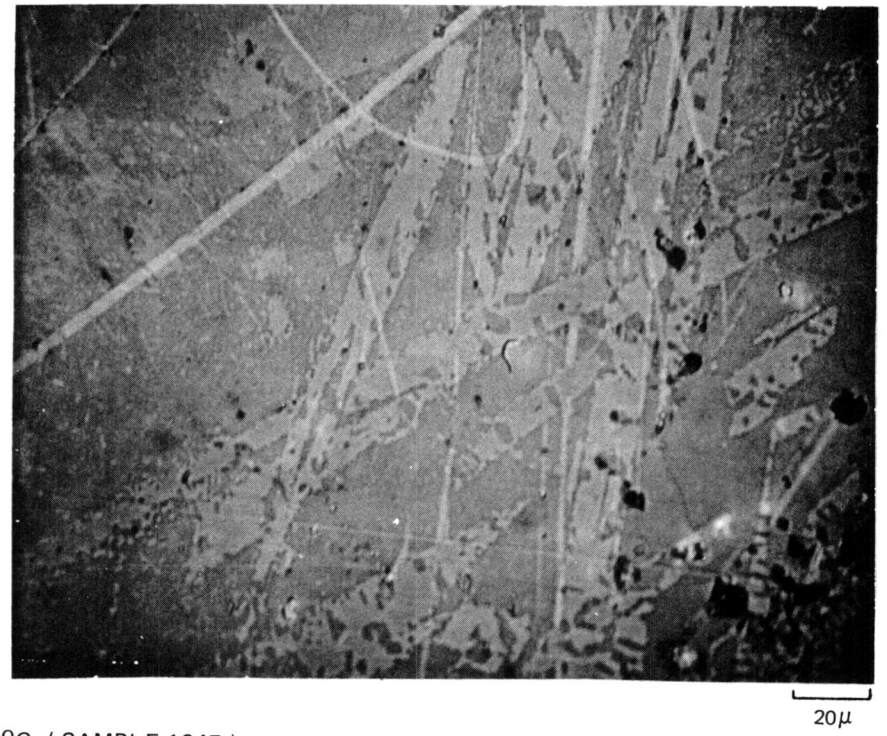

B. 1800°C (SAMPLE 1047)

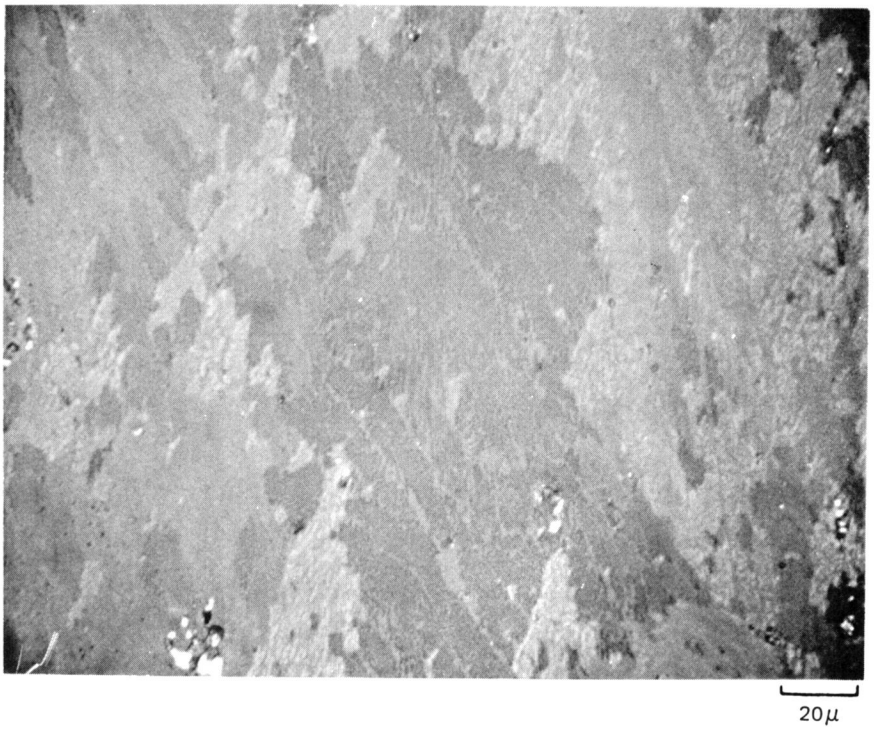

Figure E10 Etched Section of $NdSiO_2N$ Cooled From Different Temperatures

77–12–44–6